2019

Engineering cytocompatible conducting polymers for bio-related energy applications

Changchun Yu
University of Wollongong

UNIVERSITY
OF WOLLONGONG
AUSTRALIA

Australian Research Council Centre of Excellence for Electromaterials Science

Intelligent Polymer Research Institute

Australian Institute for Innovative Materials

Engineering cytocompatible conducting polymers for bio-related energy applications

Changchun Yu

B. Eng., M. Eng.

This thesis is presented as part of the requirements for the

Award of the Degree of Doctor of Philosophy of

The University of Wollongong

February 2019

Certifications

I, Changchun Yu, declare that this thesis, submitted in fulfilment of the requirements for the award of Doctor of Philosophy, at the Australian Institute for Innovative Materials, University of Wollongong, is wholly my own work except where specific references or acknowledgements are made. The thesis has not been submitted for a degree to any other university or institution.

Changchun Yu

March 2019

Publications

1. **Changchun Yu**, Xuanbo Zhu, Caiyun Wang, Yahong Zhou, Xiaoteng Jia, Lei Jiang, Xiao Liu, and Gordon G. Wallace. "A smart cyto-compatible asymmetric polypyrrole membrane for salinity power generation." *Nano Energy* 53 (2018): 475-482.

2. **Changchun Yu**, Caiyun Wang, Xiao Liu, Xiaoteng Jia, Sina Naficy, Kewei Shu, Maria Forsyth, and Gordon G. Wallace. "A cytocompatible robust hybrid conducting polymer hydrogel for use in a magnesium battery." *Advanced Materials* 28, no. 42 (2016): 9349-9355.

3. Kezhong Wang, Christopher L. Frewin, Dorna Esrafilzadeh, **Changchun. Yu**, Caiyun Wang, Joseph J. Pancrazio, Mario Romero-Ortega, Rouhollah Jalili, Gordon G. Wallace, "High performance graphene-fiber-based neural recording ricroelectrodes." *Advanced Materials* 2019, 1805867.

4. Xiaoteng Jia, Caiyun Wang, Vijayaraghavan Ranganathan, Bradley Napier, **Changchun Yu**, Yunfeng Chao, Maria Forsyth, Fiorenzo G. Omenetto, Douglas R. MacFarlane, and Gordon G. Wallace. "A biodegradable thin-film magnesium primary battery using silk fibroin–ionic liquid polymer electrolyte." *ACS Energy Letters* 2, no. 4 (2017): 831-836.

5. Yunfeng Chao, Yu Ge, Yong Zhao, Jicheng Jiang, Caiyun Wang, Chunyan Qin, Amruthalakshmi Vijayakumar, **Changchun Yu**, and Gordon G. Wallace. "Tuning the structure of three dimensional nanostructured molybdenum disulfide/nitrogen-doped carbon composite for high lithium storage." *Electrochimica Acta* 291 (2018): 197-205.

Acknowledgements

I would like to express my gratitude to my supervisors, Professor Gordon G. Wallace, Dr. Caiyun Wang and Dr. Xiao Liu for the opportunity to carry out my doctoral research at IPRI, and for their tremendous mentoring during the research of this interdisciplinary project. Caiyun, Gordon and Xiao, thank you for your contributions of time and ideas to make my Ph.D. experience productive and stimulating. Your guidance and feedback are crucial and invaluable for me to carry out impactful research. I am very grateful for your support and the trust in me to move this challenging project forward. Thank you very much.

I would like to acknowledge my honorary collaborators, Prof. Lei Jiang, Dr. Yahong Zhou and Mr Xuanbo Zhu at the Chinese Academy of Sciences, Dr. Sina Naficy at IPRI and Prof. Maria Forsyth at Deakin University for their contributions to experiments or writings. This research project also benefited tremendously from the input and expertise of many staff members in AIIM. Thanks to Dr. Kerry Gilmore, Dr. Sanjeev Gambhir, Dr. Patricia Hayes, Dr. Tony Romeo and Dr. Sapidar Sayyar for their technical support. I would also like to thank my teammates, Dr. Chen Zhao, Dr. Kewei Shu, Dr. Xiaoteng Jia, Dr. Yu Ge, Mr. Yunfeng Chao, Ms. Amuruthalakshimi Vijayakumar, Mr. Yong Zhao, A/Prof. Liang Shao, Dr. Yan Han, Dr. Zan Lu, and Mr. Kezhong Wang, with whom I have had gainful and pleasant working experience in Lab 209. Also, I would like to express my sincere gratitude to Assoc. Prof. Chee O. Too for his critical proof-reading of my publications.

I gratefully acknowledge the funding sources China Scholarship Council and University of Wollongong that made my Ph.D. work possible.

Finally, I sincerely owe my achievements to my harmonious family for their love and support. And most of all for my husband Mr. Wenke Fan whose faithful accompany during the whole periods of this Ph.D. is greatly appreciated. Thanks for their endless love.

Changchun Yu

University of Wollongong

March 2019

Abstract

Portable, wearable and implantable medical devices (IMDs) can be used to solve various clinical problems such as monitoring of chronic diseases or artificial organ transplantation. Current available IMDs are generally powered by an energy source with a strong case for absolute encapsulation. It would be ideal to minimise the size and volume of the power source for users' comfort by removing the strong case if the employed materials and by-products are safe for the body. In this thesis, two types of cytocompatible conducting polymers have been fabricated via facial chemical synthesis methods for use in bio-related energy sources that are capable of providing energy with the use of simulated body fluids. They are polypyrrole/poly(3,4-ethylenedioxythiophene) polystyrene sulfonate (PPy/PEDOT) hydrogel and asymmetric polypyrrole (PPy) membrane. The demonstrated bio-related energy systems include a bioelectric battery and an energy harvesting system.

First, a robust hybrid PPy/PEDOT conducting polymer hydrogel is fabricated through a two-step ionic crosslinking process combined with a subsequent electropolymerization process. This hydrogel demonstrates suitable mechanical property for electrode-cellular application and good catalytic ability to oxygen reduction for the Mg-air battery. The assembled Magnesium-air biocompatible battery can provide a stable voltage， which may deliver sufficient capacity for some implantable medical devices. This hydrogel has also been demonstrated to be a good substrate for Adipose-derived stem cell adhesion, and cell differentiation via electrical stimulation. The combination of excellent electrochemical properties, appropriate mechanical properties and cytocompatibility make it a promising candidate for bionic applications.

Then, the application of PPy/PEDOT hydrogel in an iron-air battery has been investigated. Iron stent is considered to be an interesting candidate for biodegradable implant material. Degradation of the iron anode in the simulated body fluid electrolyte is improved when it is subjected to a discharge process in this battery system, as evidenced by higher amount of iron produced as detected by atomic absorption spectrophotometer analysis. This battery provides a stable potential and energy as well. Electrochemical results also prove the improved corrosion rate of the iron anode; including decreased corrosion impedance, increased anodic slope and positively shifted corrosion potential. Combined with its cytocompatibility and energy providing capability, this Fe-air battery may provide a dynamic technique to increase the degradation rate of iron stent and provide energy for biological activities, potentially for vascular intervention and osteosynthesis.

Finally, another energy source - a salinity energy harvesting system is developed by using PPy membrane as an ion-exchange membrane and salt solutions with salinity difference. In this system, a single component porous PPy membrane with an asymmetric structure is prepared via a facile self-assembly process. It demonstrates an electronically tuneable conductance, and asymmetric wettability at its two faces. The system composed of this membrane can capture energy arising from a salinity gradient using artificial seawater and river water; providing a stable current when connecting with a resistor. The combination of cytocompatibility and capability of salinity energy conversion makes this membrane a promising material for harvesting energy from the stream of body fluid.

Abbreviations

IMDs	Implantable medical devices
AIMDs	Active implantable medical devices
ORR	Oxygen reduction reaction
CPs	Conducting polymers
PRO	Pressure retarded osmosis
RED	Reverse electrodialysis
IEM	Ion exchange membrane
CEM	Cation exchange membrane
AEM	Anion exchange membrane
HC	High concentration solution
LC	Low concentration solution
PPy	Polypyrrole
PEDOT	Poly(3,4-ethylenedioxythiophene)
PSS	Polystyrene sulfonate
*p*TS	p-toluene sulphonic acid
CPHs	Conducting polymer hydrogels
FBS	Fetal bovine serum
DMEM	Gibco Dulbecco's Modified Eagle'sMedium
βFGF	Basic fibroblast growth factor

ALP	Alkaline phosphatase
PI	Propidium Iodide
ARS	Alizarin Red S
hADSCs	Human adipose-derived stem cells
SEM	Scanning electron microscope
EDX	Energy-dispersive X-ray spectroscopy
XPS	X-ray photoelectron spectroscopy
TGA	Thermal gravimetric analysis
FTIR	Fourier-transform infrared spectroscopy
CV	Cyclic voltammetry
EIS	Electrochemical impedance spectroscopy

Table of content

List of Figures

List of Tables

Chapter 1 Introduction

With increasing ageing population, there emerges an increased demand for portable, wearable and implantable medical devices (IMDs). IMDs are the devices that are either partly or totally introduced into the human body and directly contact with tissues for functioning [1]. IMDs could be classified into two types based on whether their functioning relies on an energy source or the body or gravity: passive implantable medical device and active implantable medical devices (AIMDs) [2]. AIMDs able to perform more complex functions are being widely used for different purposes of monitoring or curing diseases. They can improve healthcare, aid or deliver the functions of certain organs that are being utilized for diagnosis and treatment [3]. Representative AIMDS include stimulators, pacemakers, defibrillators, insulin pumps, cochlea implants and other implantable monitors (Figure 1.1) [4, 5]. For these AIMDs, a power source is an indispensable component for delivering sufficient energy to ensure their proper functionality.

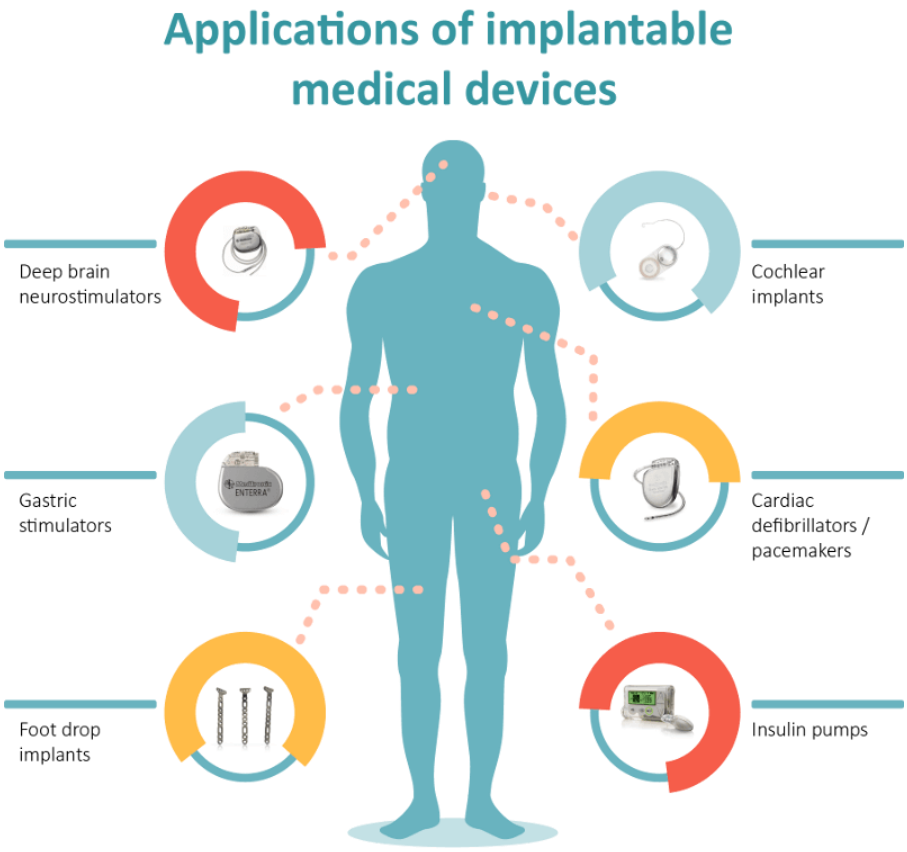

Figure 1.1 Examples of commercial active implantable medical devices [5].

1.1 Implantable power sources for medical devices

Power sources to drive AIMDs should possess properties such as long running life, performance indication, and non-toxicity in the human body [6]. Longevity can reduce the great suffering and financial burdens related to the surgeries for replacing the power source. Biocompatibility is important to minimise the effect on the surrounding tissues caused by the implants. Different types of power sources have been researched, including energy storage devices (batteries, supercapacitors), bio-fuel cells, nuclear cell and energy harvesting system [7]. Currently, electrochemical batteries (most notably lithium batteries) are the predominantly used power source in AIMDs owing

to their high energy density, long term stability, stable and predictable performance [8, 9].

1.1.1 Basics of batteries

A battery is an energy storage device capable of generating electrical energy from chemical redox reactions. Based on the reversibility of those chemical reactions, they can be generally categorized into two types: secondary (re-chargeable) and primary batteries. The former type involves multiple charging/discharging cycles, and primary batteries are designed to be used once.

In the discharging state of a battery, an oxidation reaction occurs at the anode and a reduction reaction at the cathode. Electrons flow from the anode to cathode, while ions move in the reverse direction via an ionic substance (an electrolyte) to close the circuit [10]. In a secondary cell, inputting an opposite direction of the discharged current into the cell can regenerate the chemical reactants to restore its original condition [11]. In contrast, the reaction cannot be completely reversed in a primary battery. The commercially available rechargeable batteries mainly include nickel-cadmium batteries, nickel-metal hydride batteries, lithium ion batteries and lead-acid batteries. Take a Li-ion battery for example, Li^+ ions move between the anode and cathode via the electrolyte during the charging and discharging processes, and electrons move via an external circuit to complete the reaction (Figure 1.2) [12].

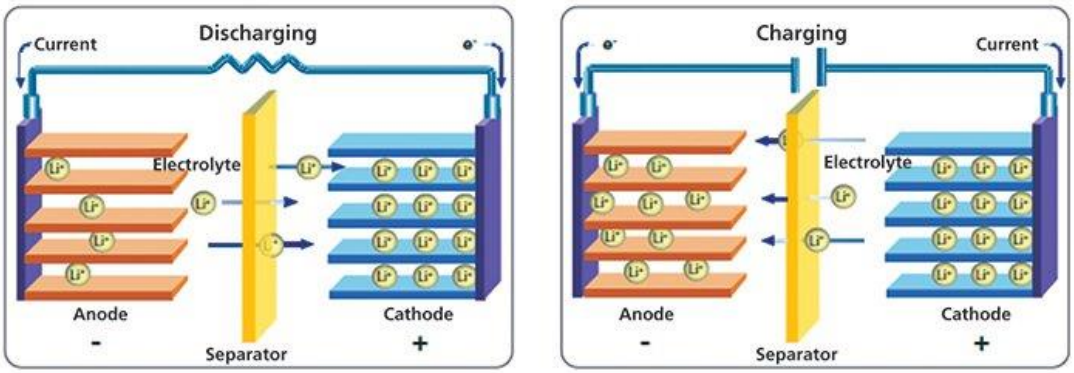

Figure 1.2 Movement of Li^+ ions balances the electrons during the charge and discharge processes of a Li-ion battery [13].

1.1.2 Batteries for Implantable Medical Devices

For AIMDs, the power needs generally fall within the range of μW–mW as listed in Table 1.1. [2].

Table 1.1 Power requirements of different AIMDs.

Implanted device	Typical power requirement
Pacemaker	30-100 μW
Cardiac defibrillator	30-100 μW
Neurological stimulator	30 μW to several mW
Drug pump	100 μW to 2mW
Cochlear implant	10 mW

The earliest practical implantable pacemakers appeared in the late 1950s and were powered by Zn/HgO batteries [14]. It is important for an AIMD battery to be sealed against the human body's moist environment [15]. However, Zn/HgO batteries leak hydrogen and therefore cannot be totally sealed. Nuclear batteries with the unique

characteristics of high energy density and outstanding reliability were an appealing alternative [7], however, toxicity and the necessary tight regulatory controls are two major concerns that limited their application in medical devices [16]. Since the first implantation of lithium/iodine–polyvinylpyridine (PVP) to power a pacemaker in 1972, lithium batteries such as Li/I_2, Li/MnO_2, $Li/Ag_2V_4O_{11}$ batteries and lithium ion batteries have become the dominant power sources in AIMDs [8, 17]. However, these batteries contain toxic substances that possess poison or do damage to the surrounding body tissues [7]. The safety concerns associated with the used toxic materials and/or the products produced during the electrochemical processes needs a strong housing and sturdy encapsulation as a barrier between the human body and hazardous batteries [18]. As a result, the size of an AIMD is commonly determined by the battery component because it occupies the largest volume and weight of the device. Providing desirable energy to miniature medical devices becomes challenging due to the limited available space or inaccessible location. Hence, there is a call for the development of a biocompatible energy source that may be directly implanted into the human body or can be generated inside the human body in combination with the use of biocompatible materials.

Body fluids are rich in oxygen and ions that are suitable for use as an electrolyte in metal air batteries. Using the inexhaustible body fluid as an electrolyte also eases the worries of electrolyte degradation which is related with the chemical reactions of the battery. Various body fluids such as gastric acid, blood, saliva and urine have demonstrated their use in bioelectric batteries [19]. These types of batteries can be easily miniaturized without the use of a case if the electrodes materials and their by-products are all safe enough for body implantation [20]. It would be a bonus if the employed electrode materials and the by-products are useful or even essential for the

body, such as the inorganic substances Mg, Fe and Ca that are contained in our dietary requirements.

1.2 Bioelectric battery

A bioelectric battery is basically a metal/air cell which relies on the oxidative corrosion of metals at the anode and reduction of oxygen at the cathode with the use of body fluid as electrolyte [21, 22]. It was first reported in the 1960s [23] where the device consisted of a silver-silver chloride or carbon cathode, a sacrificial zinc anode and body fluid electrolyte. It had been tested in clinical experiments *in vivo* [23, 24].

A metal-air battery system has the highest energy density among all aqueous batteries [11], which results from the cell design that the cathode material oxygen is available from the surroundings rather than being contained inside [25]. Oxygen from the surroundings diffuses to the cathode surface and is reduced to hydroxyl ions. It is a very attractive energy system for biocompatible power sources as the reactant oxygen can come from the body fluid. Take the magnesium (Mg)-air battery as an example, the generated hydroxyl ions migrate to the magnesium anode to complete the reactions as shown in Figure 1.3. The Overall reaction is: $2\ Mg + O_2 + 2H_2O = 2\ Mg(OH)_2$.

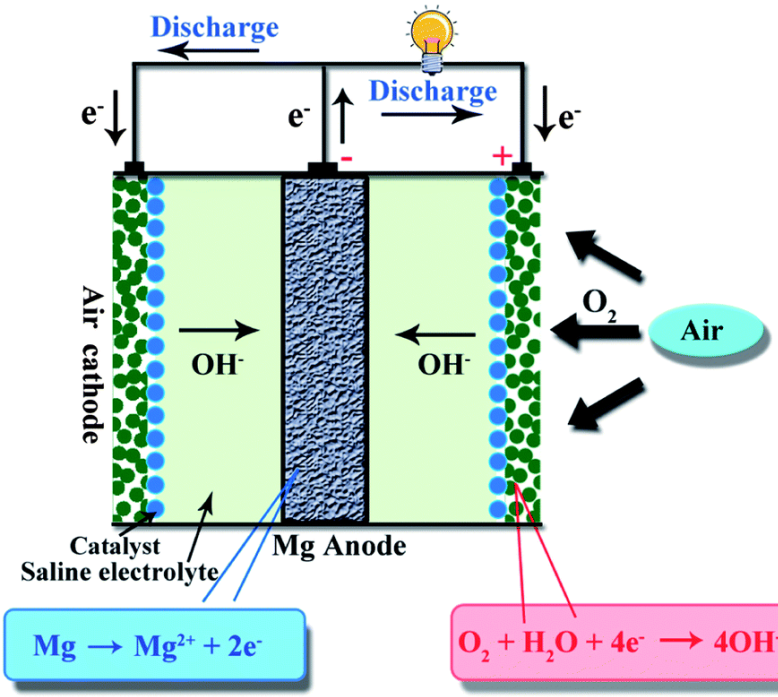

Figure 1.3 Working principle and electrode reactions of a Mg-air battery [26].

1.2.1 Configuration of a bioelectric battery

1.2.1.1 Anode materials

As discussed above, the anode of a bioelectric battery is a sacrificial electrode where oxidation reaction (loss of electrons) takes place. Different anodic materials have been used; such as Mg, aluminium (Al), iron (Fe), manganese (Mn) and zinc (Zn) [27]. Moreover, Mg has attracted attention as biodegradable implants to support tissue regeneration and healing due to the features of it being immunologically inert, with matchable physical properties to the commonly used 316L stainless steel [28, 29]. The product, Mg^{2+} ions, from the Mg anode in this battery are the essential element that accounts for the fourth most abundant cation in the human body [26, 30, 31]. Apart from the Mg^{2+}, normal human males also possess 3-5 g of Fe in their bodies, and most of them are in circulating red cells as haemoglobin [32]. For an Fe-air battery, its

discharge reaction is $Fe + 2OH^- = Fe(OH)_2 + 2e$. The theoretical energy density of an Fe/air couple is around 485 Wh/kg with an open-circuit potential of 1.2 V [33].

Compared with an Fe-air battery, a Mg-air battery can afford higher electrochemical performance: A high power density (6.8 kW h kg^{-1}) can be driven due to the high theoretical capacity (2.2 Ah g^{-1}) and low negative standard potential (-2.37 V vs standard hydrogen electrode) of Mg. Alloying Mg with other metals such as Al, Mn, or Zn [34, 35] also has been extensively investigated to improve the battery performance; as Mg alloy suppresses the HER and reduces the self-corrosion of Mg.

1.2.1.2 Cathode materials

The cathode material in a bioelectric battery is non-consumable and serves as a catalyst for the oxygen reduction reaction (ORR). A high performance metal-air battery requires an efficient “air breathing” cathode to facilitate ORR within a highly porous structure [36], since the transport or diffusion of oxygen to active sites plays a key role in determining the battery performance [37]. Biocompatibility is another important desirable property for the cathode materials working in a human body. Noble metals such as the Platinum (Pt) -group metals, in particular Pt itself, have been intensively studied as cathodes for bioelectric battery because of their known high stability, biocompatibility and superior electrocatalytic activity [38, 39]. For example, G. Fontenier et al. proposed a platinum-magnesium bioelectric battery, showing good organism tolerance and capable of supplying power to a pacemaker [38, 40]. Pt alloys (i.e., Pt-Au, Pt-Co, Pt-Ni) and Pt nanoparticles have also been used for ORR with a much improved reaction activity and battery performance [41, 42]. Nevertheless, developing high performance low cost metal-free organic matter catalysts is the

ultimate solution to overcome the obstacles of high cost, scarcity and sustainability of noble metals [43].

Carbon-based materials are considered as one of the most promising ORR catalysts with high activity and stability. They possess a relatively wide potential window for stable catalysis and good conductivity for electron transfer. As a unique material family that is composed of repeat units of carbon containing heteroatoms, conducting polymers (CPs) have widely been explored as promising inherent electrocatalysts for ORR due to their unique delocalized conjugated structures, excellent electrical and electrochemical properties [44, 45]. Their properties and applications as electrocatalysts in ORR will be discussed in section 1.4.

1.2.2 Research Progress on Bioelectric battery

Developing batteries with durable, biocompatible and reliable features will be continuously progressing to meet the requirements of new generation of IMDs with new functionalities. The bioelectric battery is expected to support the electronics with multifunctionality over the long term. Many impressive examples that use a bioelectric battery to power the IMDs have appeared in the laboratory or even in clinical studies recently.

A Zn/Cu galvanic cell with gastric or intestinal fluids as electrolyte and tissues as the salt bridge has been demonstrated. The involved reactions were oxidation of Zn electrode ($Zn \rightarrow Zn^{2+} + 2e$), hydrogen gas evolution ($2H^+ + 2e^- \rightarrow H_2$) and/or oxygen reduction ($O_2 + 2H_2O + 4e^- \rightarrow 4OH^-$) at the Cu electrode. It generated an open circuit potential of 0.76 V with a galvanic apparent internal resistance of various tissues (heart, lung, liver) [46]. This kind of Zn-Cu battery enclosed in a capsule had demonstrated effective functioning in a porcine stomach *in vivo* (Figure 1.4) [47]. It was

accompanied with semiconductor parts; including a potentiometer and digital converter. This device delivered an average power of 0.23 mW/mm^2 for 6.1 days to power the temperature measurement in the gastrointestinal tract of pigs. It could also continuously power wireless transmission, and drug delivery *in vivo*.

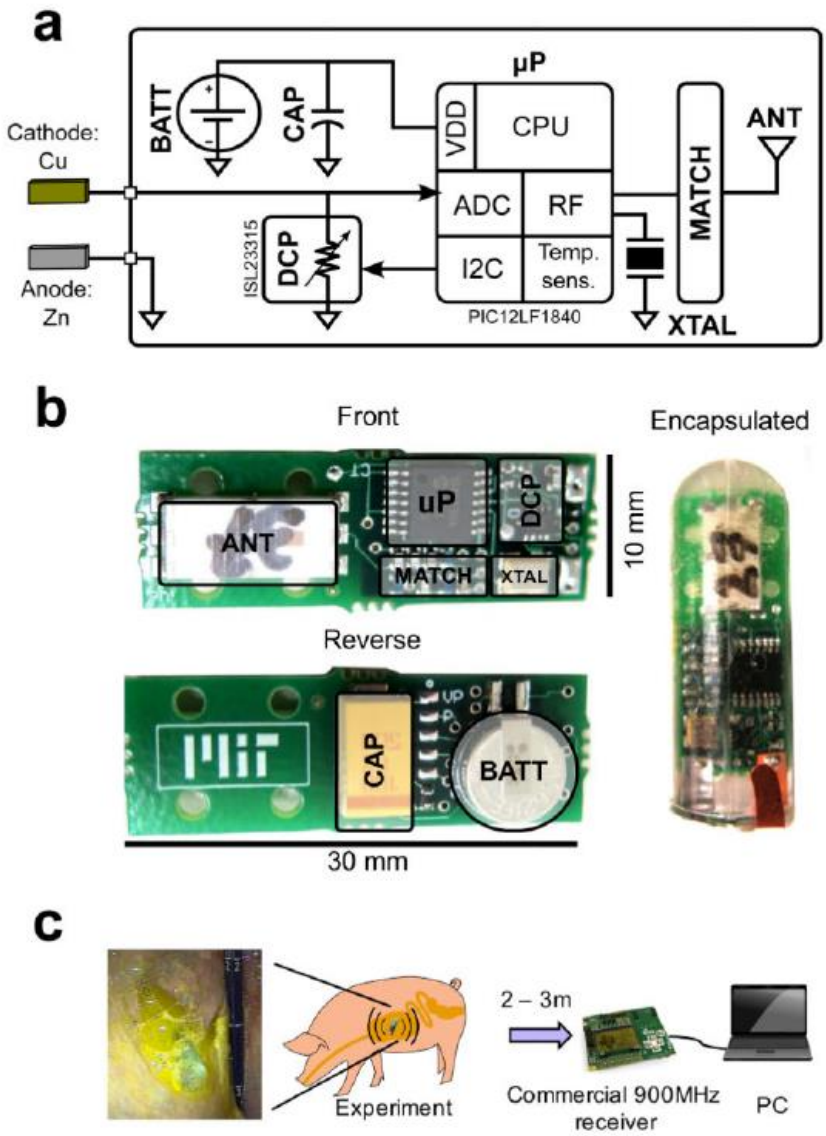

Figure 1.4 A gastric battery in a porcine model: a) Simplified architecture of the measurement system; b) Photograph of the front and reverse sides of the system along with encapsulation. The PCB includes a programmable load resistor (DCP), crystal

(XTAL), microcontroller (μP), RF matching network (MATCH), and antenna (ANT) on the front side, and the battery (BATT) and decoupling capacitor (CAP) on the back side. c) Photograph of the encapsulated pill in contact with gastric fluid inside the porcine stomach [47].

A similar Mg/CuCl bioelectric battery was developed as a power source to drive an ingestible sensor with demonstrated safety for clinical use (Figure 1.5) [48]. It composed of a Mg anode, a CuCl cathode with gastric fluid electrolyte that could generate an open circuit potential of 1.85 V ($Mg + 2CuCl \rightarrow 2Cu + 2Cl^{-} + Mg^{2+}$). This battery had also demonstrated chemical, toxicological, mechanical, and electrical safety for in vivo clinical application.

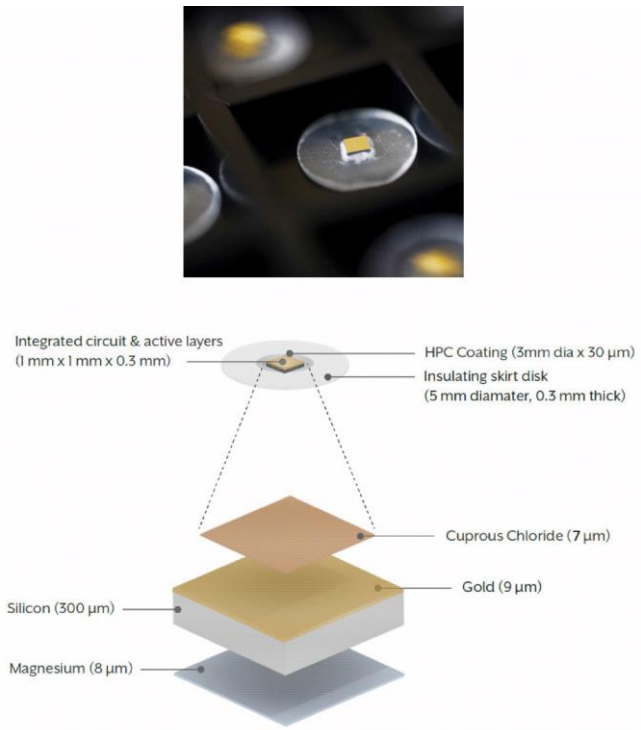

Figure 1.5 Photograph and schematic of an ingestible sensor [48].

To power a temporary medical device, a bioelectric battery of magnesium–molybdenum trioxide (Mg–MoO_3) battery system was developed. It could separately drive a LED, a calculator, and the amplifier of an electrocardiography signal detector (Figure 1.6) [49]. By introducing alginate hydrogel electrolyte and polyanhydride/poly(lactide-co-glycolide) (PLGA) coating on MoO_3 cathode, the battery was capable of providing a high stable output voltage of up to 1.6 V and a capacity of 6.5 mAh/cm^2 with a prolonged lifetime of up to 13d in humid air at room temperature. A microfabricated Mg/Fe biodegradable battery featuring a total cell volume of less than 0.02 cm^3 delivered a capacity and power of 0.7 mAh and 26 μW. Its operation in various physiological electrolyte solutions has been demonstrated and its performance is listed in the Table 1.2 [50].

Table 1.2 Discharge performance of Mg/Fe batteries in different electrolyte solutions [50].

	0.1 M $MgCl_2$	0.9 wt.% NaCl	Phosphate buffered saline
Discharge time (h)	49	90	99
Average discharge potential (V)	0.5	0.4	0.7
Specific capacity (mAh g^{-1})	509	1100	1060
Energy (J)	3.7	6.2	11
Power (μW)	21	19	29
Coulombic efficiency (%)	23	50	48
Change in electrolyte pH	2.11	3.05	0.41

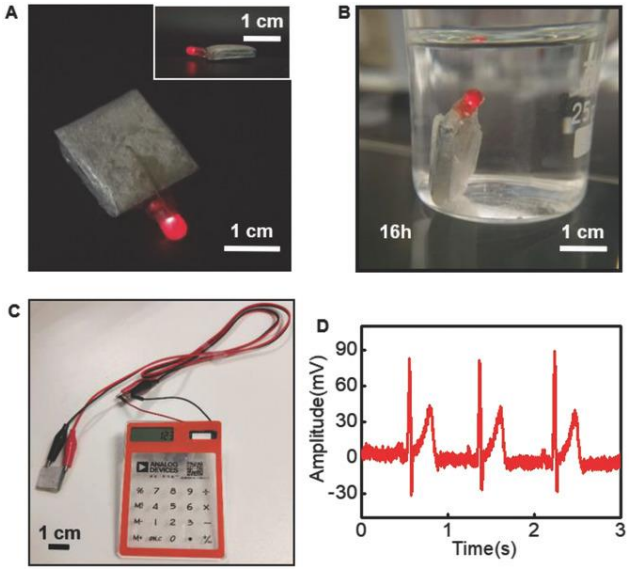

Figure 1.6 A LED light was powered by a magnesium–molybdenum trioxide (Mg–MoO_3) battery in air (A) and in phosphate buffered saline (B). (C) A calculator powered by a Mg–MoO_3 battery. (D) Measured ECG signal with the amplifier of a detector powered by a biodegradable Mg–MoO_3 battery [49].

As another important member of energy storage devices, protein-based supercapacitors that use human body fluids (serum/urine) as electrolytes were also developed and showed no adverse effects on cells after 4 d(days) continuous charge/discharge cycles (Figure 1.7). The electrode was formed by anchoring cation-derivatized (cationized) bovine serum albumin (cBSA) on graphene oxide sheets and further modified with heme protein myoglobin in a layer-by-layer (LbL) manner [51]. These electrodes are very thin (1.14 μm), even thinner than a human hair, yet capable of providing a high power density of 116 W/kg.

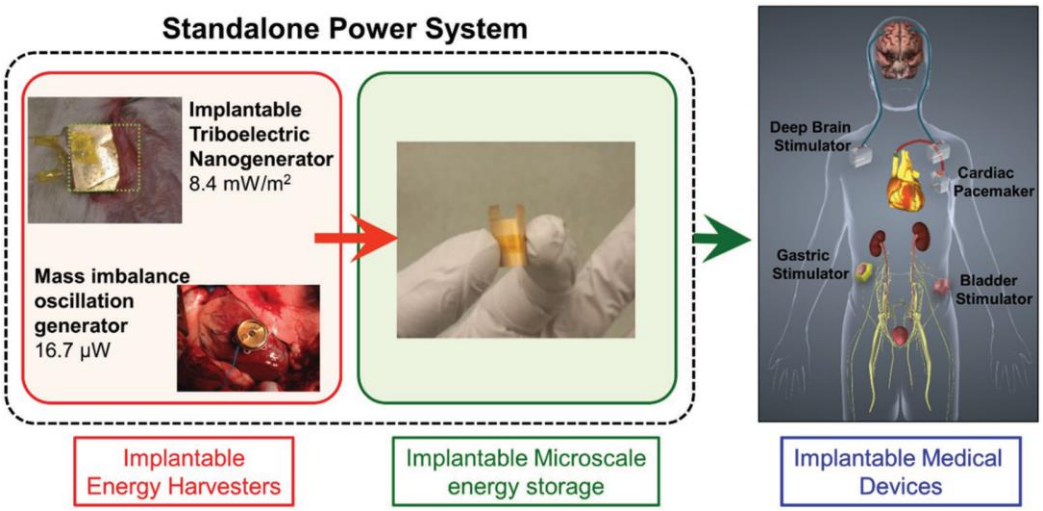

Figure 1.7 Scheme illustrating a graphene oxide/ myoglobin bioelectrochemical supercapacitor (centre panel) as a micropower source for biomedical implants [51].

1.3 Energy harvesting system

Different from the bioelectric battery that converts the stored chemical energy into electricity, an energy harvesting system is a renewable energy source that can capture, harvest or scavenge an ambient energy and convert it into electrical energy [52]. The human body provides numerous potential energy sources including mechanical energy, vibrational energy, chemical energy, and salinity gradient energy. The demonstrated power systems derived from the human body mainly include glucose oxidation [53], kinetic energy from limbs [54], natural vibrations of internal organs [55-58]. A small power can also be derived from the temperature differences of the body and dissipation heat by using a thermo-electric harvester [59]. The energy harvesting technology offers two significant merits: virtually inexhaustible energy sources and little or no adverse environmental effect [60]. For example, Tang et al. developed a self-powered low-level laser Cure System driven by a triboelectric nanogenerator (TENG) (Figure 1.8) for clinical therapy of bone remodelling and orthodontic treatment [61]. However,

it has limited biological applications because of insufficient biocompatibility and stability [62].

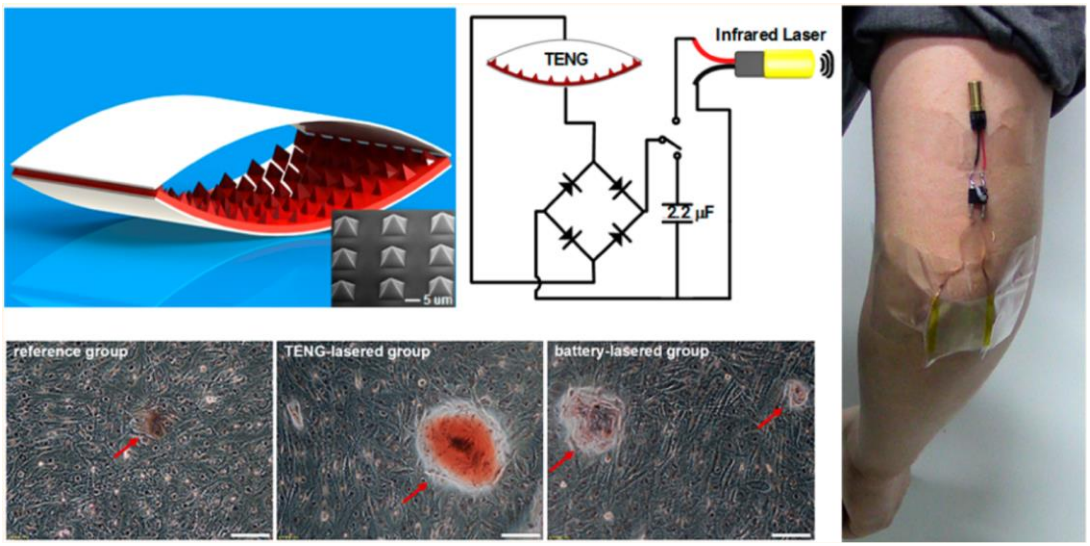

Figure 1.8 A self-powered low-level laser cure (SPLC) system powered by a triboelectric nanogenerator (TENG) that accelerated the mouse embryonic osteoblasts' proliferation and differentiation [61].

Salinity gradient is an important power source in the biological system and involves biological functions such as: adenosine triphosphates (ATPs) being synthesised by proton gradients; nerve pulse being conducted through the change of sodium-potassium gradients; and salinity variation has an effect on the activity of antioxidant enzymes [63, 64]. Ion channels and ion pumps on the cell membranes work together to form the ion concentration gradients and trigger the release of an action potential [65, 66]. Take the electric eel as an example, their electrogenic cells (electrocytes) can generate a potential of ~600 V for predatory purposes and defence [67]. Electrocytes generate electrical discharges using ion channels and receptors, which are polarized at the two sides of cell membranes [67, 68]. The salinity gradient between the

intracellular and extracellular fluid in human body is in the range of 2-30, and in principle it can be used as an energy source for generating a salinity gradient power.

1.3.1 Salinity power generation

Salinity gradient power is captured from water via partitioning two aqueous solutions of different salinities across a membrane [69]. When two aqueous solutions of different salinity are brought in contact, they will spontaneously mix [70]. The induced Gibbs free energy will be converted into electricity (Figure 1.9) [71, 72]. Theoretically, about 2 terawatts can be generated where the rivers flow into the sea on a global scale, and it almost equals the world's electricity consumption in 2015 [73]. Technologies to harvest this clean and sustainable energy source mainly include pressure retarded osmosis (PRO), mixing entropy batteries, and reverse electrodialysis.

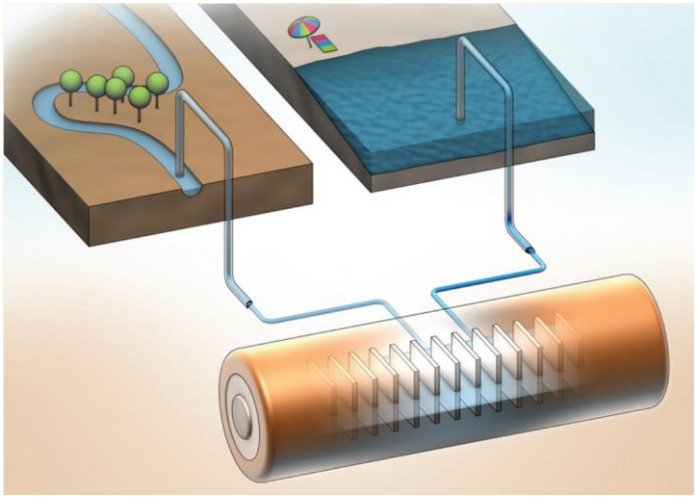

Figure 1.9 Salinity difference between salt water and fresh water can be used to generate renewable energy [72].

1.3.1.1 Pressure retarded osmosis

Pressure retarded osmosis (PRO) is a technique that uses a semipermeable membrane to separate a solution with low concentration (e.g., river water) from a solution that

is more concentrated (e.g., sea water) [74]. The semipermeable membrane allows the solvent (water) to permeate and retains the solute (dissolved salts). The osmotic pressure between these two solutions drives water molecules to transfer through the membrane from the diluted salt solution to the more concentrated one [75].

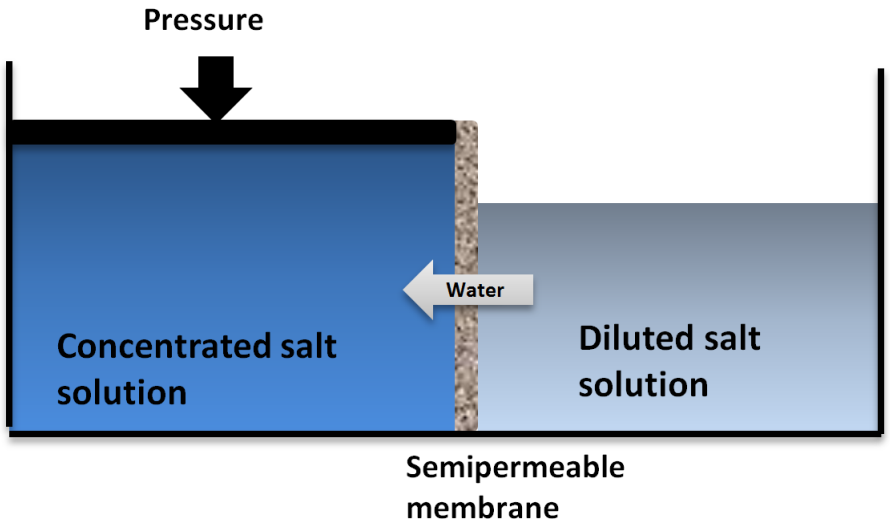

Figure 1.10 Conceptual representation of pressure-retarded osmosis [76].

The currently available PRO application for seawater and fresh water with an osmotic pressure difference of $\Delta\pi$ = 20–25 bar can yield a power density between 0.11 and 1.22 W/m^2 [76]. From more concentrated brines and fresh water ($\Delta\pi$ > 75 bar), the power density could reach 2-5 W/m^2 when using the membranes with high permeability, high salt rejection and low transport resistance [77].

1.3.1.2 Capacitive mixing batteries

The entropy increase from mixing two solutions of different salt concentrations can be harnessed to generate electrical energy [78]. Capacitive mixing batteries are based on an electrochemical cell with two electrodes dipping in the solutions with salinities difference. This method has its roots in the ability to store a very large amount of electric charge inside the supercapacitor or battery electrodes [79]. These electrodes

could accumulate electrical charge that they are charged in one solution and discharged in another. The potential can be generated due to the electrode potentials difference induced by the salinity change (Figure 1.11) [80].

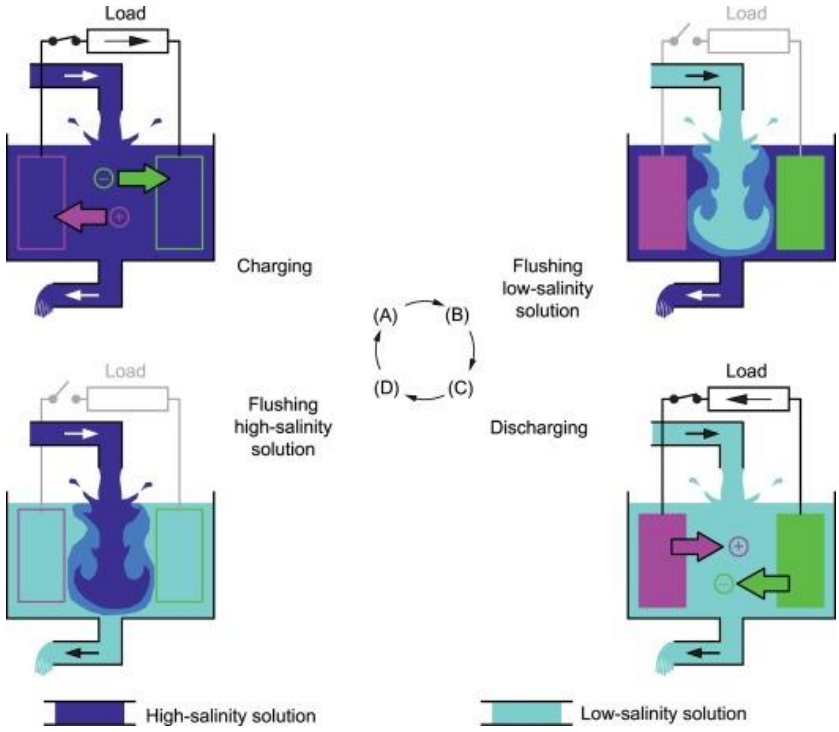

Figure 1.11 Schematic representation of the four steps of a capacitive mixing cycle. The cycle begins with the cell filled with high-salinity solution. Step A: A current flows in one direction. Step B: The circuit is opened, and solution in the cell is substituted with a low-salinity feed solution. Step C: A current flows in the opposite direction with respect to Step A. Step D: The circuit is opened, and the liquid in the cell is substituted with a high-salinity feed solution [80].

The produced voltage of the capacitive mixing batteries depends on the adsorption of charged molecules on the electrodes [81]. Activated carbon is the widely used material in capacitive mixing batteries because of its huge surface area per gravimetric unit for high specific capacitance; and its behaviour is close to that of an ideally polarizable

material [82]. However, the peak power density obtained is only around 200 mW/m^2, which is far below those reported for PRO (1–10 W/m^2) [83].

1.3.1.3 Reverse electrodialysis

Reverse electrodialysis (RED) is a reverse desalinization process that uses an ion exchange membrane (IEM) to derive energy from the electrochemical potential difference from the concentrated and dilute salt solutions [84]. When two solutions are fed separately on either side of an IEM, ions will preferentially diffuse from high concentration solution (HC) to low concentration solution (LC).

1.3.1.3.1 Basics of reverse electrodialysis

Membranes with specific charges can be used to capture the energy from a salinity gradient by screening the passing ions, resulting in a net electrical current. Specifically, anion exchange membranes that are characterized with fixed positive surface charges allow anions to pass through, while cation exchange membranes with negative charges allow cations to permeate through. In a reverse electrodialysis system with stacks of ion exchange membranes, cation and anion exchange membranes are arranged in an alternating pattern between a cathode and an anode (Figure 1.12) [76]. Take a sodium chloride solution as an example, Na^+ permeates through a cation exchange membrane towards the cathode, while Cl^- permeates through an anion exchange membrane towards the anode. At the electrodes, the ionic current is converted into the electronic current via a redox reaction. Electro-neutrality of the solution is maintained via an oxidation reaction at the anode surface and a reduction reaction at the cathode surface. As a result, electrons move from the anode to the cathode via an external electric circuit.

It has been shown that, in the case of river water with seawater (salinity ratio 0.05M/0.1M), the RED is a promising technique when compared with PRO, as the PRO process requires extremely low concentration of the diluted solutions [76].

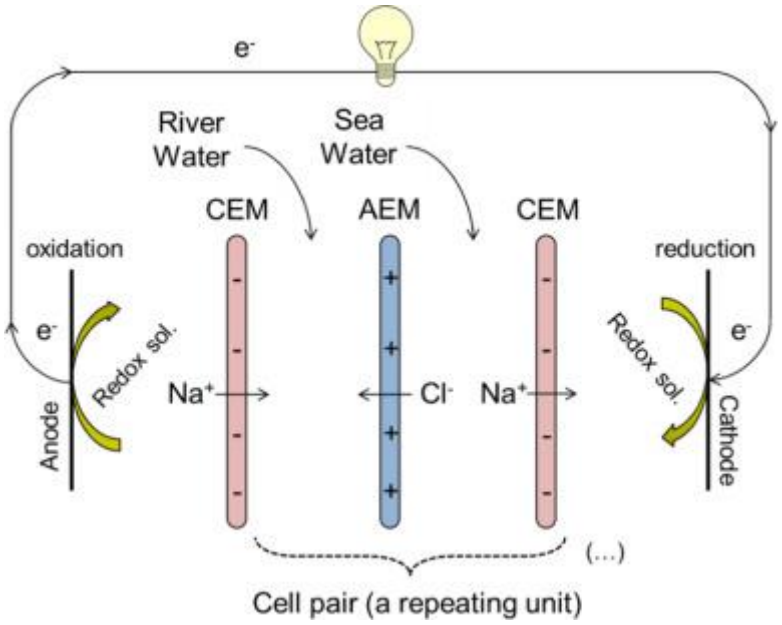

Figure 1.12 Conceptual representation of an energy conversion scheme using reverse electrodialysis, “CEM” and “AEM” mean cation exchange membrane and anion exchange membrane, respectively [85].

1.3.1.3.2 Ion-exchange membrane

In a RED process, the ion exchange membrane is the core component determining the power conversion performance [86]. The predominant properties required for an efficient RED membrane mainly include low electrical resistance, high transport number, and high permselectivity [86-89]. In the charged nanochannels within ion-exchange membranes, counter-ions are preferentially transported, that is, ion-selectivity occurs[90]. Permselectivity indicates the ability of IEMs to selectively transport counter-ions (e.g., cations in the case of a CEM) and exclude co-ions [91].

Permselectivity of an IEM is highly related to the surface charge properties that are determined by the density, type and distribution of surface charge groups [88].

Guo *et al.* developed a reverse electrodialysis system for efficient osmotic energy conversion that was composed of negatively or positively charged lamellar nanochannels cascaded in graphene oxide membranes (GOM) (Figure 1.13) [92]. Through the preassembly modification, the surface charge polarity of GO nanochannels can be tuned from negative (-123 mC m^{-2}) to positive ($+147$ mC m^{-2}). An output power density of 0.77 W m^{-2} was achieved by mixing artificial seawater and river water.

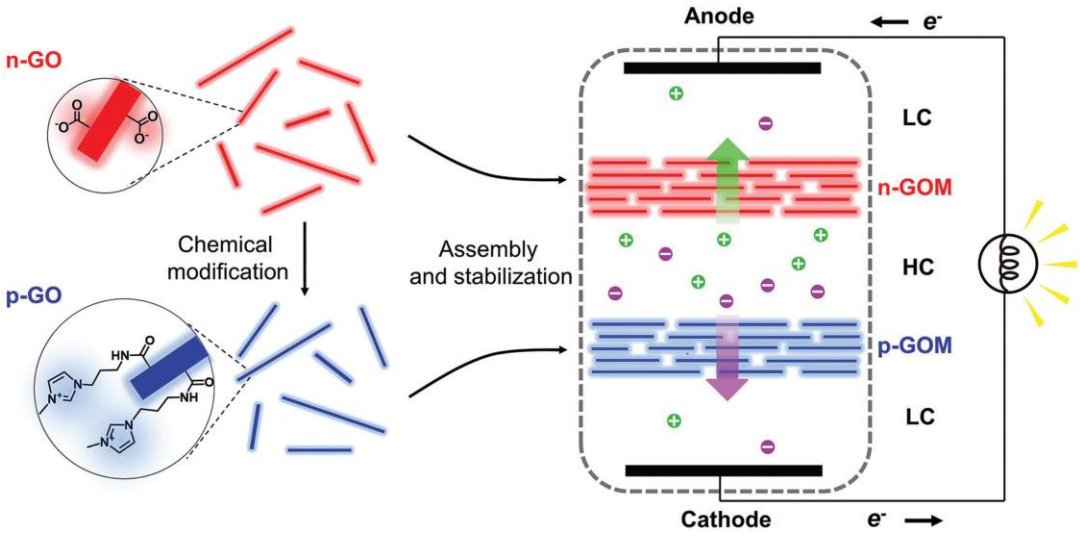

Figure 1.13 Assembly and preassembly modification of the graphene oxide membranes (GOM)-based nanofluidic energy harvesting device. A pair of cation- (n-GOM) and anion-selective GOMs (p-GOM) are used to harvest osmotic energy from concentrated (HC) and diluted (LC) ionic solutions [92].

It has also been documented that asymmetric, conically shaped nanopores with permanent surface charge shows a preferential direction for ion flow, thus promoting the energy conversion efficiency [93]. The schematic diagram is shown in Figure 1.14.

The small opening pore is called tip and the larger end is the base. The positively charged tip attracts counterions due to the requirement of electroneutrality, causing a higher cation concentration than anions. The salinity gradient facilitates the ion transport between the tip and base to generate power. With an inner driving force arising from their asymmetric configuration, this kind of membrane could enhance energy efficiency by decreasing the ionic transport resistance [94].

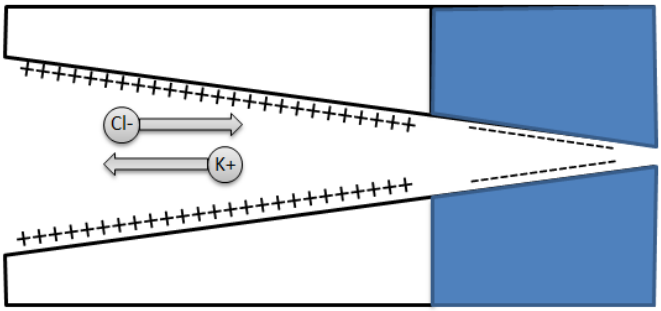

Figure 1.14 Schematic of a conical pore with asymmetric structure.

These ion-channel-mimetic nanofluidic systems can function as single electrogenic cells and built for energy conversion. For example, an ultrathin and ion-selective Janus membrane (Figure 1.15) prepared via a phase separation of two block copolymers enabled an osmotic energy conversion with a power density of approximately 2.04 W m^{-2} by mixing seawater and river water. Due to the asymmetric nanoscale pore size, this membrane facilitated the charge-governed ionic transport in a wide concentration range and exhibited excellent anion selectivity [95].

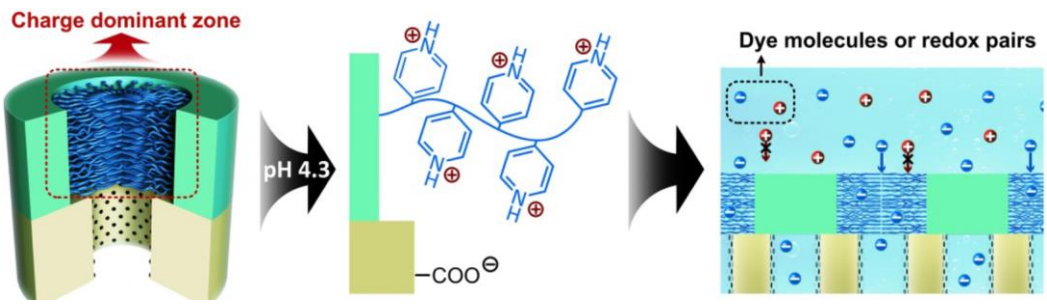

Figure 1.15 The excellent anion selectivity of a Janus membrane (poly(styrenesulfonate) and block polymer) is dominated by the block polymer part, whose nanochannels are filled with polystyrene-b-poly(4-vinylpyridine) chains, showing stronger electrostatic interactions [95].

Inspired from the living systems, the concept of reverse electrodialysis has gained renewed attention in the biological field with advanced IEM fabrication techniques [96]. In a biological system, cell membranes contain numerous nanoscale conductors in the form of ion channels for transporting ions or molecules [68]. The novel ion transport properties of nanochannels in IEMs including excellent selectivity and high throughput may lead to technological breakthroughs in many areas, such as biosensing, separation, energy conversion, and water desalination [95]. Some membranes are smart and can make biomimetic response by responding to environmental stimuli such as pH, temperature, light or electrical potential [97-100]. Those smart membranes with artificial biological ion channels are capable of reproducing the biological energy conversion process based on salinity gradient. Membranes with nanochannels are commonly fabricated by various sophisticated techniques such as self-assembly process, ion track etching, or electrochemical etching (Figure 1.16) [101-103]. The smart nanochannels with heterogeneous structures are generally fabricated either

directly by using functional materials or indirectly by surface modification with functional molecules [104].

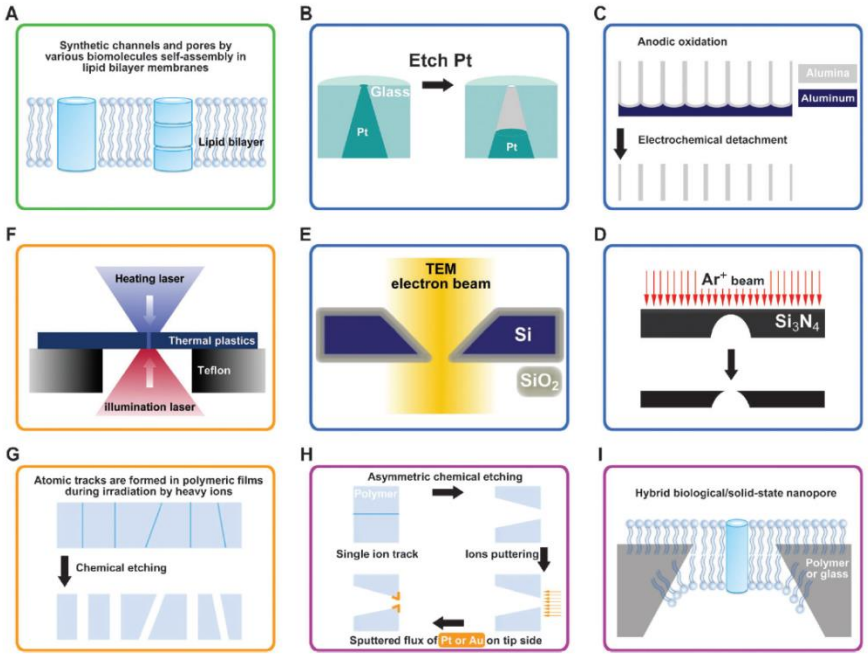

Figure 1.16 Fabrication methods of various shapes and structures of smart membranes: (A) Biomolecules self-assembly; (B) Electrochemical etching; (C) Electrochemical oxidation; (D) Ion beam; (E) Electron beam; (F) Heat process; (G) Chemical etching; (H) Ion-track-etching; (I) Biological pores self-assembly [104].

1.3.2 Bio-application of salinity gradient power

Biological activities of all living entities including humans, animals and plants involve ion transportation. For example, during the signal transmittance along the neurons, Na^+ ions move out of the cell while the K^+ ions diffuse into cells via the cell membrane (Figure 1.17).

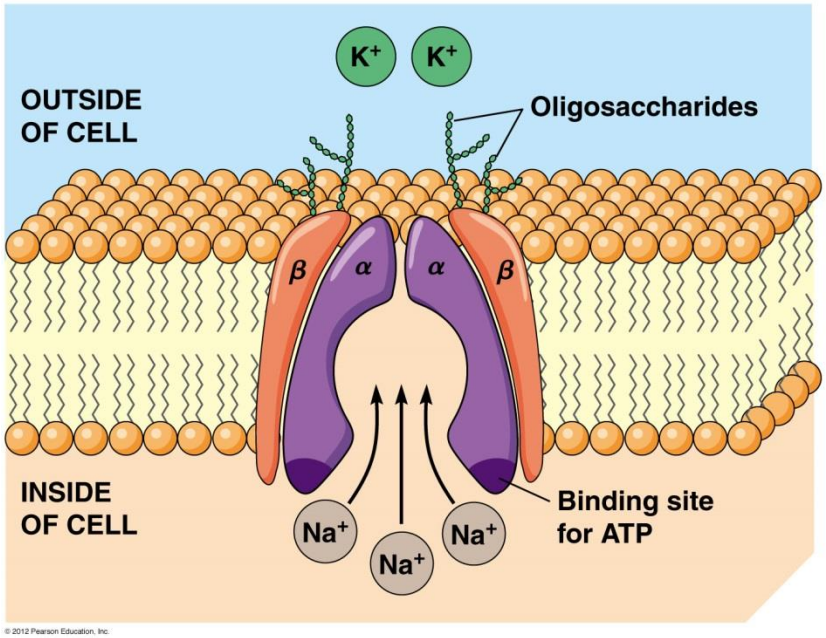

Figure 1.17 Ion transportation through the cell membrane between intracellular and extracellular fluid [105].

Ionic distributions give rise to diffusion potentials, which determine the magnitude and polarity of ionic equilibrium potential [106]. In a biological system, relative permeability of various ions determines the transmembrane potential, which is the voltage arising from the differences in the ions concentrations on opposite sides of a cellular membrane. The concentration of primary ions in the body fluid is listed in Table 1.3.

Table 1.3 Summary of the ion distributions in most types of cells and the equilibrium potentials [106].

Ion	Extracellular Distribution (mM)	Intracellular Distribution (mM)	Equilibrium Potential (mV)
Na^+	145	15	+60
Cl^-	100	5	−80
K^+	4.5	150	−94
Ca^{2+}	1.8	0.0001	+130
H^+	0.0001	0.0002	−18

The existing salinity gradient in the body fluid is a potential source for generating power across an exchange membrane. The electric eel is the best example with a system optimized by natural selection for power generation from ionic gradients. The stacks of electrocytes create electricity by allowing the movement of Na^+ and K^+ (Figure 1.18). Inspired by this, Thomasions et al. developed a similar system by using ions gradients between miniaturised polyacrylamide hydrogel compartments bounded with a repeating sequence of ion exchange membranes [107]. By using thousands of ion gradient units, this system was able to generate an open-circuit potential in excess of 100 V and a power density of 27 mW m^{-2} per tetrameric gel cell.

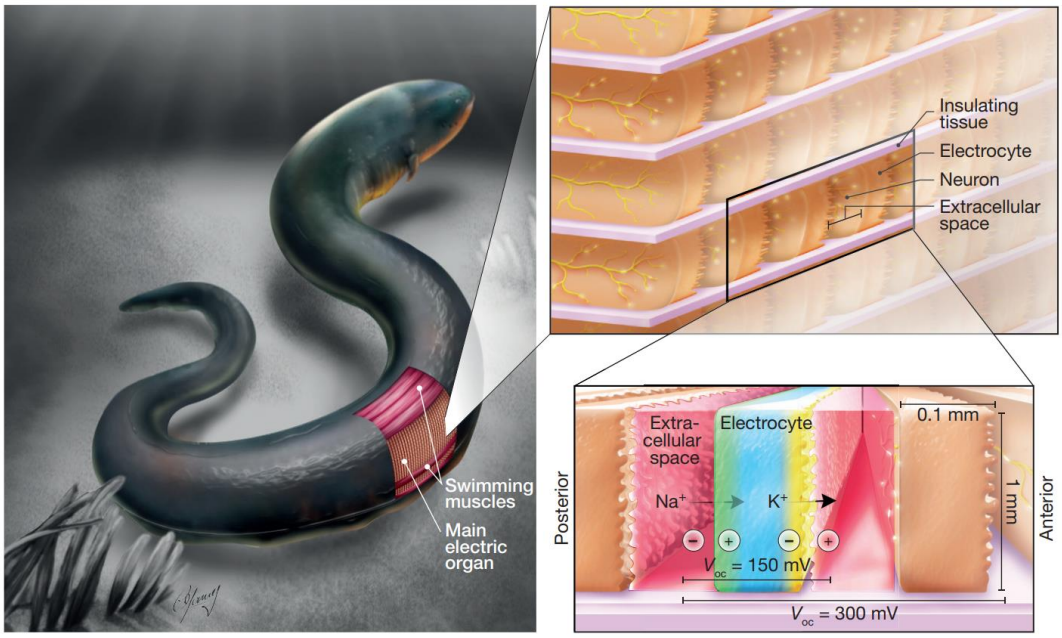

Figure 1.18 Morphology of the eel's electric organ and the artificial electric organ. The electrocytes are arranged within the electric organs of electrophorus electrics [107].

Very recently electronics-free RED patches have been developed to be used as an ionic power source for active transdermal drug delivery (Figure 1.19) [63]. This patch was composed of three pairs of IEMs and two Ag/AgCl electrodes at the end of a stack. Upon the injection of NaCl solutions with different salinities, this miniaturized electrodeless RED patch was activated generating an initial voltage of 0.478 ± 0.017 V. The generated voltages were proportional to the number of ion-exchange membranes and salinity ratios, which successfully facilitated the in vitro delivery of ionic drugs through mouse skin. The unique characteristics of such a salinity power system that only involves ion transportation during the energy generation process provides great compatibility with the human biosystem, as it wouldn't cause the decomposition of the electrolyte. Thus, it holds great applicability for an implantable

medical device or sensor, particularly when using a biocompatible ion exchange membrane such as conducting polymers-based ones.

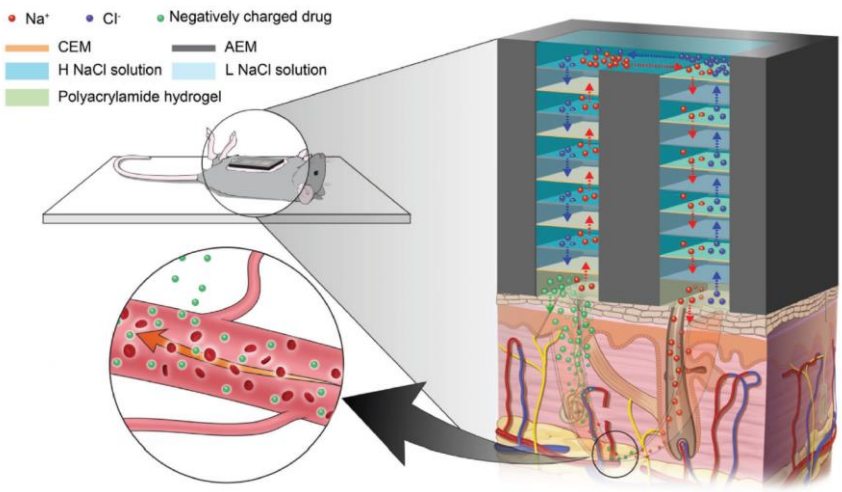

Figure 1.19 Schematic representation of an electrodeless reverse electrodialysis (RED) patch attached on the mouse skin. Ions (Na^+ and Cl^-) in the RED system selectively permeate from high-concentrated (H) NaCl solution to low-concentrated (L) one through a CEM and AEM, respectively. The negatively charged drug molecule penetrates the mouse skin while sodium ion moves toward the L solution through an CEM to maintain the electrical neutrality in the hydrogel [63].

1.4 Conducting polymers for bio-related energy application

The demand for developing a power source that can use body fluid as a component such as a bioelectric battery and an energy harvesting system has stressed the requirement of developing biocompatible materials with excellent electrochemical, electric and/or ionic properties. Conducting polymers (CPs) are unique materials that can meet all these merits with features of metallic conductivity, excellent electroactivity, ion permselectivity, and cytocompatibility [108, 109].

CPs, especially nanostructural CPs-based materials have been widely used in the research fields of batteries, supercapacitors [110], electroanalysis [111], and electrocatalysis [112]. Specific advantages of nanostructured CPs for these applications mainly include: (i) high electrode/electrolyte contact area facilitating high charge/discharge rates; (ii) short path lengths for electronic transport permitting the operation with low electronic conductivity; (iii) short path lengths for facilitating ions transport to the electrodes surface [113].

Apart from the electronic properties, CPs possess the ion-selective properties as well, thus they can be used as ion-exchange membranes [114]. For example, the defluoridation of water occurred via a polyaniline/chitosan (PANi/Ch) and polypyrrole/chitosan (PPy/Ch) membrane leading to an enhanced fluoride ion uptake [115]. It has also been demonstrated that the relative transport number of ions was changed after coating a PPy layer on a commercial cation exchange membrane [116]. The PPy layer with cationic charge restricted the permeation of Ca^{2+} resulting in a sieving effect for calcium ions.

1.4.1 Conducting polymers

CPs are polyconjugated materials composed of alternating single and double bonds forming π molecular orbitals [117]. They were discovered in 1970s [118]. CPs commonly exist in the form of polymer chains doped with counter ions [119-121]. The commonly used CPs in the energy area include polyaniline (PANi) [122], PPy [123], poly(3,4-ethylenedioxythiophene) (PEDOT) polystyrene sulfonate [124] and their corresponding derivatives. The structures of representative CPs are shown in Figure 1.20.

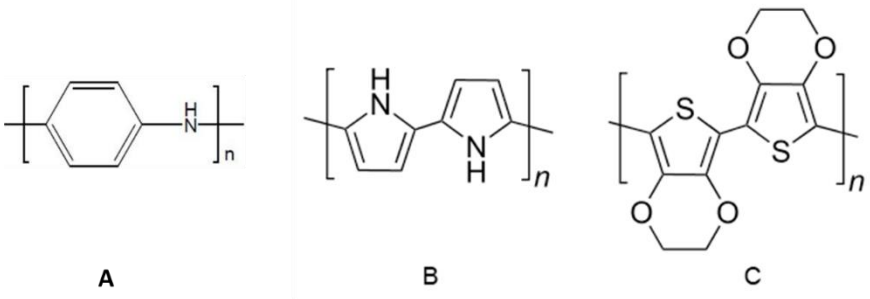

Figure 1.20 Schematic structures of A) PANi; B) PPy; C) PEDOT.

The doping process of a CP is realised via an oxidation or reduction reaction, which generates delocalized ‘p’ doping or “n” doping on the polymer chain. Specifically, positively charged polymers that are introduced by the oxidation on the repeating units of polymer chains are termed as ‘p-doped’; the negatively charged polymers generated by reduction are termed as ‘n-doped’ [125].

Both the oxidation and reduction reactions of CPs commonly involve the inward/outward movement of counterions. Take PPy as an example, counterions (such as Cl^-) are able to reversibly insert/extract (into/from) the polymer matrix during the reduction/oxidation processes. The reactions are shown in Figure 1.21. If the dopant anions are small and mobile, anion movement dominates for redox reactions. For a polymer with immobilised large size anions dopant, the redox reactions are predominantly accompanied by cations movement.

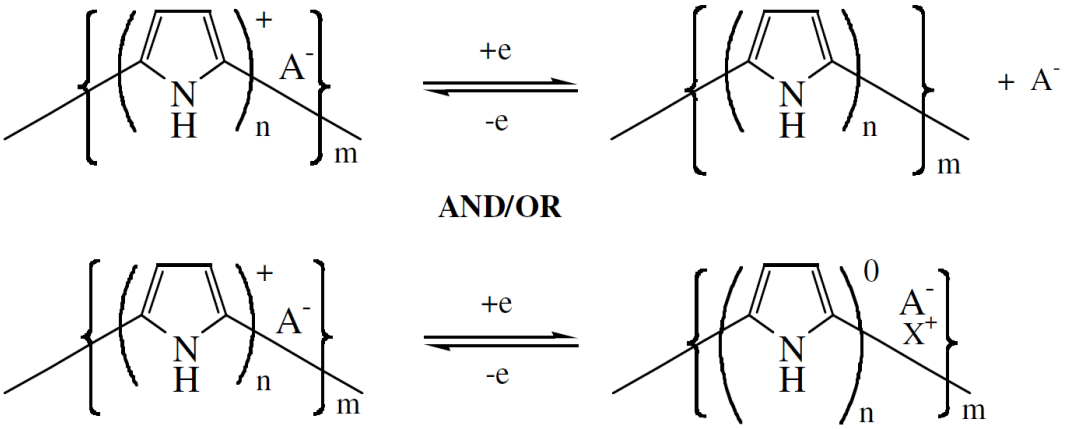

Figure 1.21 The electrodynamic character of PPy, where n is the number of monomer units per unit positive charge, A^- is a counterion incorporated during the synthesis, m determines molecular weight [126].

1.4.1.1 Synthesis of conducting polymers

CPs can be synthesized by chemical or electrochemical polymerization. Electrochemical polymerization is a common technique for producing CPs on a conductive substrate. The formation and doping of polymer are generally realised simultaneously. It can be achieved by using potentiostatic (constant potential), galvanostatic (constant current) or potentiodynamic methods (cyclic voltammetry, pulse deposition) [127]. This synthesis method is preferable for producing CPs with controllable size and thickness; as the yield in charge terms is close to 100% [128]. At a sufficiently high positive/anodic potential, monomers like aniline or pyrrole undergoes electrochemical oxidation yielding cation radicals or other reactive species which trigger the polymerization process [129].

In a chemical synthesis process, they are prepared by oxidizing monomer with oxidants such as $(NH_4)_2S_2O_8$, or $FeCl_3$ [130, 131]. The monomer is oxidised to form active cation radicals, which can react with monomers to yield oligomers and finally

insoluble polymers. Take the polymerization process of pyrrole as an example (Figure 1.22), a neutral molecule of pyrrole monomer yields a radical cation (a) with the assistance of an oxidant; then they combine, consecutively to form the bipyrrole dication and a neutral pyrrole dimer (b); finally the deprotonation and recombination steps (c) lead to the formation of PPy [132]. All CPs can be synthesized chemically, but the electrochemical synthesis is limited to those systems in which the monomer can be oxidized within the applied potential to form reactive radical ion intermediates for polymerization [117]. The major advantage of chemical polymerization is the possibility of mass-production at a relatively low cost [133].

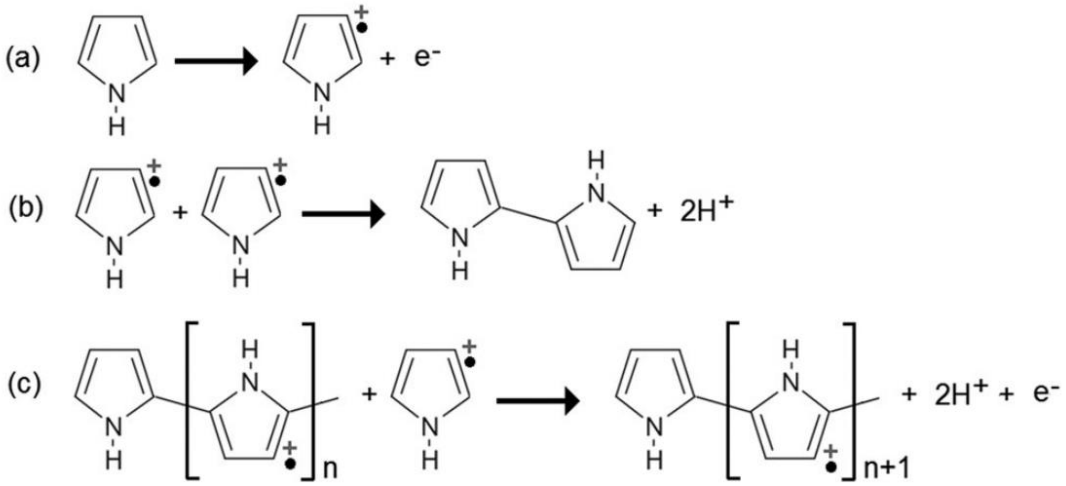

Figure 1.22 Scheme illustrates the chemical polymerization of pyrrole [134].

As a special subclass of CPs, nanostructured CPs not only retain features of CPs, but also have the characteristics of nanomaterials such as large surface area, fast electrolyte diffusion [135]. The growth of nanostructured CPs can be guided by different hard or soft templates [136] for producing various nanostructures such as nanofibres [137], nanotubes [138, 139], nanowires [140, 141], nanorods [142], and nanoparticle [143] (Figure 1.23).

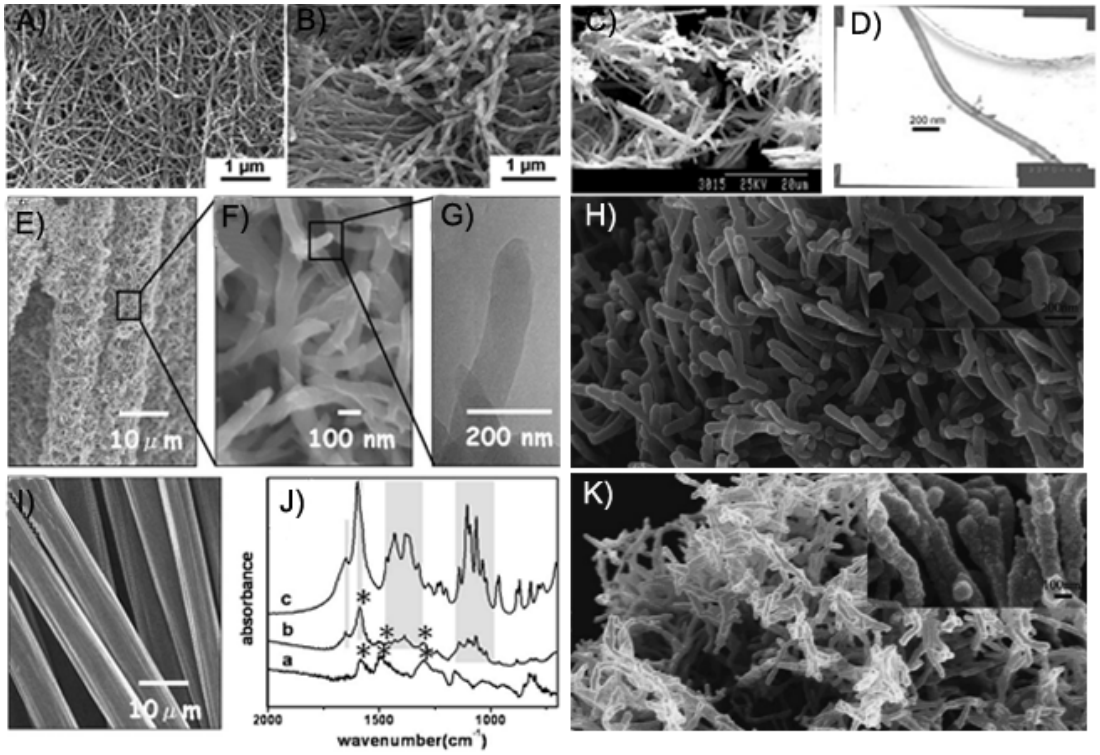

Figure 1.23 Conducting polymers in different nanostructures: A, B) Scanning Electron Microscope (SEM) images of PPy nanofibres [137]; C) SEM and D) Transmission electron microscope (TEM) images of PPy nanotubes [139]; E-G) and I) SEM images of PANI-NWs [141]; H) and K) SEM images of PPy nanorods [142].

The synthesis of nanostructured CPs via using inorganic templates such as silica, metal oxides, is called a hard-template method (Figure 1.24); while the soft-template method uses organic materials as template such as surfactants (Figure 1.25). The soft-template method has an advantage over the hard-template, in that, the soft template doesn't need to be removed with additional steps. Interfacial polymerization is an attractive soft-template method, which was proposed by Kaner et al. This method involves the polymerization process taking place at the interface between two immiscible liquids where the reactants are respectively dissolved [144]. This method is usually based on

a molecular self-assembly mechanism with hydrogen bonding, π–π stacking, van der Waals forces, or electrostatic interactions as the driving forces [145].

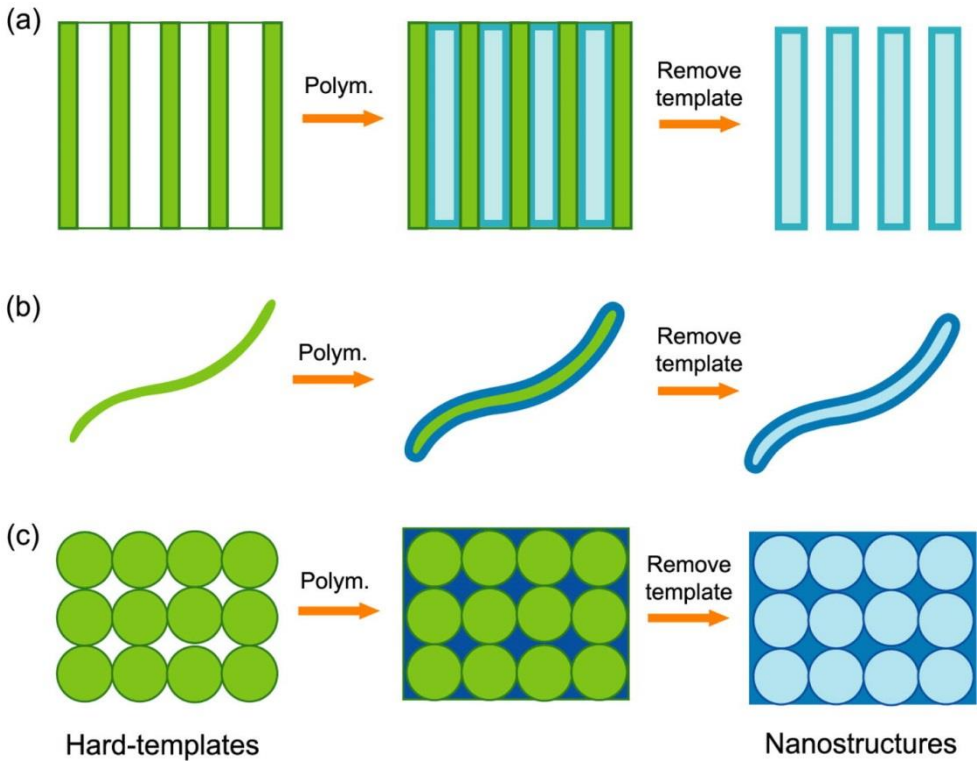

Figure 1.24 Schematic of the synthesis of nanostructured CPs using hard-templates. The growth of CPs are guided by various templates: a) porous membrane, b) nanofibres and c) colloidal particles; and then these templates are removed after the polymerization [146].

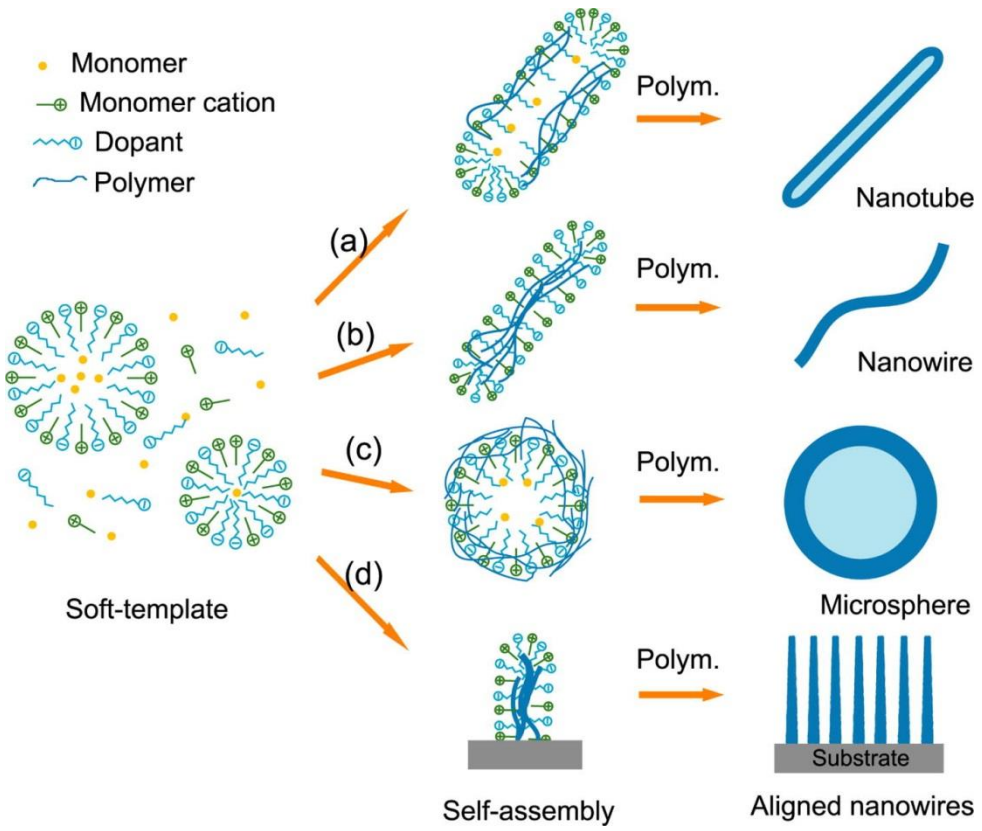

Figure 1.25 Schematic of the synthesis of nanostructured CPs with soft templates of a) micelles, b) dopants, c) monomer droplets; and d) a self-assembly process of molecules [146].

1.4.1.2 Factors affecting the properties of conducting polymers

During the synthesis process, all the factors such as dopants, oxidant, temperature, surfactants as well as the buffer solution affect the morphology and structure of the formed CPs [147, 148]. PPy doped with different anions can be electrochemically formed in different morphologies including fibrillar, spheroidal and film-like structure [149]. Conductivity of the produced CPs are affected by the synthesis conditions as well [128]. For example, PPy with the highest conductivity was obtained in methanol solution compared to that formed in water, alcohols, benzene, tetrahydrofuran, chloroform, acetone, acetonitrile (AN) and dimethylformamide; since the oxidation

potential of pyrrole was solvent dependent thus affecting the polymerization process [119]. It is also reported that conditions of dopants (i.e., $FeCl_3$ concentration) affected the electrical conductivity of PPy because it is related to the oxidation potential obtained in the oxidant[119]. Martin and his group found that template-synthesized nanostructural CPs have higher conductivity compared with bulk materials owing to the higher molecular and supermolecular order [150].

1.4.2 Properties of Conducting Polymers

Neutral CPs are insulators and can be converted into a semi-conductive or conductive state through redox reactions. This doping process makes the CPs backbone to possess positive (p-doping) or negative charge carriers (n-doping), which can attract counterions to be entrapped within the polymer matrix to maintain the charge neutrality [136]. This synergistic process endows CPs with electronic properties, electroactivity and ionic properties, which enable them to transduce between bioelectric signals (in the form of ionic current) and electric signals. The CP-based materials are electrically stable over a long period during implantation in tissue, non-biodegradable yet biocompatible [151].

1.4.2.1 Conductivity

Charge carriers are created by electron donating or electron accepting species at the polymer backbone, resulting in electron (n-type) or hole (p-type) conductivity [152]. CPs demonstrate a conductivity ranging from 10^{-5} to 10^{3} S cm^{-1} [128, 153, 154]. They are classified as semiconductors or even sometimes they possess metallic conductivity. Table 1.4 compares the conductivity of CPs, metals and insulators.

Table 1.4 Comparison of conductivity of CPs, metals and insulators [155, 156].

Property	CPs	Metals	Insulators
Electrical conductivity(S/cm)	10^{-11}-10^{3}	10^{-4}-10^{6}	10^{-20}-10^{-12}
Carriers	Polarons and bipolarons	Valence electrons of half- filled band	-

The conjugated backbone of CPs (Figure 1.26) is formed by a series of polymer units with alternating double bonds and singles bonds. These bonds all contain a chemically strong, localized σ-bond, while double bonds contain less strongly localized π-bonds as well. The *p*-orbitals in the series of π-bonds overlap each other, allowing the electrons to move freely between atoms. For CPs, the doping process generates charged polarons/bipolarons and these carriers are delocalized to facilitate electronic conductivity [157].

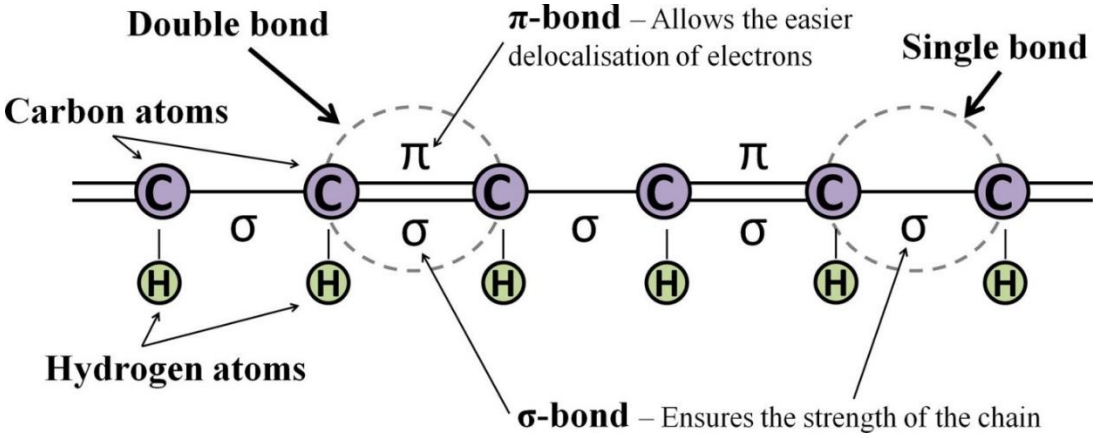

Figure 1.26 A simplified schematic of a conjugated backbone: a chain contains alternating single and double bonds [158].

The interaction of a polymer unit with all its neighbours leads to the formation of electronic bands [156]. The highest occupied electronic levels constitute the valence band and the lowest unoccupied levels form the conduction band. The state of energy of the band determines the intrinsic electrical properties of materials. The smaller the band gap energy for a CP, the more conductive it is [159]. Many factors can influence this band gap and the consequent conductivity, which mainly include dopant, oxidation level/doping percentage, and temperature [117, 160, 161].

1.4.2.2 Electroactivity

As described in Section 1.3.1, the doping/dedoping process of a CP typically leads to reversible structural changes. Take PPy as an example, the oxidised segments in the PPy chains are counterbalanced and incorporated with anions; when PPy is reduced, anions egress the polymer matrix to the electrolyte [128]. This reversible doping/dedoping process is the basic principle for energy application; including batteries and supercapacitors [157].

It is a unique characteristic of CPs that electron transition and mass changes are all being involved during the reduction-oxidation processes. The oxidation level of CPs is easily affected by the doping/dedoping process, which may result in a sensitive and rapid response to specific analytes [162]. The charge transport properties of CPs are changed and can be correlated quantitatively to the analytes concentration [163]. Most CPs have demonstrated electrocatalytic activity for ORR; as CPs in the reduced state can interact with oxygen and be oxidised [164, 165]. Specifically, a neutral CP acts as the electron donor while O_2 is an electron acceptor; namely, CP can strongly interact with O_2 molecules and activate O_2 by decreasing its molecular symmetry and increasing the lengths of O=O bonds [44]. It has been calculated that the oxygen

molecule can be adsorbed on the CP's surface, and bond orders in the chemisorbed oxygen molecules are almost 30% lower than those free O_2 molecules [45]. Thus, chemisorbed oxygen molecules have a fairly high degree of activation and can be readily reduced at the CP's surface. For example, PPy coated paper towel (Figure 1.27) is prepared by vapour phase polymerisation. The polymerisation takes place at the interface between oxidant and vaporous pyrrole monomer, where the oxidant is dropped on the paper tower [166, 167]. It displayed excellent ORR catalysis performance, with a reduction potential of −0.068 V (vs. $Hg|HgCl_2$), an onset potential of 0.014 V, and a half-wave potential of −0.061 V in 0.1 mol/L O_2-saturated KOH solution, which are more positive than those of Pt/C (−0.121, −0.042, and −0.109 V). Compared with a Pt/C catalyst, this PPy electrode demonstrated a higher stability and superior tolerance to methanol cross-over and CO-poisoning effects.

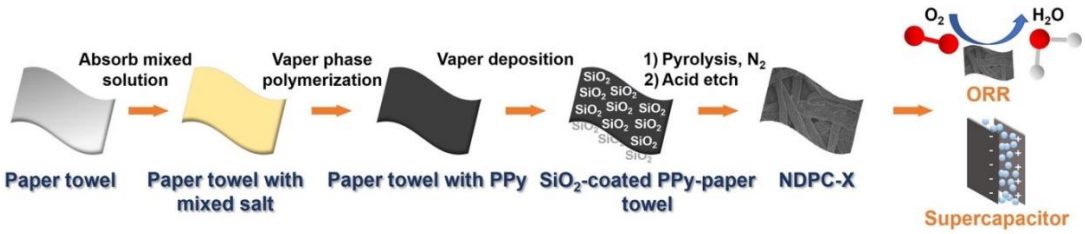

Figure 1.27 A schematic illustration of fabricating a PPy/paper towel electrode and its application as ORR catalyst [167].

1.4.2.3 Ion transport property

CPs are electroactive materials with a mixed electronic and ionic conductivity, which means that they can transduce an ionic signal in the solid state [168]. Under anodic polarisation, the polymer chain loses electrons to induce positively charged chains which attract the counterions to balance the polymer backbone and maintain electroneutrality [169]. The existence of positively charged atoms in CPs provides a

good prospect for ion selectivity [170]. Ion movement is highly related with the nature and number of the charged sites on the polymer backbone, and the changing of these features will change its ionic resistance [171]. CPs such as PPy can be called "ion gate membranes" with the permselectivity controlled by potentials, as the ion conductivity is strongly dependent on the oxidation state [172]. When PPy is oxidised cations are expelled from the polymer and anions are inserted (Figure 1.28) [173]. This leads to an increase in the doping level and oxidation state (oxidation). This occurs when a positive potential is applied. When a negative potential is applied, PPy switches to the reduced state with the concomitant expulsion of anions. With the re-applied positive potential, the polymer is re-oxidised and positive charges will return to the backbone. This process is reversible, and thus can control the direction of ion transport.

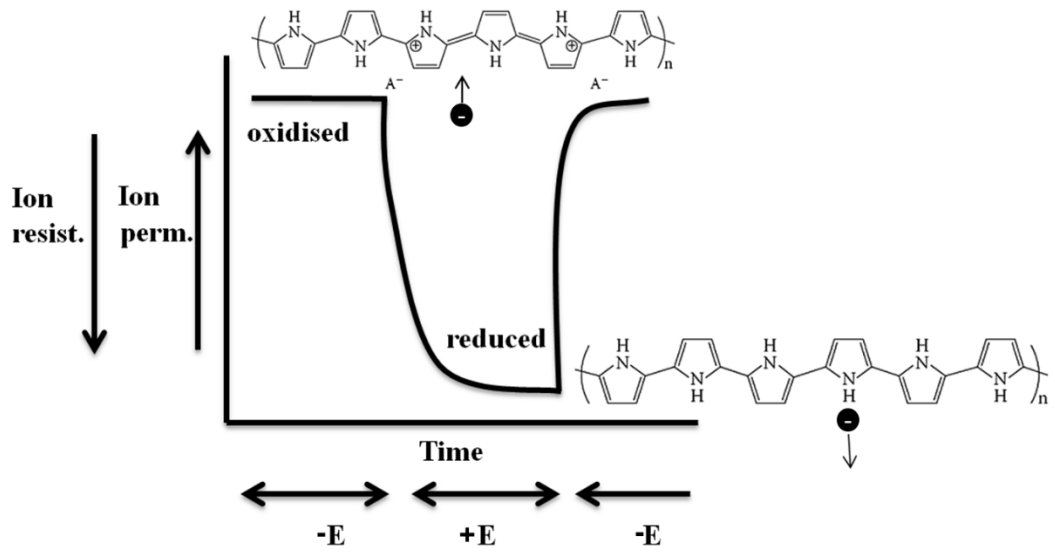

Figure 1.28 CPs whose state is switched between the cationic (oxidized) and neutral (reduced) by varying the applied potential [173].

The ion transport properties of PPy have been widely studied. [174]. T. Shimidzu *et al.* reported that the oxidation-reduction (doping-dedoping) processes in PPy was

influenced largely by the size of the incorporated anion (dopant)[175]. In the extreme case of large dopant molecules (i.e. PSS), they are immobilised within the CP matrix preventing the leaching from the polymer matrix. While at the other end for small dopants (molecules or ions), they can easily diffuse in and out of the CP matrix. Due to the multifunctionality of the chemical compositions and the asymmetries in structure and surface charge polarity, PPy/poly(acrylamide-co-acrylic acid) membrane is also reported to be capable of rectifying counterions transmembrane transport in response to both electro- and pH-stimuli (Figure 1.29) [176].

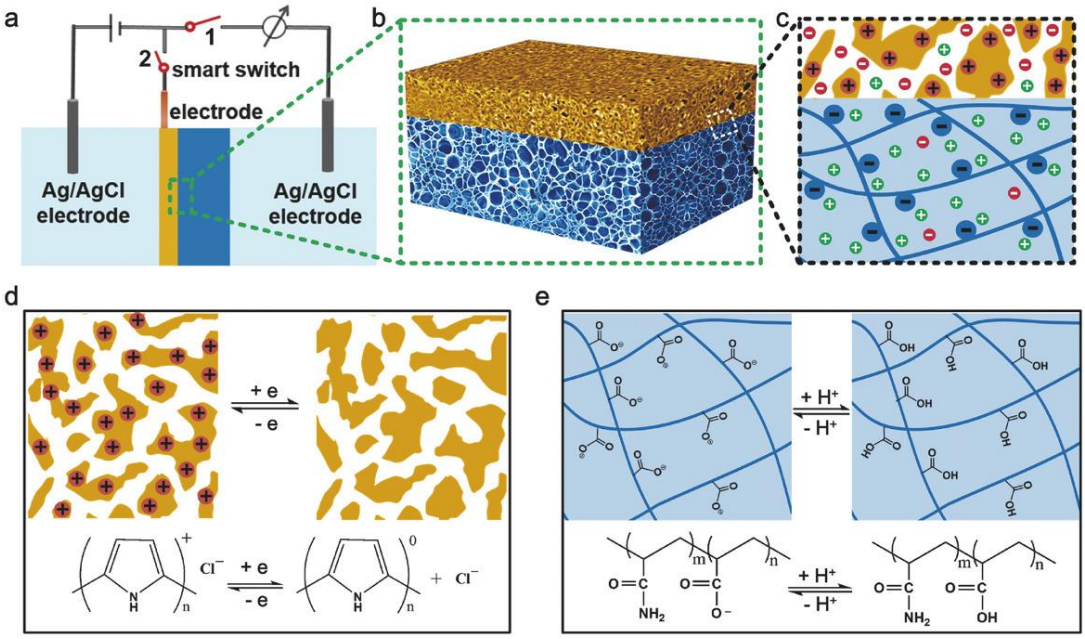

Figure 1.29 3D porous hydrogel/conducting polymer heterogeneous membrane and its electro-/pH-responsive ionic rectification properties: (A) Illustration of the electrochemical device to investigate the ionic transport properties. (B, C) PPy/ poly (acrylamide-co-acrylic acid) membrane with asymmetric structure, surface charge density. (D) PPy layer can be modulated by extracting/injecting electrons. (E) Charge density of poly (acrylamide-co-acrylic acid) layer can be changed by varying the pH of the solution [176].

1.4.2.4 Biocompatibility

CPs are widely used in biological systems; with good capacity to support and regulate the growth of various cells such as nerve cells and bone cells [177]. In the physiological environment, electrical charges play an important role in stimulating cell proliferation or differentiation [178-180]. For example, neurite outgrowth is enhanced on electrets such as polyvinylidene fluoride [181]. With the growing knowledge of the electrical properties of tissues and cells [182], electrical stimulation (EL) become an active tool to control cell behaviour and function for the basic research and future translational applications [183, 184]. EL has been used to modulate the differentiation of multiple cell types such as bone cells [185, 186], and neural cells [158, 187].

Considering their good electrical properties, biocompatibility and good mechanical property, CPs may be used as bioelectrodes in an electrical stimulation system to modulate cellular activities by providing a soft bio-interface with low impedance [188, 189]. CPs have shown their potential to regulate the shape and function of adherent cells [190], modulate the cellular activities including cell adhesion, migration, and DNA synthesis via an electrical stimulation [191, 192]. These studies involve a wide application in the nerve, bone, muscle, and cardiac cells.

Among these CPs, PPy is the most attractive candidate due to its biocompatibility, mild synthesis processes, excellent electronic property and electroactivity [128]. For example, Schmidt *et al.* demonstrated that PPy could promote cells differentiation with an applied electrical stimulation [193]. Wallace *et al.* demonstrated that polypyrrole/poly (2-methoxy-5 aniline sulfonic acid (PPy/PMAS) composites could support nerve cell (PC12) differentiation; the clinically relevant 250 Hz biphasic current pulses delivered via PPy/PMAS films significantly promote nerve cell

differentiation in the presence of nerve growth factor (NGF) (Figure 1.30) [194]. Another reason of its wide use is that PPy can be electropolymerized in an aqueous media at neutral pH, which allows the incorporation of various biological counterions (e.g., proteins) [195]. PPy can also be modified with functional negatively charged ions such as adhesive peptides that are tailored for enhancing the material-cell interactions by creating biological molecules coating for cells attachment [196]. Other types of CPs are more limited in this regard. For example, the oxidation of aniline in mildly acidic, neutral or even alkaline media yields non-conducting oligomers [197].

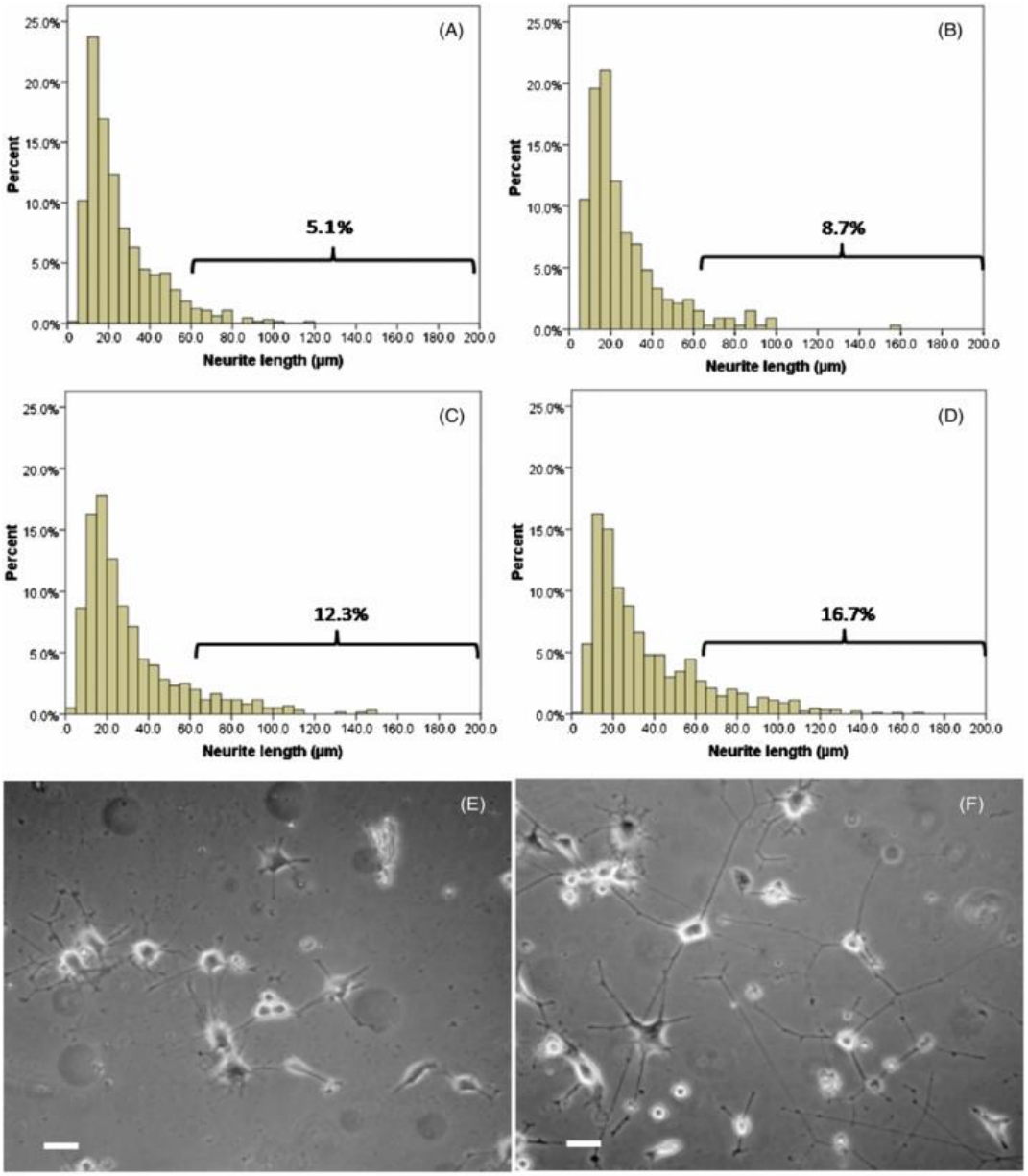

Figure 1.30 Neurite length histograms of PC12 cells on PPy/PMAS film without (A) and with 10 Hz (B), 100 Hz (C) and 250 Hz (D) electrical stimulation. Phase-contrast images of PC12 cells on PPy/PMAS films without (E) and with (F) 250 Hz electrical stimulation. The scale bars are 20 μm [194].

Due to their reversible doping/dedoping process, CPs, as discussed in 1.4.2.2, can entrap and controllably release biological molecules (reversible doping), thus they

may make themselves suitable for biomedical applications such as tissue-engineering scaffolds, biosensors, neural probes, drug-delivery systems, and actuators [117, 198-201].

1.4.3 Conducting polymer hydrogels

Conducting polymer hydrogels (CPHs) are interesting materials, wherein electronic conductivity is introduced into a hydrogel structure with little compromise of the physical properties [202]. CPHs are a unique subclass of CPs that are electrically conductive as well as capable of water swelling/deswelling. CPHs are extremely suitable for a variety of bio-applications [203, 204] due to their electrical properties and their mechanical properties compared with biological tissues [188]. Their representative applications are illustrated in Figure 1.31; including bioelectrodes, biosensors, energy field, and tissue engineering [205].

This type of 3D interconnected conductive porous structure creates an ideal cell-electrode interface for cell growth and differentiation [205]. For example, PEDOT–agarose hydrogel had a demonstrated application in axonal regeneration. It supported superior neural regeneration due to the improved diffusion of nutrients and biomolecules into the lumen of conduits [110]. A flexible micropatterned PEDOT/agarose hydrogel electrode was developed for cultivating contractile myotubes [206]. Upon an electrical stimulation, the contraction of PEDOT nanotubes produced a mechanical force which created pressure to expel the loaded drugs [207]. Alginate hydrogel with grown PPy has been used in a microfabricated neural prosthetic device for improving neural recording [208]. Acryloyl-6-aminocaproic acid hydrogels is used as tissue adhesives in rabbit gastric mucosa [209]. A moisture-activated copolymer hydrogel comprised of methyl binyl and maleic anhydride can be

used as bioadhesive films to neonate porcine skin as interfaces for the operation in a wet environment [210].

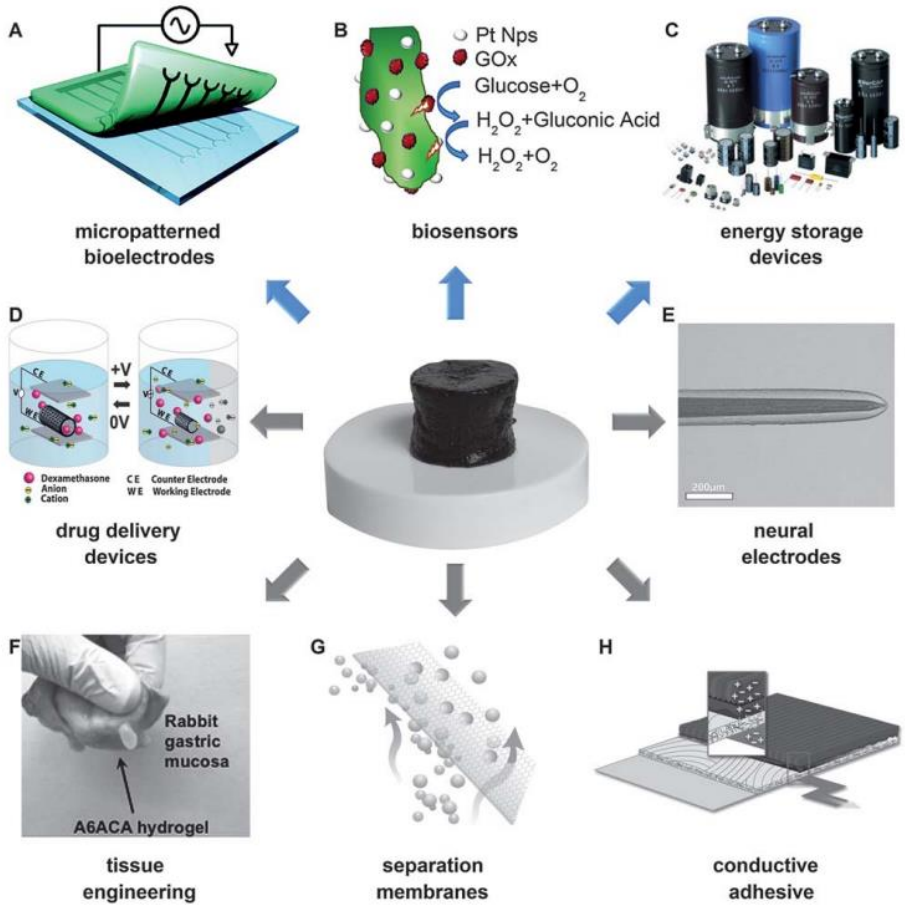

Figure 1.31 Representative applications of CPs hydrogels [205]: A) Bioelectrodes [206], B) Biosensors [211], C) Energy storage devices, D) Drug delivery [207], E) Neural electrodes [208], F) Tissue engineering [209], G) Separation membranes, and (H) Conductive adhesives [210].

Typically, CPHs are prepared by incorporating a CP with a non-conductive hydrogel. As illustrated in Figure 1.32 [205], the common routes for CPHs synthesis mainly include: 1) Dehydrated hydrogel is re-swollen in a CP monomer solution, and the confined CP monomer is chemically or electrochemically polymerized on the

hydrogel template [212]; 2) Hydrogel is fabricated with a template filled with CP monomer, and the polymerization is conducted inside the hydrogel network [213]; 3) Hydrogel is made from the mixed precursors including hydrogel and CP monomer, these two components are polymerized simultaneously or separately [214].

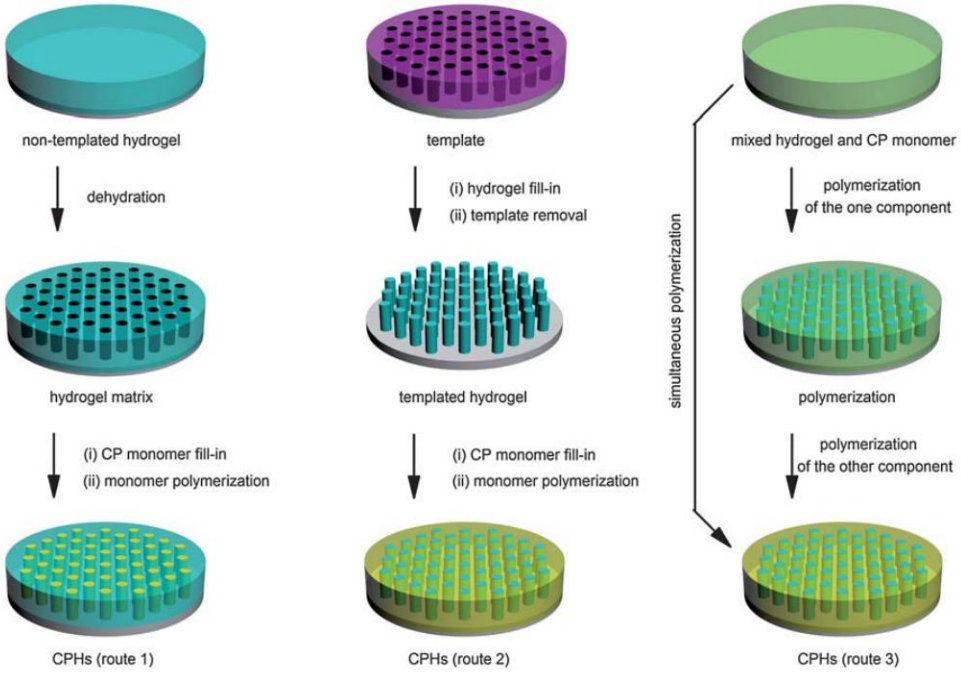

Figure 1.32 Representative methods for the formation of CPHs [205].

1.5 Thesis objectives

Active implantable medical devices (AIMDs) have achieved great breakthroughs over the past six decades with the progressive development in science and engineering, especially in microelectronics, biotechnology, and materials. As a core component of an AIMD, currently the power source is still predominated by Li batteries. They need an absolute encapsulation or housing to prevent any leakage of toxic substances into the human body, which inevitably results in a bulky size occupying a large space and

weight of the device. They are the limiting factors governing the miniaturisation of AIMDs. New types of biocompatible and reliable power sources are highly desirable. It would be ideal if a power source (e.g., energy storage/generation) could directly use the body fluid as one component when coupled with cytocompatible materials. CPs are ideal materials based on its electroactivity, electroconductivity, cytocompatibility and ionic conductivity. Therefore, the work in this thesis mainly focuses on the development of cytocompatible CPs for bionic-related energy applications; including a metal-air battery system and a salinity power generation system.

In this thesis, the bioelectric battery uses culture media as an electrolyte, a bioresorbable metal anode (Mg or Fe) anode and a biocompatible conducting polymer cathode. Both Mg and Fe are essential elements for the human body. This type of battery has the potential for direct implantation without the need of a case. The performance of a bioelectric battery is mainly determined by the cathode. To achieve an excellent battery performance, an efficient cathode material, CPH, has been developed, which integrates the structural merits of a hydrogel - 3D interconnected porous structure, with the inherent electrochemical properties of a conducting polymer - high conductivity, biocompatibility, and electrocatalytic ability to ORR.

Apart from the bioelectric battery, in this thesis another promising power source that uses a cytocompatible conducting polymer film as an ion exchange membrane to harvest the energy from the salinity gradient has been researched. This salinity gradient power has the potential to utilize that gradient between the intracellular and extracellular fluid. In addition, ion conductance of this PPy membrane is tunable via an applied potential due to the redox-active properties of the CPs.

A brief introduction of these works in this thesis is described below.

In Chapter 3, a robust conductive hybrid PPy/PEDOT hydrogel is developed. It is realized by electrochemically depositing PPy onto a PEDOT hydrogel that is prepared by a two-step cross-linking process. This hydrogel offers good electrochemical properties due to its 3D interconnected porous structure facilitating ions and electrons transportation, as well as good cyto-compatibility for supporting cell proliferation. The battery assembled with this hybrid hydrogel cathode and a Mg alloy anode possesses high capacity, high rate and high energy density in the culture media electrolyte. It can be anticipated that the energy generated from this type of bioelectric battery may be directly used to modulate cellular activities cultured on the hydrogel without need of an external power supply.

In Chapter 4, further consideration is given for the development of this type of bioelectric battery with the use of an Fe anode substituting Mg alloy, as Fe is an important element involved in the activities of cytochromes and many enzymes. This battery can provide a stable potential and power. Human adipose stem cells proliferate well on the hydrogel cathode in this battery. The degradation rate of Fe is also increased when this bioelectric battery is subjected to a discharging period compared to that static Fe corrosion/at the open circuit state. This novel Fe-air battery may provide a new avenue for solving the slow degradation problem of a Fe stent for angioplasty, as well provide energy for biological activities such as cell migration.

In Chapter 5, a single component PPy membrane is developed via a simple interfacial polymerization process. This membrane can work as an ion exchange membrane in a salinity energy harvesting system, generating a stable power from the use of artificial seawater and river water. Moreover, this membrane provides asymmetric wettability on either side, cytocompatibility and an electrochemically tunable ionic conductance.

These features make this membrane a promising material for biomimetic membraned-based energy conversation.

Chapter 2 Experimental Methods

In this chapter, chemicals and materials used in this doctoral work are summarized and presented, as well as the general preparation methods of materials and characterization techniques.

2.1 Chemicals and Reagents

Chemical reagents and materials used in this work are listed below. They were used as-received without further treatment unless otherwise stated.

Table 2.1 List of chemical reagents and materials used in this thesis.

Reagents and Materials	**Company**	**Tasks**	**Chapters**
PEDOT: PSS pellets	Agfa Company	Synthesis of PPy/PEDOT hydrogel	**3,4**
Magnesium nitrate	Sigma-Aldrich		**3, 4**
p-Toluene sulphonic acid	Sigma		**3, 4**
Pyrrole	Merck	Synthesis of PPy/PEDOT hydrogel,	**3, 4, 5**

		Synthesis of PPy membrane	
Chloroform	ChemSupply		**5**
Iron (III) chloride	Sigma-Aldrich		**5**
Tween-80	Sigma-Aldrich		**5**
Magnesium Alloy	Goodfellow company	Anode in a magnesium-air battery	**3**
Iron Alloy	Goodfellow company	Anode in an iron-air battery	**4**
Stainless Steel	Hongye Stainless Steel Wire Cloth Co. Ltd.	As the conductive substrate	**3,5**
PC12 cells	Dr. Anita Quigley at St Vincent's Hospital (Melbourne)	-	**3**
Commercial human adipose-	Lonza company		**3,4,5**

derived stem cells (hADSCs)		-	
Fetal bovine serum (FBS)	Life technologies	Culture media	**3, 4, 5**
Basic fibroblast growth factor (βFGF)	Life technologies		**3, 4, 5**
Penicillin-Streptomycin	Life technologies		**3,4,5**
β-glycerophosphate	Sigma-Aldrich	Differentiation media	**3**
Dexamethasone	Sigma-Aldrich		**3**
Ascorbate acid	Sigma-Aldrich		**3**
Nerve growth factor	Sigma-Aldrich		**3**
Calcein and Propidium Iodide (PI)	Life technologies	Fluorescence imaging	**3,4,5**

Alizarin Red S (ARS)	Life technologies	Characterization of cell proliferation	**3**
Paraformaldehyde	Fluka		
PrestoBlue™	Invitrogen		**3,4**
Alkaline Phosphatase Activity Fluorometric Assay Kit	BioVision Inc.	Characterization of cell differentiation	**3**
Ethanol	Ajax Fine Chemicals	Sterilization of materials	**3,4**
Sodium chloride	Ajax Fine Chemicals	Electrolyte	**5**
Sodium potassium	Ajax Fine Chemicals		**5**

2.2 Synthesis of materials

Here only the introduction of general synthesis and preparation methods are described. Detailed preparation procedures and the specific experimental works are included in the following corresponding chapters.

Chapter 3 describes the preparation of a PPy/PEDOT hydrogel electrode. The fabrication procedure includes an ionic crosslinking process of PEDOT dispersion

with magnesium nitride solution and a subsequent electrochemical deposition process. This PPy/PEDOT hydrogel is used as the electrode in a Mg-air battery system as well in an Fe-air battery in Chapter 4. Chapter 5 develops a single component asymmetric PPy membrane for salinity power generation via an interfacial polymerization.

2.3 Cell analysis

Cell viability assays are generally used for determining if the testing materials/molecules have effects on cell activity or show direct cytotoxic effects that eventually lead to cell death. Two different cell lines (hADSC and PC12 cells) were used to thoroughly assess the cytocompatibility of conducting polymer materials which may be potentially used for various medical purposes.

hADSCs are a kind of mesenchymal stem cells that can be differentiated to many different lineages including chondrogenic, osteogenic, adipogenic and neural [215]. PC12 cells is a cell line derived from the pheochromocytoma of the rat adrenal medulla that have an embryonic origin from the neural crest[216].

Both were used to test the cytocompatibility of hydrogels and membranes developed in the work. Differentiation of these two cells was also researched on the hydrogel with application of electrical stimulation.

2.3.1 Cells culture

The hADSCs culture media was prepared by mixing DMEM (low glucose) supplemented with 10% (v/v) FBS, 1% penicillin-streptomycin, 1% non-essential amino acids (NEAA) and 1 ng/ml basic fibroblast growth factor (βFGF). Cells were cultured in a T-75 flask supplemented with 15 ml culture media in a humidified incubator at 37 °C with 5 % CO_2 atmosphere.

PC12 cells were maintained in a T-25 plastic plate in 5 mL DMEM with 10% horse serum, 5% FBS and 1% penicillin-streptomycin. Specifically, the hydrogels were covered with the prepared collage coating solution (0.04 mg/mL) (Table 2.2) and incubated at 4° overnight.

Table 2.2 Collage coating solution.

	V_t (µL)	V_1(µL)	V_2(µL)	V_3(µL)	V_4(µL)
0.04 mg/mL	400	3.2	40	0.08	356.72

V_t: Total volume, V_1: collagen volume (5mg/mL), V_2:10× PBS solution, V_3:1N NaOH, V_4: Milli-Q water

2.3.2 Cell proliferation

Cell proliferation was studied using PrestoBlue cell viability reagent in accordance with the manufacturer's protocol. Specifically, at the selected day, cells were incubated in 10% Prestoblue (in culture media) for 1h.

For fluorescence analysis, cells were visualized using Live/Dead (calcein-AM/PI) staining with 2 µm Calcein AM and 4 µM PI in PBS. Images were obtained using a ZEISS Axio Imager microscope (Carl Zeiss). Fluorescence was measured by use of a plate reader with a 544 nm excitation filter and a 590 nm emission filter.

2.3.3 Cell differentiation

To induce the osteogenic differentiation, hADSCs were seeded on substrates in culture media and allowed to proliferate 7 days before transferring to differentiation medium (culture media supplemented with 10 mM β-glycerophosphate, 10 nM dexamethasone,

and 25 mM ascorbic acid). Alkaline phosphatase (ALP) activity was determined with Alkaline Phosphatase Activity Fluorometric Assay Kit.

To induce the nerve differentiation of PC12 cells, 50 ng/ml nerve growth factor were added to the culture media. For differentiation characterization, PC12 cells were fixed by the 3.7% paraformaldehyde and visualized with β-III tubulin staining by following the manufacturer's instructions.

2.3.4 Electrical stimulation

PPy/PEDOT hydrogels on a non-toxic stainless-steel mesh were adhered on the acrylic chamber with Flowable silicone sealer (ITW Permatx Inc, USA) as a working electrode. Cells were directly seeded on the hydrogel, and after 72 hrs the culture medium was replaced by osteogenic medium; then the electrical stimulation was applied. Cells were stimulated for 7 days in the incubator, 4 hrs per day. It should be noted that a one-day rest is needed for the cells' recovery after a 3-day continuous stimulation. Electrical stimulation was performed through a two-electrode setup, with a counter platinum electrode placed on the top of the chamber that is parallel to the bottom hydrogel electrode (Figure 2.1). hADSCs were seeded on the hydrogel samples and stimulated at 0.25 mA/cm^2 using a biphasic waveform of 100 ms pulses with 20 ms interphase and a 3.78 ms short circuit (250 Hz) using a Digital A310 Accupulser (WPI) and A315 Isolator units (WPI). Control samples were prepared by using the same method but without the use of electrical stimulation.

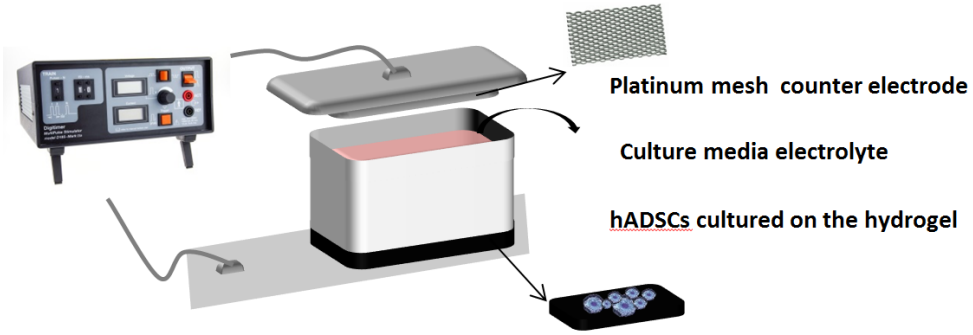

Figure 2.1 Cell stimulation setup: A home-made cell stimulation device.

2.4 Bioelectric battery assembly

All the cathodes used in this thesis were conducting polymer-based materials: PPy/PEDOT hydrogel or PPy membrane. These materials were conductive, thus they were directly used as electrodes without using conductive additives and binders.

The magnesium-air battery or Fe-air battery were fabricated by being assembled into acrylic chambers as shown in Figure 2.2. The cathode and anode were respectively adhered on two pieces of acrylic chamber as top and bottom part. The middle chamber was to contain electrolyte. These chambers were connected and fixed with four long screws, and thus a battery setup was assembled. This set-up is also used for the battery testing.

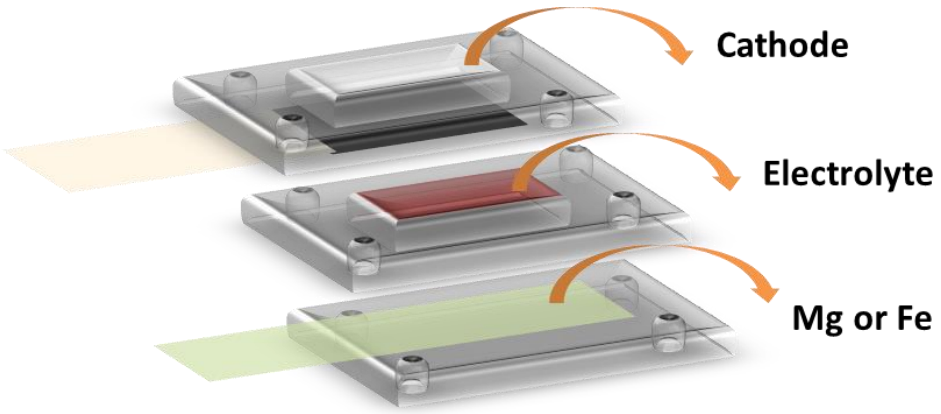

Figure 2.2 Configuration of a magnesium-air battery or an Fe-air battery.

2.5 Characterization techniques

Properties of the hydrogel and membrane developed in this thesis were characterized using physicochemical characterization techniques and electrochemical characterization methods.

2.5.1 Physicochemical properties characterization

2.5.1.1 Scanning electron microscopy and energy-dispersive X-ray spectroscopy

Scanning electron microscope (SEM) uses a focused beam of high-energy electrons to generate a variety of signals at the surface of solid samples for morphology analysis. For imaging in the SEM, specimens must be electrically conductive at the surface and electrically grounded to prevent the accumulation of electrostatic charge at the surface. Those non-conductive samples or with low conductivity are usually coated with an ultrathin layer of electrically conductive material such as gold or platinum.

A specimen is normally required to be completely dry to avoid gas molecules interfering with the electrons emitted from the sample, as SEM is operated at very high vacuums. Living cells and tissues require chemical fixation to preserve or stabilize their structures. Fixation is usually performed by incubating in a solution of buffered chemical fixatives, such as glutaraldehyde or formaldehyde. The fixed cells or tissues are then dehydrated with organic solvents such as ethanol or acetone or a freeze drying process, as the conventional air-drying can cause cells collapse and shrinkage. All the SEM images in this work were taken by using a JEOL JSM7500 FA cold-field emission gun scanning electron microscope. All samples were mounted with carbon tape on aluminium stubs.

Energy-dispersive X-ray spectroscopy (EDX) is an analytical technique used for the elemental analysis or chemical characterization of a sample. It relies on an interaction of some source of X-ray excitation of the sample. Initial EDX analysis usually involves the generation of an X-ray spectrum from the entire scan area of the SEM. The spectrum of X-ray energy versus counts is evaluated to determine the elemental composition of the sampled volume.

2.5.1.2 X-ray photoelectron spectroscopy

X-ray photoelectron spectroscopy (XPS) is a surface-sensitive quantitative spectroscopic technique that measures the elemental composition, empirical formula, chemical state and electronic state of the elements within a material. In this thesis, XPS spectra were obtained using a Bruker D8 Focus system to determine the redox state of PPy.

2.5.1.3 Inverted microscopy

An inverted microscope is a microscope with a light source and a condenser on the top, while the objectives and turret are below the stage pointing up. It is useful for observing living cells or organisms at the bottom of a larger container (e.g., a tissue culture flask) under more natural conditions than on a glass slide, as the case for a conventional microscope. As all the materials in this work are totally black and opaque, they can't be visualised by a conventional microscope whose light is below the samples. The images were captured using a camera and recorded by a computer. The optical microscope system used in this work was a Zeiss Axiovert microscope.

2.5.1.4 Thermogravimetric analysis

Thermogravimetric analysis or thermal gravimetric analysis (TGA) measures the thermal stability of a material and the rate of weight loss as a function of temperature or time. The mass of a sample is monitored when it is heated or cooled at a predetermined rate. This technique provides valuable information on the composition, thermal stabilities, and oxidative stabilities of samples. In this thesis, TGA measurement was conducted by heating the samples from room temperature to 600 °C at a heating rate of 10 °C min^{-1} under nitrogen flow (90 mL min^{-1}) using a Q500 TGA analyser (TA Instruments, UK).

2.5.1.5 Fourier-transform infrared spectroscopy

Fourier-transform infrared spectroscopy (FTIR) is a technique used to obtain an infrared spectrum of absorption or emission of a solid, liquid or gas. The instrument used in this thesis was a Shimadzu AIM8000 spectrometer with attenuated total reflectance mode (ATR). ATR has advanced to become the standard FTIR sampling technique, providing excellent data quality combined with high reproducibility.

2.5.1.6 Atomic absorption spectroscopy technique

Atomic absorption spectroscopy is an analytical technique that measures quantities of chemical elements by measuring the absorbed radiation. Every atom has its own distinct pattern of wavelengths at which it will absorb energy, due to the unique configuration of electrons in its outer shell [217]. It's a fast and easy technique with an extremely high sensitivity. In this thesis, Agilent AAS -240 equipment is used to measure the Fe concentration at a current of 5 mA and a wavelength of 372 nm.

2.5.1.7 Sheet resistance

Sheet resistance (R_s) of thin films (Ohms-per square) is commonly measured by use of four-point probe based instruments. It is defined as the resistivity of a material divided by its thickness (R_s = resistivity/thickness). A four-point probe is used to avoid contact resistance, which often has the same magnitude as the sheet resistance. Typically, a constant current is applied to two outer probes, and the potential on the other two inner probes is measured with a high-impedance voltmeter. In this thesis, the sheet resistivity was measured with a Jandel RM3 Conductivity Meter using a four-point probe method.

2.5.1.8 Mechanical properties

The mechanical properties of a material are those properties that involve a response to an applied load, including elasticity, yield strength, ultimate tensile strength and ductility. Compressive stress-strain measurements were performed using a Shimadzu EZ-L universal mechanical tester at a crosshead speed of 1 mm/min. The Young's modulus was calculated using the slope of the stress-strain curve. Rheological experiments were performed on a TA AR-G2 rheometer with a parallel plate configuration (12 mm diameter) at a constant strain and a constant normal force.

2.5.2 Electrochemical properties characterization

Electrochemistry provides an analytical tool for analysing the kinetics of charge transfer processes. Cyclic voltammetry (CV), electrochemical impedance spectroscopy (EIS) and galvanostatic charge/discharge technique are three main methods in this thesis to characterize the electrochemical properties of materials, electrodes or batteries.

2.5.2.1 Cyclic voltammetry

Cyclic Voltammetry (CV) is an electrochemical technique used to probe the nature of electrochemical redox processes. CV is performed by applying a cyclic potential on a working electrode, and measuring the resulting current. An electrochemical cell with a three-electrode setup consists of a reference electrode, a working electrode and a counter electrode, as shown in Figure 2.3. Before experiments, the counter electrode (stainless steel mesh) was cleaned by being sonicated in ethanol and subsequently rinsed with distilled water. The CV measurements were conducted using a CHI 650D electrochemical workstation (CHI Instruments, USA).

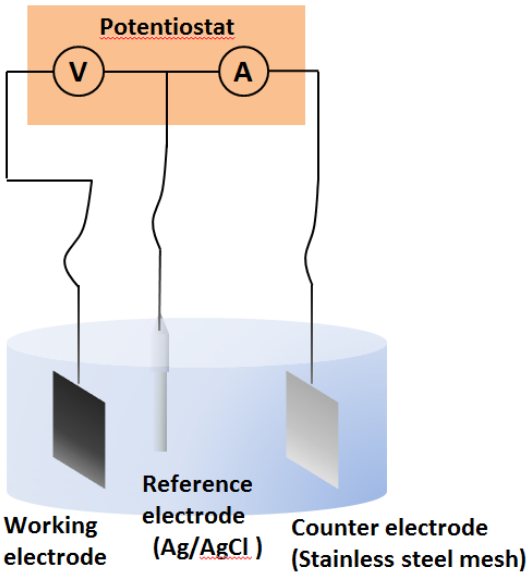

Figure 2.3 A three-electrode electrochemical setup.

2.5.2.2 Electrochemical impedance spectroscopy

EIS is a non-destructive electroanalytical tool used to determine kinetic parameters of an electrochemical system. It can be used to evaluate materials of electrodes and devices (e.g., batteries, capacitors). During an EIS test, a small amplitude AC-signal

is applied to measure the response and compute the impedance (both resistance and reactance) at each frequency. The complex response of the system is usually displayed in Nyquist format and Bode plot. A Nyquist plot is a plot of the imaginary part versus the real part over the scanned frequency range. A Bode plot consists of a resistance plot or a phase plot which is the resistance or phase as a function of frequency. In this thesis, EIS tests were performed using a Gamry EIS 3000TM system with an AC amplitude of 10 mV at open circuit potential.

2.5.2.3 Galvanostatic charge/discharge technique

Galvanostatic charge-discharge test is a commonly used method to evaluate the electrochemical energy storage of materials. For this technique, current is commonly controlled and voltage is measured. This method is a powerful technique to provide various parameters for evaluating energy storage devices such as capacity/capacitance, rate capability, cyclability, and self-discharge. In this thesis, galvanostatic charge/discharge tests were performed using a battery test system (Neware Electronic Co., Ltd).

Chapter 3 A cytocompatible robust hybrid conducting polymer hydrogel for use in a magnesium battery

This chapter is adapted from the article, "A cytocompatible robust hybrid conducting polymer hydrogel for use in a magnesium battery", by *Changchun Yu, Caiyun Wang, Xiao Liu, Xiaoteng Jia, Sina Naficy, Kewei Shu, Maria Forsyth, and Gordon G. Wallace, that was published in Advanced Materials 28, no. 42 (2016): 9349-9355, with permission from the Royal Society of Chemistry.*

3.1 Introduction

The advent of bionic materials that utilise electrical stimulation to promote tissue regeneration has highlighted the need for integrated energy storage systems [218, 219]. Mg-air battery is a promising candidate with high energy density and high discharge voltage attainable. Moreover, Mg or Mg alloys are also bioresorbable, suitable for implantable work [31, 220].

A high performance Mg-air battery requires an efficient cathode with a highly porous structure facilitating ORR [27, 36, 37]. Porous architectures with high specific surface

areas and larger pore volumes, not only maximize the availability of electron transfer but also provide better mass transport of reactants [221]. CPs possess the merits of high conductivity, biocompatibility and catalytic ability towards the ORR. The use of CPs in biocompatible Mg batteries with a biological electrolyte has been demonstrated previously [222-224]. However, CPs membranes have the limitations in the biological field due to their rigid mechanical property.

Hydrogels are suitable for a variety of bio-applications due to its matchable mechanical property to tissues [203, 204]. Conducting hydrogels used in tissue engineering typically consist of nonconductive scaffolds with a CP coating layer [208, 225]. These hydrogels possess excellent mechanical properties, however, they suffer from low electroactivity and hence are not suitable for application in batteries. CPHs wherein electronic conductivity is introduced into the structure with little compromise of the physical properties are of interest. The 3D interconnected porous structure with gel like mechanical properties make them highly suitable for tissue engineering [164, 184, 193, 205, 226], such as poly(3-thiopheneacetic acid) hydrogel [227].

CPHs for energy storage applications are commonly in the form of composites with graphene or carbon nanotubes [224, 228, 229], which may lead to phase separation with two different materials. Ghosh *et al*. have demonstrated a PPy/PEDOT hydrogel as a supercapacitor electrode [230], however, they used the pre-formed PEDOT film (about 2/3 of the contained water was evaporated) for ionic cross-linking to form the hydrogel, since PEDOT dispersion can easily disintegrate upon the direct contact with high concentration Mg^{2+} solution and difficult to form a bulk hydrogel [231] . There are significant limitations in controlling the structure due to the additional processes introduced, including film forming, drying and re-swelling. PANi hydrogels [232, 233] or PPy hydrogels [234-236] prepared by chemical polymerization have demonstrated

a high conductivity for application in energy storage, but they require a long purification time to remove excess reactants or by-products. Furthermore, little information is available on the mechanical properties of these CPHs, nor their application in tissue engineering.

In this chapter, a cytocompatible PPy/PEDOT hydrogel was developed as a cathode for a Mg battery. PPy is electrochemically deposited onto the PEDOT hydrogel that is obtained by a two-step cross-linking process. This hydrogel is suitable for electrode-cellular application. It demonstrates a high battery performance when coupled with a bioresorbable Mg alloy in phosphate-buffered saline. A combination of suitable mechanical and electrochemical properties makes this hydrogel a promising material for bionic applications.

3.2 Experiment Section

3.2.1 PPy/PEDOT hydrogel Fabrication

A 1.5 wt% PEDOT:PSS dispersion (3 ml) was mixed with 0.25 M $Mg(NO_3)_2$ (360 µL). This partial ionic crosslinking process lasted 24 h in a cuboid conductive template, followed by an immersion in 1 M $Mg(NO_3)_2$ overnight for additional crosslinking. Then it was immersed in 0.1 M freshly distilled pyrrole and 0.1 M *p*TS solution for 2 h at 4 ºC prior to commencing the electropolymerization at 0.7 V vs Ag/AgCl. The consumed amount charge is 1C.

A similar procedure was followed to fabricate PPy/PEDOT hydrogel on stainless steel mesh for electrochemical tests and cell work. The uniformly mixed 1.5% PEDOT:PSS and 0.25 M $Mg(NO_3)_2$ solution (60 µL) was cast onto a UV-ozone-treated stainless steel mesh (1 x 1 cm^2). The samples were kept in the hood for 20 min for gelation before being immersed in 1 M Mg $(NO_3)_2$ for 2 h. The applied charge for PPy

electropolymerization (0.7 V vs Ag/AgCl) was 1 C per cm^2. PPyon stainless steel mesh was also prepared as control.

3.2.2 Cell work

PPy/PEDOT hydrogels were treated by soaking in sterile PBS supplemented with 500 U/ml Penicillin-Streptomycin for 20 h. The hydrogels were placed into six-well polystyrene cell culture plates and soaked overnight with culture medium, followed by rinsing with PBS twice. Adipose-derived stem cells (hADSCs) were seeded on the samples at the density of 3×10^4 cells/cm^2, and cultured in DMEM media supplemented with 10% FBS for 72 h. Then cells were visualized using Live/Dead (calcein-AM/PI) staining following the methods in 2.3.1. For SEM imaging, the hADSCs were fixed in 3.7% paraformaldehyde for 1 h at room temperature, followed by a freezing process in liquid nitrogen and a freeze drying process.

For the proliferation study, cells were seeded at 10^4 cells/cm^2 in a 24-well plate. Cell viability and proliferation ability were measured by PrestoBlue (Life technology) following the methods in 2.3.2. Specifically, at day 1, 3, 7, 14 and 21, cells were incubated in 10% Prestoblue (in culture media) for 1h.

Electrical stimulation was studied to demonstrate that PPy/PEDOT hydrogel may be beneficial as tissue engineering scaffold. Each PPy/PEDOT hydrogel was seeded initially at the density of 10^4 cells/cm^2 in a custom designed acrylic chamber filling with culture media.

3.2.3 Characterization

Surface morphology or cross-sectional view of PPy, freeze-dried PEDOT or PPy/PEDOT hydrogels was investigated by field emission scanning electron microscopy. The method for thermal properties, compressive stress-strain curves and

rheological tests are detailed in 2.3.

Cyclic voltammetry tests were performed within a potential range of -0.7 V to 0.6 V at various scan rates. Impedance spectra were measured over the frequency range of 100 kHz to 0.01 Hz with an AC perturbation of 10 mV at open-circuit potential. Batteries were assembled using a PPy-PEDOT hydrogel or a PPy cathode (1×1 cm^2) coupled with a Mg alloy anode (1×1 cm^2) in a one-component cell containing 10 mL PBS. The discharge test was carried out using a battery-testing device (Neware Electronic Co.).

3.3 Results and discussion

3.3.1 Formation mechanism and porous structure of PPy/PEDOT hydrogel

In the PEDOT:PSS compound, PSS is in excess with respect to the positively charged PEDOT chain [237]. Excessive negative charge of the PEDOT:PSS complex can be ionically crosslinked in solution by multivalent cations. The cation of Mg^{2+} can electrostatically interact with PSS as an ionic crosslinker (Figure 3.1A). The addition of low concentration $Mg(NO_3)_2$ was used to convert the viscous PEDOT:PSS dispersion (Figure 3.1B) into a monolithic gel, capable of maintaining its structure under gravity (Figure 3.1C).

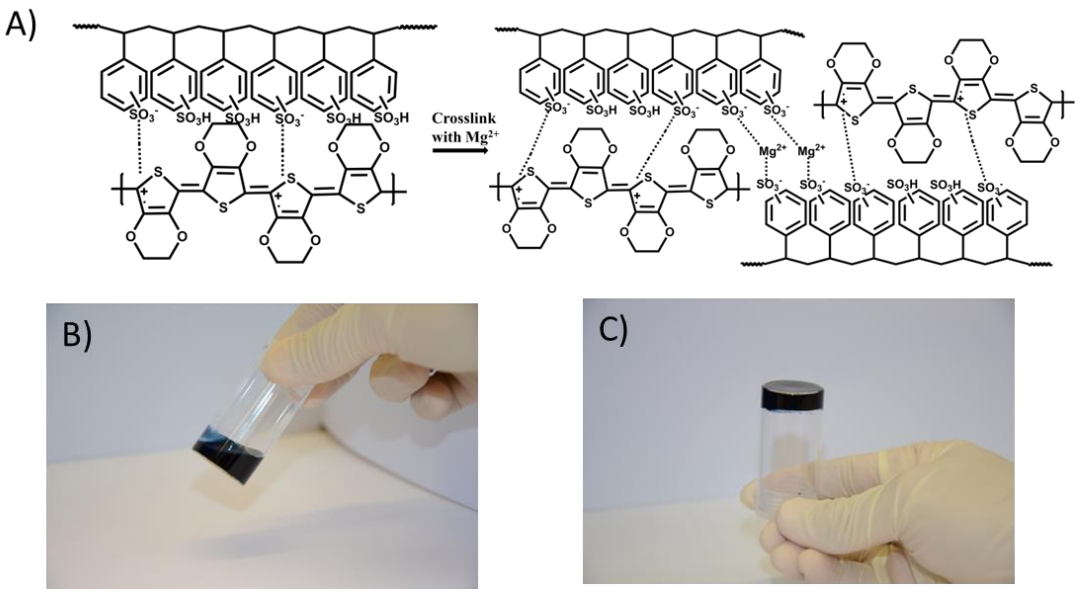

Figure 3.1 (A) Crosslinking process of PEDOT:PSS hydrogel. Digital images of freshly mixed 1.5% PEDOT and 0.25 M $Mg(NO_3)_2$ solution (B) and after the gelation (C).

Similarly, the PEDOT film that was partially crosslinked with Mg^{2+} can maintain its integrity when contacting with 1 M Mg^{2+} solution, in contrast to the disintegration of pure PEDOT film (Figure 3.2). It has been reported that aqueous PEDOT:PSS films are easily disintegrated in excess Mg^{2+} solutions rather than gelation occurring [230, 231]. The initial crosslinking step allows Mg^{2+} to evenly distribute throughout the PEDOT:PSS dispersion and slightly crosslink it. This process is essential to maintain a uniform hydrogel avoiding local gelation when contact with high concentration Mg^{2+} solution. The use of a higher concentration of Mg^{2+} in the second step is to increase the degree of crosslinking and thus improve the overall strength of the hydrogel.

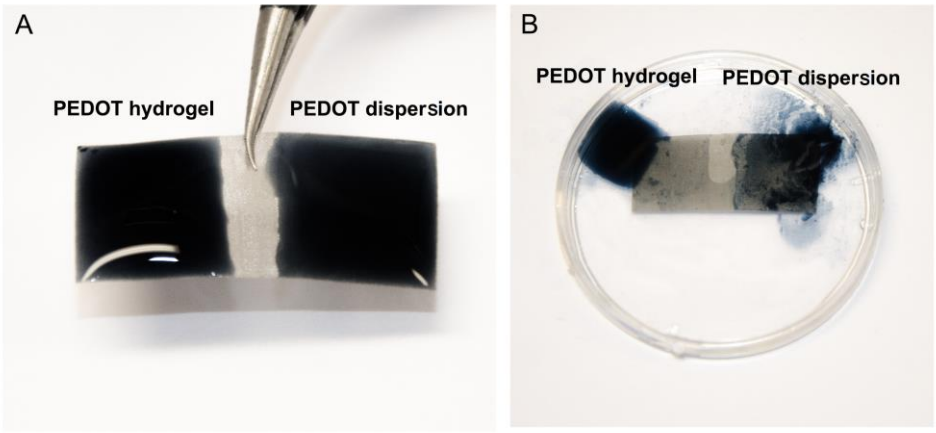

Figure 3.2 A) Photos of the freshly fabricated PEDOT film partially crosslinked with Mg^{2+} (left) and pure PEDOT film (right) on one piece of stainless steel mesh; B) Photos of these two fresh PEDOT films after they were immersed in 1M $Mg(NO_3)_2$. Partially cross-linked PEDOT film maintained its integrity while pure PEDOT film was disintegrated.

After the formation of PEDOT hydrogel, an additional electropolymerization process of PPy is applied on PEDOT hydrogel to fabricate PPy/PEDOT hydrogel with the increase in the mechanical properties of the composite (Figure 3.3A). The PEDOT hydrogel changed colour from dark blue (Figure 3.3B, left) to black (Figure 3.3B, right) after the incorporation with PPy. The PPy/PEDOT hydrogel materials were mechanically robust, and still retained the shape without any volume loss after removing the mould. This free-standing hydrogel was robust and can be lifted by a pair of tweezers (shown as the insert picture of Figure 3.4B). In contrast, PEDOT hydrogels were collapsed under their own weight (left hydrogel in Figure 3.4B). It should point out that a facile and easily to scale up method (e.g., chemical/electrochemical synthesis) have been applied in the formation of PPy/PEDOT hydrogel. Hence it is possible to fabricate a PPy/PEDOT hydrogel with any desired shape or size using this method.

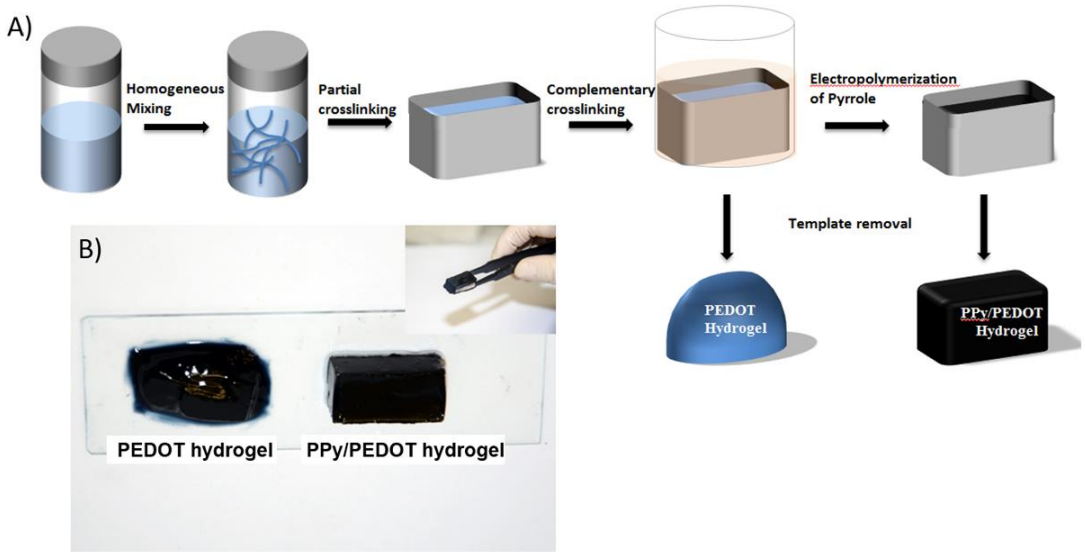

Figure 3.3 A) Schematic procedures to fabricate PEDOT hydrogel and PPy/PEDOT hydrogel. B) Digital images of PEDOT hydrogel (left) and PPy/PEDOT hydrogel (right) after the template removal; Inset shows that robust PPy/PEDOT hydrogel can be lifted by a tweezer.

The growth curve of PPy on PEDOT hydrogel is shown in Figure 3.4, and growth of PPy on stainless steel is the contrast. Both of the growth curves of PPy on stainless steel and PEDOT hydrogel show similar characteristics: a plateau where the diffusion controlled monomer oxidation and a rapid increase of charge density indicating continuous and gradual polymer growth [238]. A higher deposition current was produced during the PPy growth on PEDOT hydrogel, compared with that with stainless steel substrate at the same applied potential (Figure 3.4). It can be ascribed to the increased surface area ascribed to the hydrogel's 3D porous structure as well as its good compatibility with the electrolyte.

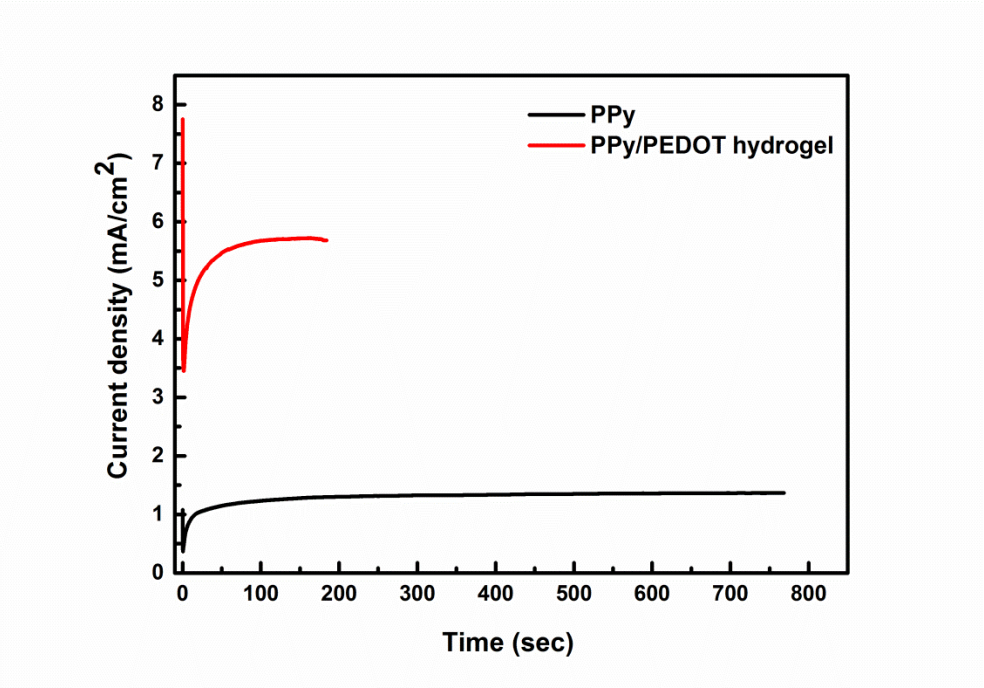

Figure 3.4 Chronoamperometric curves recorded during the PPy growth on a stainless steel mesh (black line) or a PEDOT hydrogel (red line) at 0.7 V (vs.Ag/AgCl) in 0.1 M pyrrole and 0.1 M *p*Ts electrolyte. A charge of 1C cm^{-2} was consumed.

The water contents of PEDOT and PPy/PEDOT hydrogels were estimated by thermogravimetric analysis. PEDOT and PPy/PEDOT hydrogels displayed a sharp mass loss between 50°C and 100°C in the TGA measurement (Figure 3.5), which is associated with water contained in the structure. The water content was estimated to be 97.5% for PPy/PEDOT hydrogel, and 98.2% for PEDOT hydrogel by the enlarged inset of Figure 3.5.

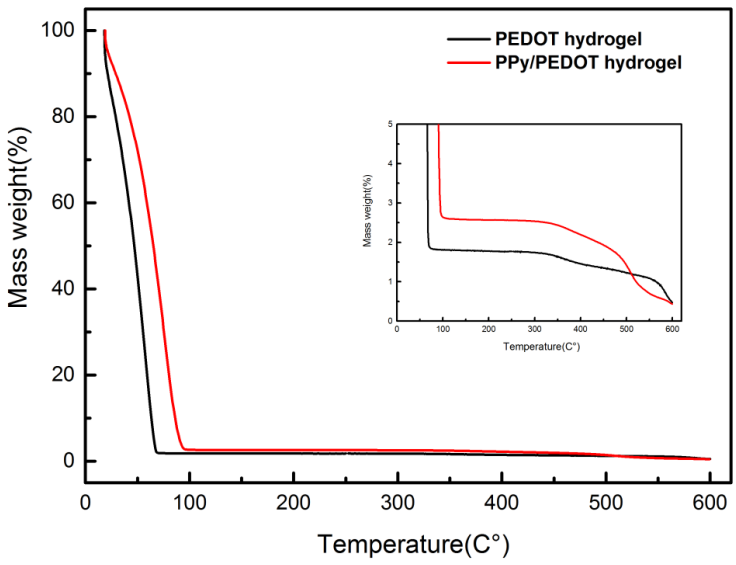

Figure 3.5 TGA of PPy/PEDOT hydrogel and PEDOT hydrogel. Inset image is the enlarged figure of Mass weight (0-5%) vs. temperature.

3.3.2 Physicochemical properties of PEDOT hydrogel and PPy/PEDOT hydrogel

3.3.2.1 Mechanical properties of PEDOT hydrogel and PPy/PEDOT hydrogel

The PEDOT gel displayed the properties resembling a highly concentrated polymer solution with a plateau region of storage modulus G' around 2.5-3.2 kPa (Figure 3.6A), a compression fracture strength of 1.6 kPa and a Young's modulus of 0.9 kPa (Figure 3.6B). In contrast, the PPy/PEDOT hydrogel exhibited a robust gel-like behaviour with G' remaining almost constant around 13.5-19.3 kPa, higher than that (~3 kPa) of poly(N-isopropylacrylamide)/PPy hydrogel [236]. PPy/PEDOT hydrogel also exhibited a much higher compression fracture strength and a Young's modulus respectively 12.4 kPa and 7 kPa. Such enhancement is attributed to the incorporation of the stiffer PPy network into the PEDOT hydrogel matrix providing additional reinforcement and mechanical support.

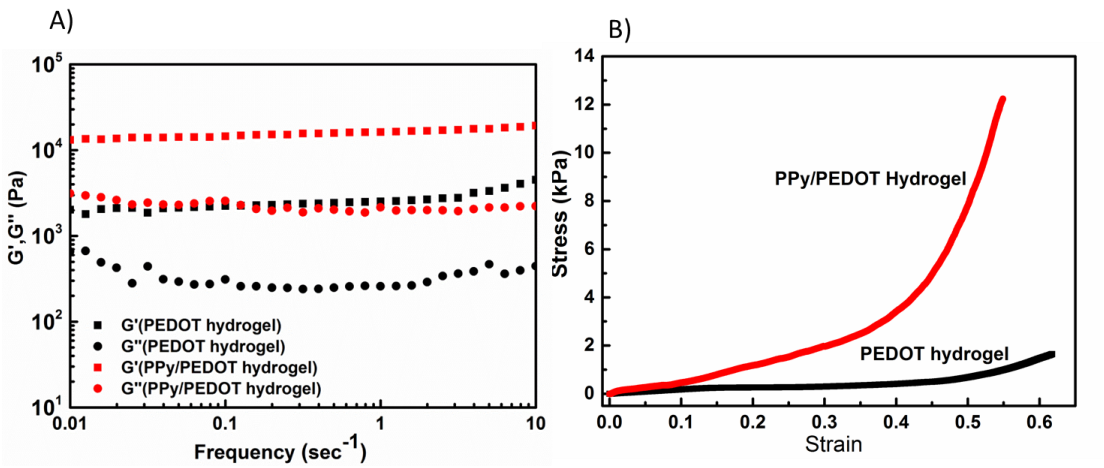

Figure 3.6 A) Rheological behaviours of PPy/PEDOT hydrogel and PEDOT hydrogel. B) Compressive stress-strain curves of PPy/PEDOT hydrogel and PEDOT hydrogel.

The modulus can be further improved to ~12 kPa and ~32 kPa when the charge consumed during the PPy growth was increased by 150% and 200% (Figure 3.7). It is because of the different amounts of PPy chains attached on the PEDOT hydrogel scaffolds to increase their mechanical properties. This modulus range (7~32 kPa) matches that of adipose (2 kPa), neurons (1-10 kPa), and skeletal muscle (~30 kPa) tissue [239-241], thus making these PPy/PEDOT hydrogels candidates for tissue regeneration.

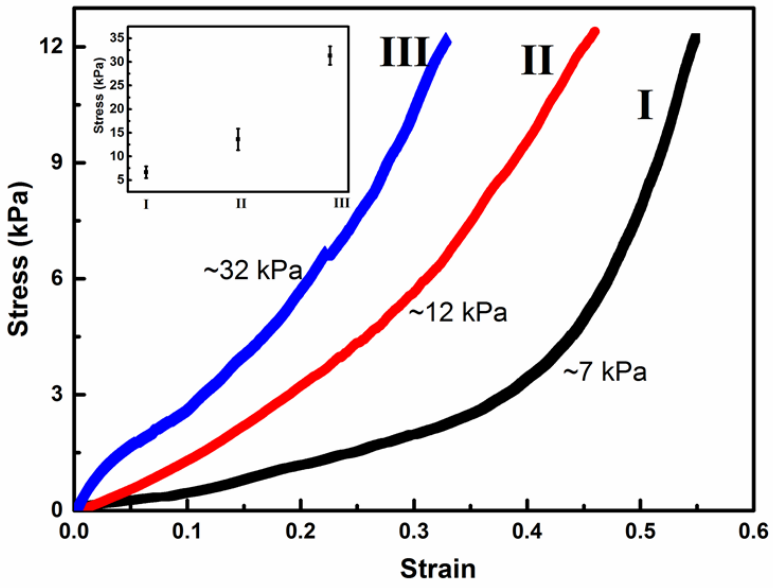

Figure 3.7 Stress-strain curves of PPy/PEDOT hydrogels with different deposition amount of PPy (charge consumed during PPy growth per ml PEDOT hydrogel: 16.7C (I), 25C (II) and 33.4C (III) (Inset, Young's modulus with deviations).

3.3.2.2 Microscopic structures of PEDOT hydrogel and PPy/PEDOT hydrogel

Freeze-drying is a pore-protecting drying method, and is widely used to process hydrogels to characterise the porous structure [242]. Both PEDOT (Figure 3.8A) and PPy/PEDOT hydrogel (Figure 3.8B) displayed a typical 3D interconnected porous structure. PPy/PEDOT hydrogel matrix is composed of more denser or smaller micropores compared with that of PEDOT hydrogel, implying a higher mechanical robustness. PPy on the stainless steel mesh showed a granular surface morphology (Figure 3.8C, 3.8F), compared with that of PEDOT (Figure 3.8A, 3.8D). This coarse surface was composed of granules at higher magnification, clearly demonstrating the existence of PPy. Both PEDOT and PPy/PEDOT hydrogels demonstrated a similar cross-sectional view being a typical hydrogel structure (Figure 3.8G and H).

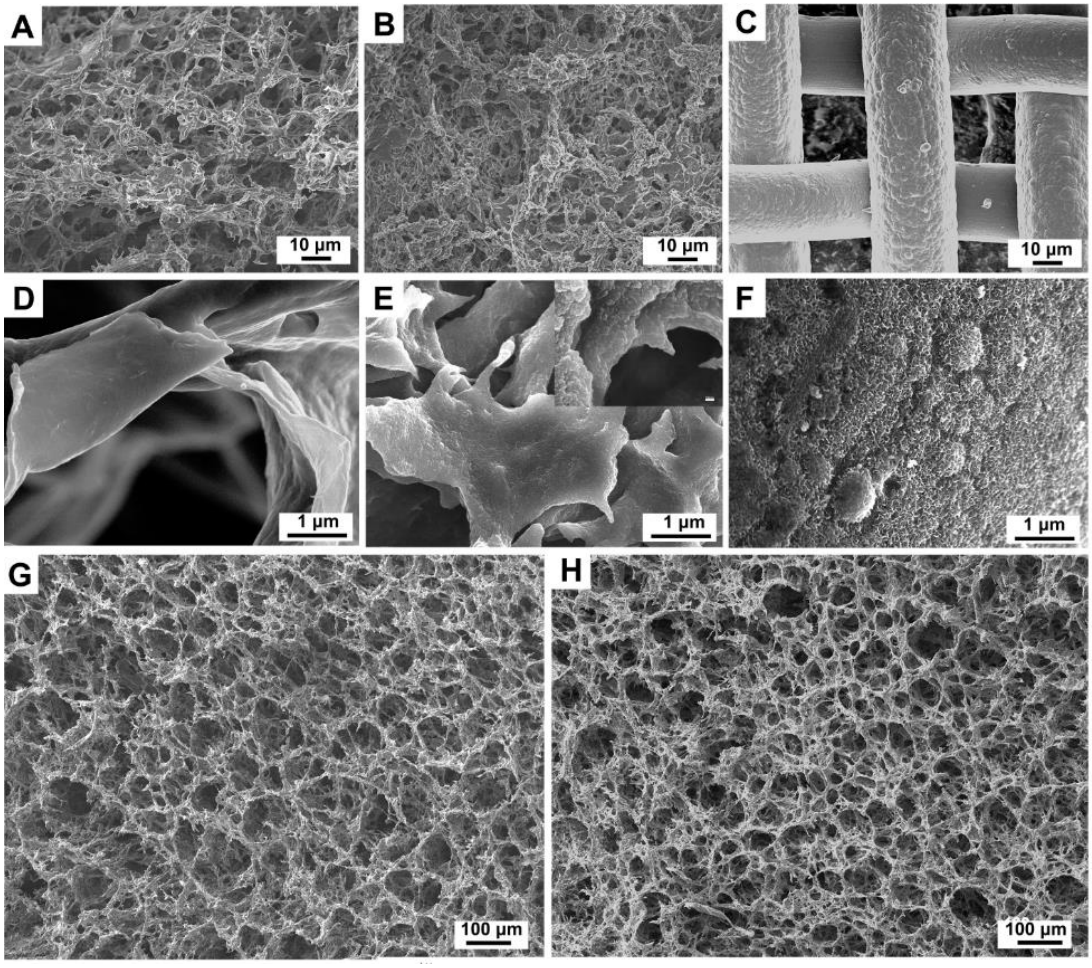

Figure 3.8 Surface morphology of PEDOT hydrogel (A, D), PPy/PEDOT hydrogel (B, E), and PPy on a stainless steel mesh (C, F) (Inset E, scale bar 100 nm); Cross-sectional images of PEDOT hydrogel (G) and PPy/PEDOT hydrogel (H).

The elements contained in these hydrogels were examined using energy-dispersive X-ray spectroscopy (EDS) associated with SEM (Figure 3.9). Elements, C, S and O, were detected in all these three samples. Mg was observed in the PEDOT and PPy/PEDOT hydrogel, which is from the crosslinking agent used, $Mg(NO_3)_2$. The element N is from the pyrrole ring. The presence of N in the PPy/PEDOT hydrogel proves the successful deposition of PPy onto PEDOT hydrogel.

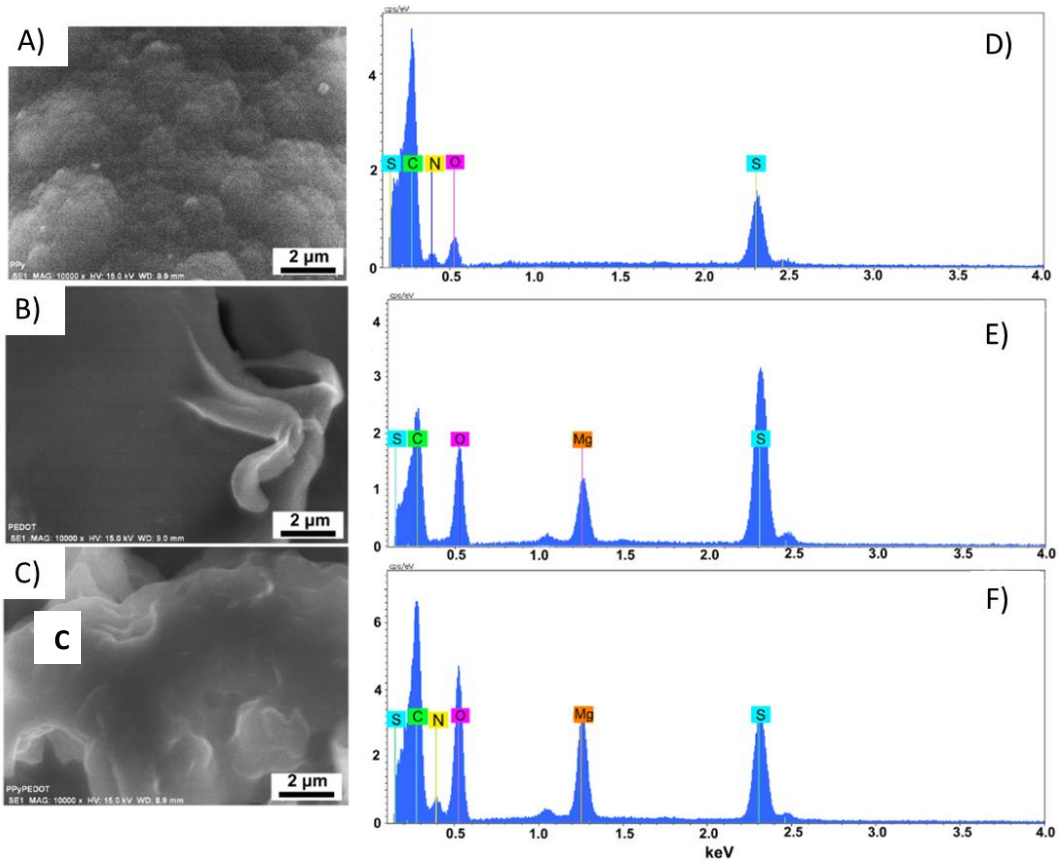

Figure 3.9 SEM images and the corresponding EDX spectra of PPy (A, D), PEDOT Hydrogel (B, E) and PPy/PEDOT Hydrogel (C, F).

3.3.3 PPy/PEDOT hydrogel as the cathode for Mg-air battery

3.3.3.1 Electrochemical properties of PPy/PEDOT hydrogel

The PEDOT hydrogel alone displayed a negligible current response when scanned over the range of -0.7 V to 0.6 V at a scan rate of 20 mV/s (Figure 3.10), whereas with a PPy coating, both the anodic and cathodic current improved significantly. The negligible current response of PEDOT hydrogel was probably because PEDOT sued in this work didn't have the catalytic activity for ORR [226]. Cyclic voltammograms (CVs) obtained from the electrode with PPy alone had lower current densities for both oxidation and reduction compared with the PPy/PEDOT composite.

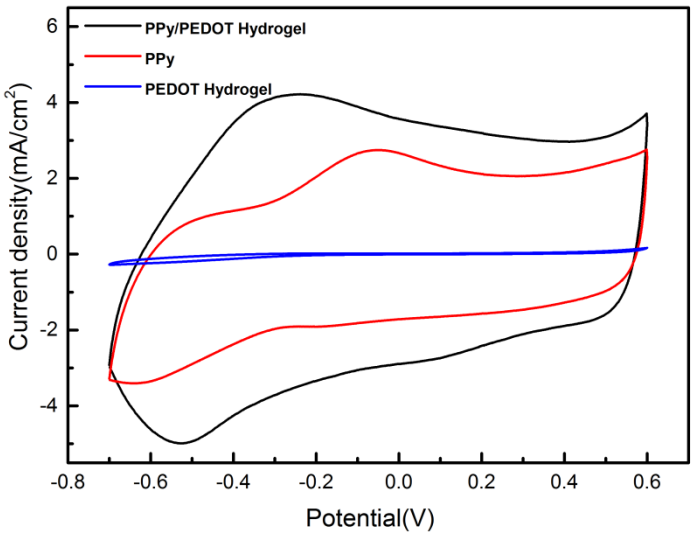

Figure 3.10 Cyclic voltammograms of PPy/PEDOT hydrogel, PPy or PEDOT hydrogel in PBS at a scan rate of 20 mV s^{-1}.

The negligible electrochemical response of PEDOT hydrogel compared to PPy/PEDOT hydrogel demonstrated that PPy was the major contributor to the high electroactivity. The significantly higher current response from PPy/PEDOT hydrogel compared to PPy on stainless steel can be attributed to its porous structure facilitating fast electron and ion transport [125]. Not surprisingly, the current response increased with the increased amount of PPy deposited (Figure 3.11A). It is also noted that the oxidation peak shifted positively and the reduction peak shifted negatively with increasing scan rate (Figure 3.11B), and this is attributed to the electrode resistance.

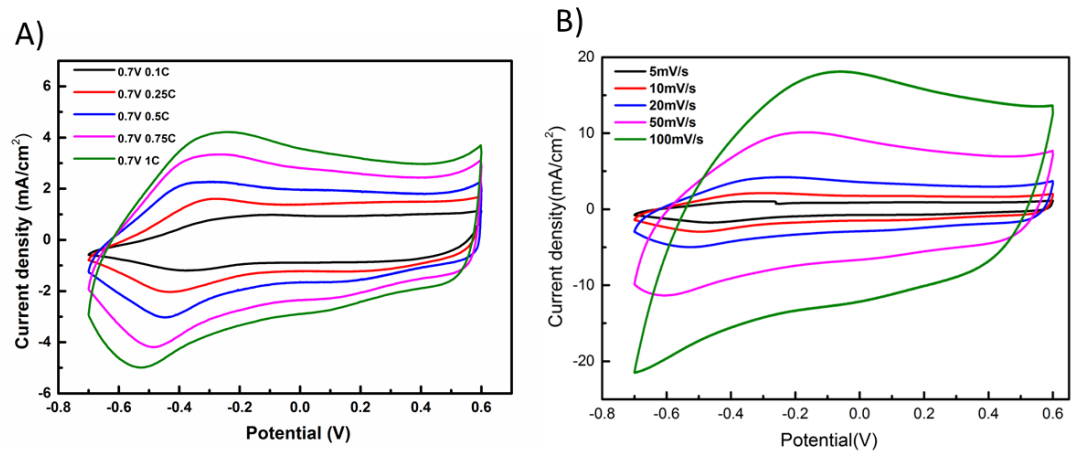

Figure 3.11 A) Cyclic voltammograms of PPy/PEDOT hydrogel with different deposition amount of PPy in PBS at a scan rate 20 mV s^{-1} (charge consumed during PPy growth per cm^2: 0.1, 0.25, 0.5, 0.75, 1C). B) Cyclic voltammograms of PPy/PEDOT hydrogel at different scan rates in PBS electrolyte.

The oxidization ability of PPy/PEDOT hydrogel was tested by the potential-time curve. The open circuit potential of the reduced PPy/PEDOT hydrogel (-0.8 V, 1800s) increased immediately after the bias potential was removed (Figure 3.12) in an O_2-rich or N_2-saturated PBS electrolyte. It was noticed that the potential at time = 0 (*e.g.* the biased potential was removed) was different, it was -0.45 V in O_2-rich electrolyte and -0.51 V in N_2-saturated electrolyte indicating different re-oxidation state of reduced PPy, which was directly related to the partial pressure of oxygen dissolved at the interface [243]. A potential of -0.04 V or -0.30 V were recorded at 400s, respectively. A higher potential increase in the O_2-rich electrolyte suggests that the reduced hydrogel can be readily re-oxidized by O_2.

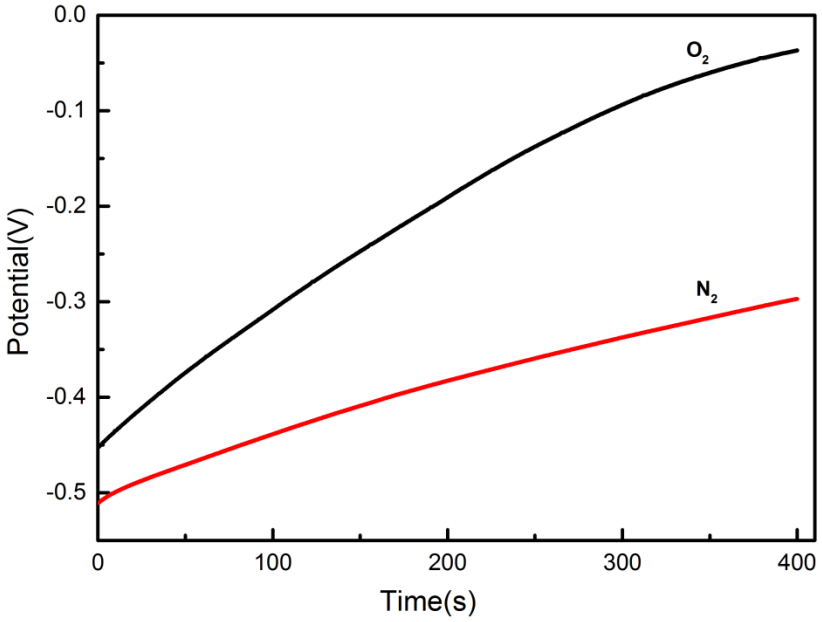

Figure 3.12 Potential response of PPy/PEDOT hydrogel electrode in O_2 or N_2 saturated PBS solution after the bias potential (−0.8 V vs Ag/AgCl) was removed.

The PPy/PEDOT hydrogel, PPy or PEDOT hydrogel displayed a bulk resistance of 15 Ω, 35 Ω and 10 Ω in PBS electrolyte, respectively (Figure 3.13). The lowest bulk resistance of the PEDOT hydrogel arises from its better electrical properties compared with PPy [158]. The PPy/PEDOT hydrogel displayed a smaller resistance in the medium-high frequency region compared to pure PPy, suggesting its fast electrochemical kinetics [244]. Neural cell communication commonly occurs between 300 Hz and 1 kHz [245]. PPy/PEDOT hydrogel showed its excellent ion transportation behaviour as evidenced by a low impedance of 10 Ω at 1 kHz, lower than 37 Ω for PPy (Figure 3.13, insert) and the previously reported KΩ level for the PEDOT hydrogel [246]. The low resistance is beneficial to recording high quality signals when used in vivo.

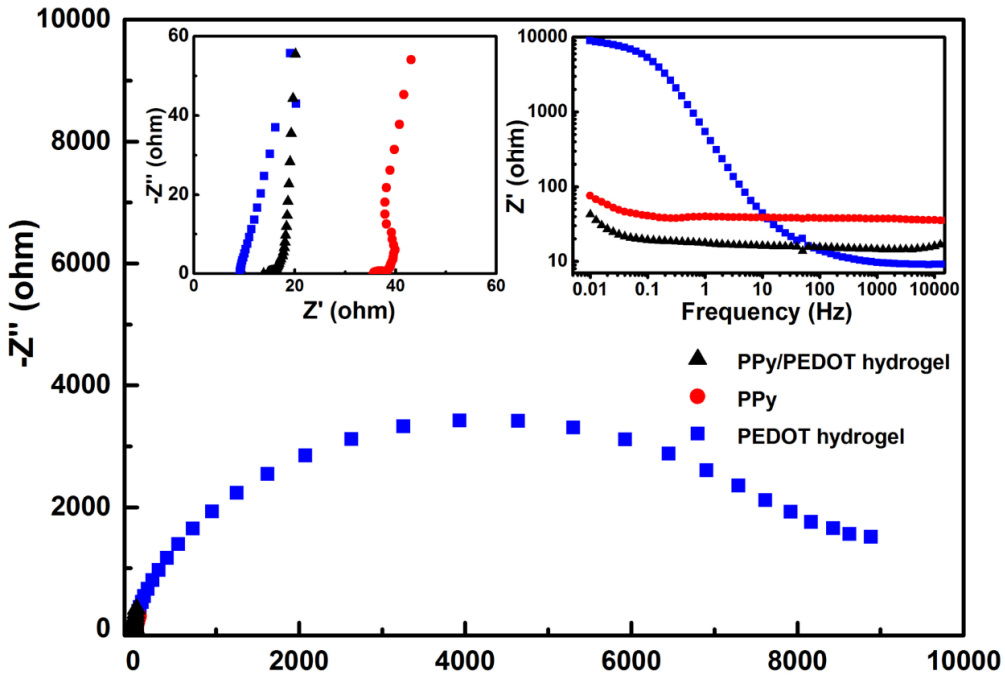

Figure 3.13 Nyquist plot of a PEDOT hydrogel, PPy or PPy/PEDOT hydrogel in PBS (Insets: left, expanded plot; right, plot of Z' vs. frequency).

3.3.3.2 Battery performance of Mg-air battery with PPy/PEDOT hydrogel or PPy as cathode

A Mg battery composed of PPy/PEDOT hydrogel or PPy was discharged for 6h at various discharge current densities (Figure 3.14). PPy/PEDOT hydrogel displayed a discharge plateau of 1.35, 1.20, 1.10, 0.93 and 0.45V, compared with 1.42, 1.26, 0.75, 0.55 and 0.27 V for PPy at a current density of 20, 50, 100, 200 and 500 μA/cm^2, respectively. It can be seen clearly that at a discharge current above 100 μA/cm^2, a PPy/PEDOT hydrogel battery displayed a higher discharge voltage indicating its better ORR catalytic ability at these discharge rates [247]. This may be explained by the fact that the porous conductive framework facilitates rapid electron transfer and shortens ion diffusion distances leading to better performance at high current densities.

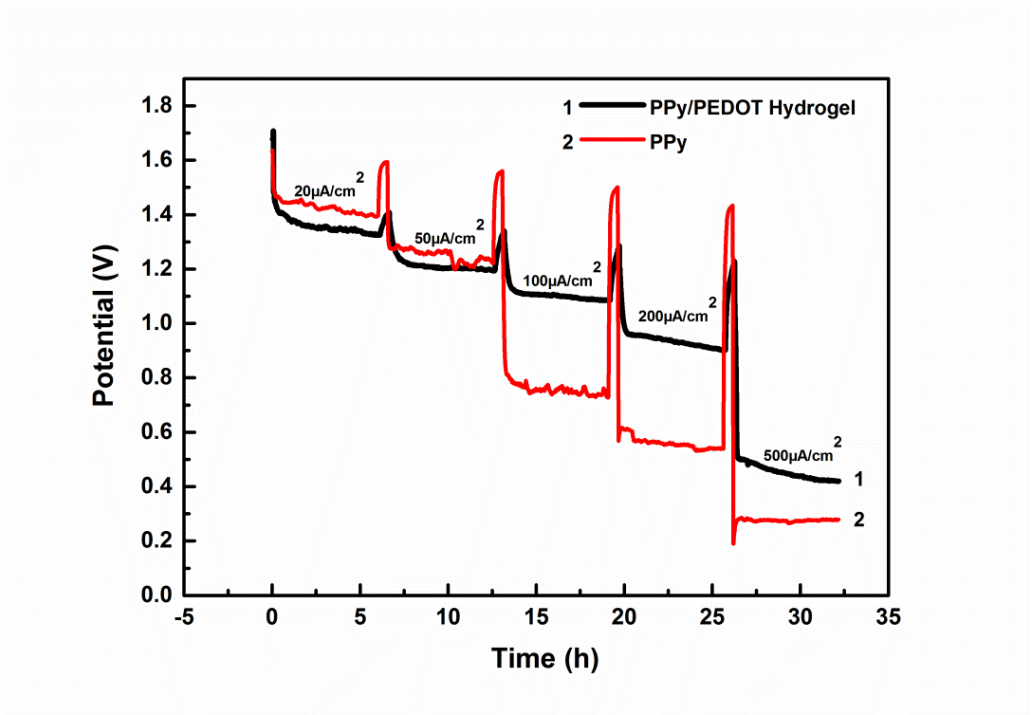

Figure 3.14 Discharge curves of a Mg battery with a PPy/PEDOT hydrogel or a PPy cathode in PBS at different discharge current densities (6h duration for each stage).

The Mg battery with a PPy/PEDOT cathode could provide a stable voltage of 0.7 V for about 160 h at a current density of 200 μA cm^{-2}, delivering a capacity of 32 mAh cm^{-2} and an energy density of 22 mWh cm^{-2} (Figure 3.15). This performance is superior to the 60 h for PPy with a capacity of 12 mAh cm^{-2} and energy density of 10 mWh cm^{-2}. The power to drive the implantable medical devices (IMDs) generally falls in the level of μW to mW [2], and therefore the Mg-air battery containing a PPy/PEDOT cathode is expected to power IMDs such as a pacemaker, cardiac defibrillator or a neurological stimulator with power requirement between μW to mW range.

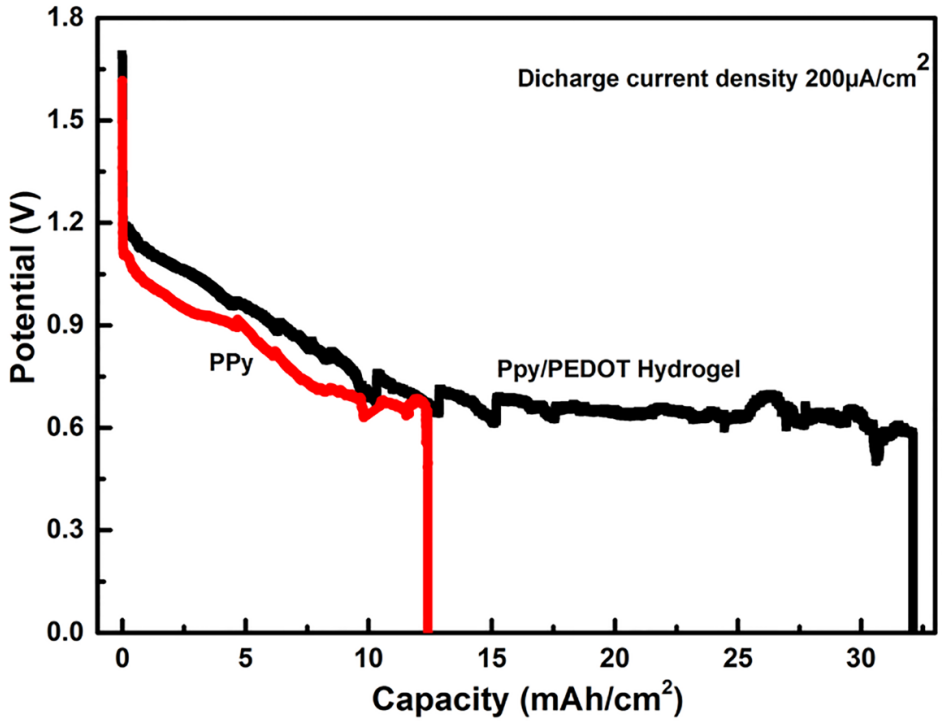

Figure 3.15 Discharge curves of a Mg battery with PPy/PEDOT hydrogel or PPy cathode at 200 μA cm^{-2} in PBS.

3.3.4 Bio-application of PPy/PEDOT hydrogel

3.3.4.1 Cytocompatibility of PPy/PEDOT hydrogel

Cytocompatibility is an important feature for the materials applied for *in vitro* or *in vivo* work. The cytocompatibility of PPy/PEDOT hydrogel was evaluated using adipose-derived stem cells (hADSCs). As shown in the live/dead fluorescence staining (Figure 3.16A), hADSCs were well spread and reached high confluence after seeding for 72 h, which indicates low cytotoxicity of the substrate. In agreement with the fluorescence image, the SEM images exhibited a flat, well spread cell morphology, with minor filopodia attached tightly to the PPy/PEDOT hydrogel. These cells were forming bridges over the highly porous substrate (Figure 3.16B, Figure 3.16C).

The total cell metabolic activity, characteristic of cell proliferation, increased significantly during the first 2 weeks, then stabilised (Figure 3.16D). These results demonstrate that this conductive PPy/PEDOT hydrogel provides a compatible substrate for hADSCs. Given its conductivity and electroactivity this organic conducting polymer based hydrogel could also serve as a conduit for electrostimulation to provide benefits of electrical stimulation [194, 248].

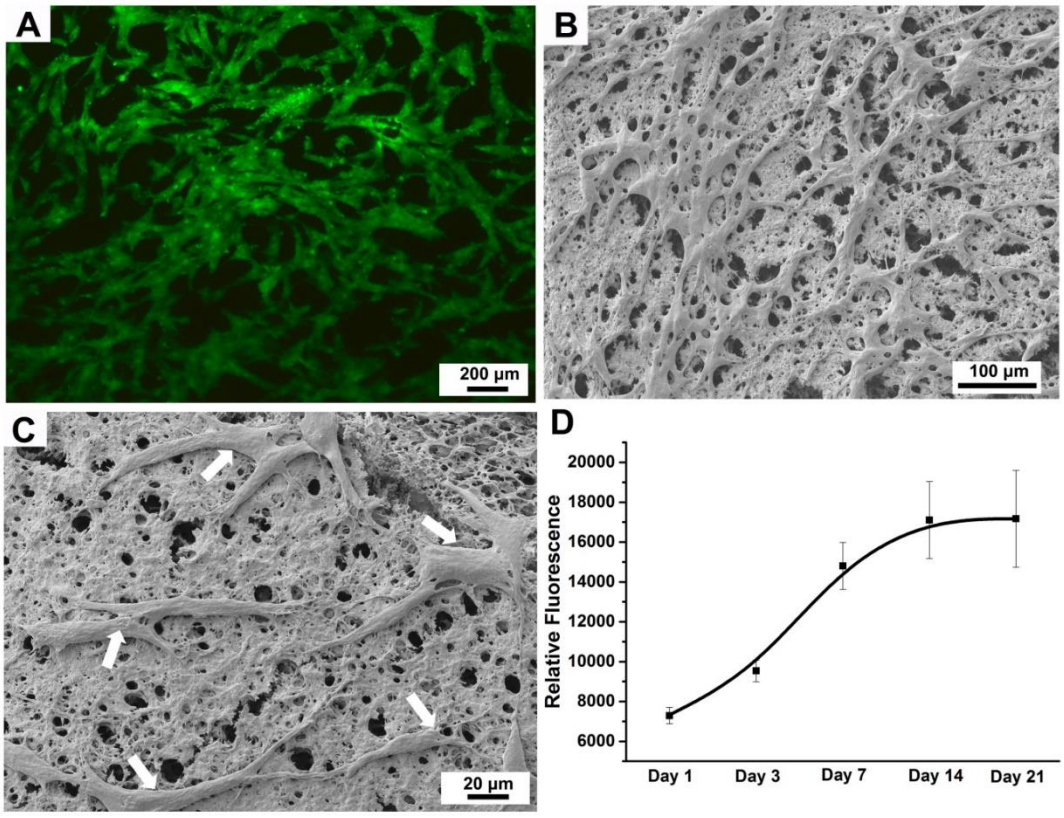

Figure 3.16 Live/Dead cell viability staining (green, live cells; red, dead cells) of hADSCs on the PPy/PEDOT hydrogel after 72h seeding. B, C) SEM images of cell on PPy/PEDOT hydrogels; D) Growth curve of hADSCs on PPy/PEDOT hydrogel at day 1, 3, 7, 14, 21.

Likewise, PC12 cells as the representative neural cell type were also cultured on the hydrogel samples and immune-stained for analysis to demonstrate that the hydrogel could be also applied in neuron research (Figure 3.17). As expected, cells number increased significantly in the first 3 days and reached the high confluence at day 10. However, it has also been noticed that there is an increased number of dead cells, which may be attributed to the too high cell density. The growth curve of PC12 cells (Figure 3.18) is consistent with the results shown in the fluorescence test. Cells number kept increasing with time, demonstrating that the PPy/PEDOT hydrogel can well support PC12 cells attachment and proliferation also.

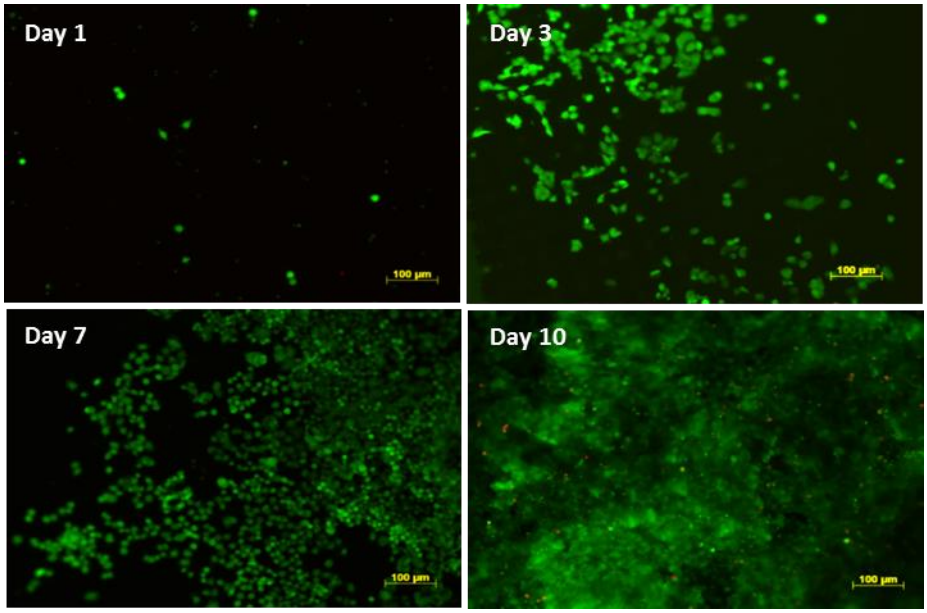

Figure 3.17 Fluorescence images of PC12 cells on the PPy/PEDOT hydrogel at A) day 1, B) day 3, C) day 7 and D) day10.

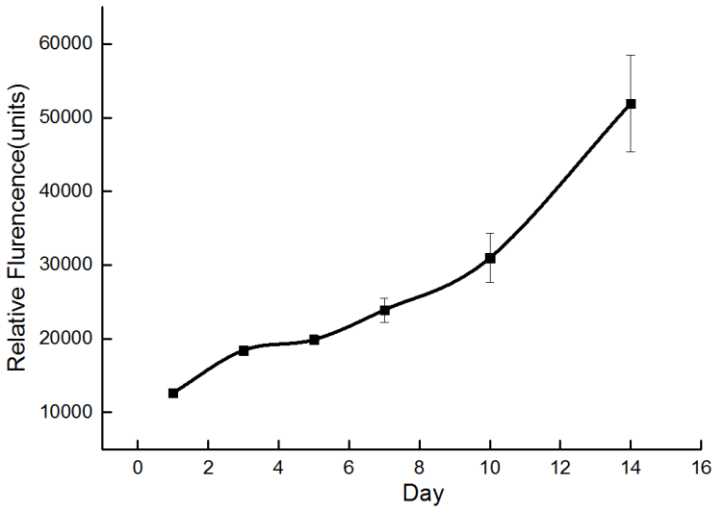

Figure 3.18 Growth curve of PC12 cells on PPy/PEDOT hydrogel at day 1, 3, 5, 7, 10 and 14.

3.3.4.2 Stem cell differentiation on PPy/PEDOT hydrogel

To evaluate whether stem cells can retain their differentiation potentialities, hADSCs were induced on PPy/PEDOT hydrogel in osteogenic differentiation media. As shown in SEM images (Figure 3.19 A-C), hADSCs displayed an irregular polygonal morphology of osteogenic induction, and had long cellular extensions on the PPy/PEDOT hydrogel samples. Filopodia were observed to be in direct contact with neighbouring cells as well as with hydrogel especially on the day 14 and day 21 when the cells achieved high confluence.

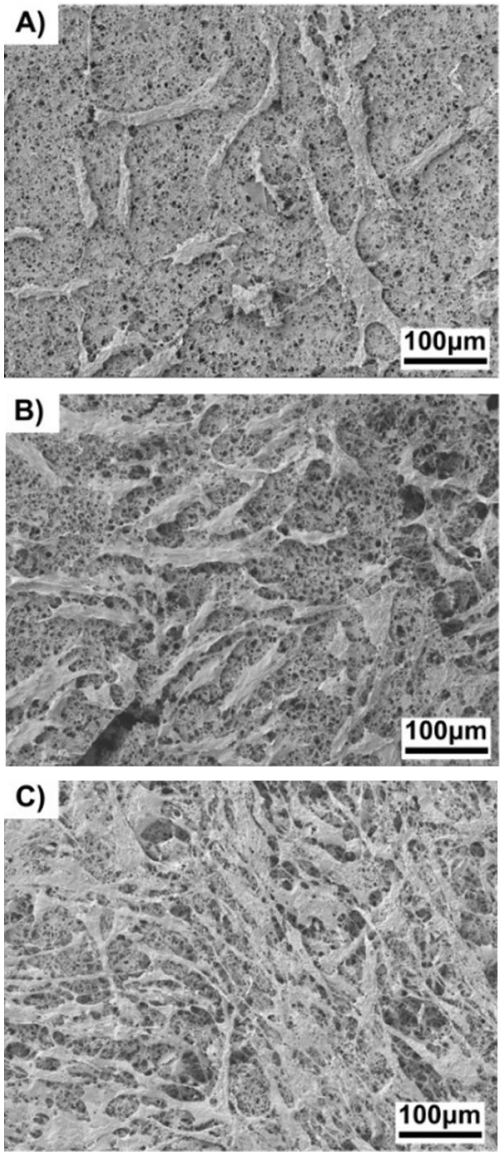

Figure 3.19 Cell attachment, differentiation and morphology on PPy/PEDOT hydrogel after 7 days, 14 days, and 21 days.

In addition, the mineralization process was semi-quantified by means of alizarin red staining. The results (Figure 3.20) demonstrated profound Ca deposition during osteogenic differentiation of hADSCs on PPy/PEDOT hydrogel. The calcium deposition amount increased with time. Since the ability of mineralization is a marker for mature osteoblast [249], these results clearly indicated that PPy/PEDOT hydrogel could support the osteogenic differentiation of hADSCs and lead to mineralization.

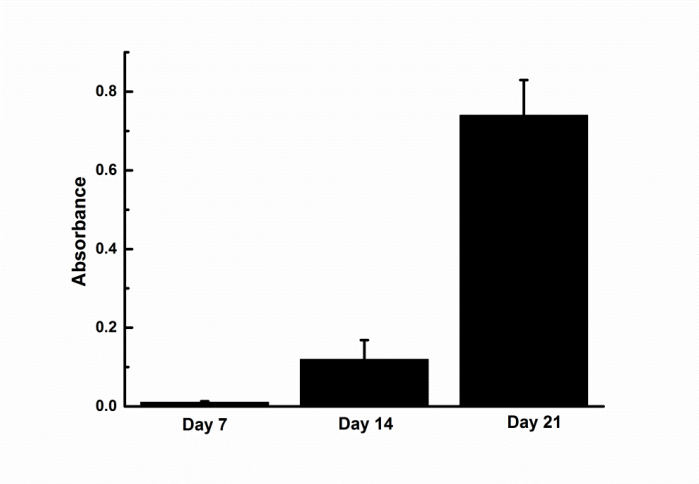

Figure 3.20 Semi-quantitative analysis of the mineralization by ADSCs on PPy/PEDOT hydrogel using alizarin red on day 7, 14 and 21.

Apart from hADSCs, PC12 cells could also successfully grow neurites on hydrogel, as demonstrated by the florescence images in Figure 3.21. Neurites started to extend at day 1, and formed a complex neuronal network at day 7. It shows that this hydrogel could support the differentiation of PC12 cells, potentially for the application of neural stimulation.

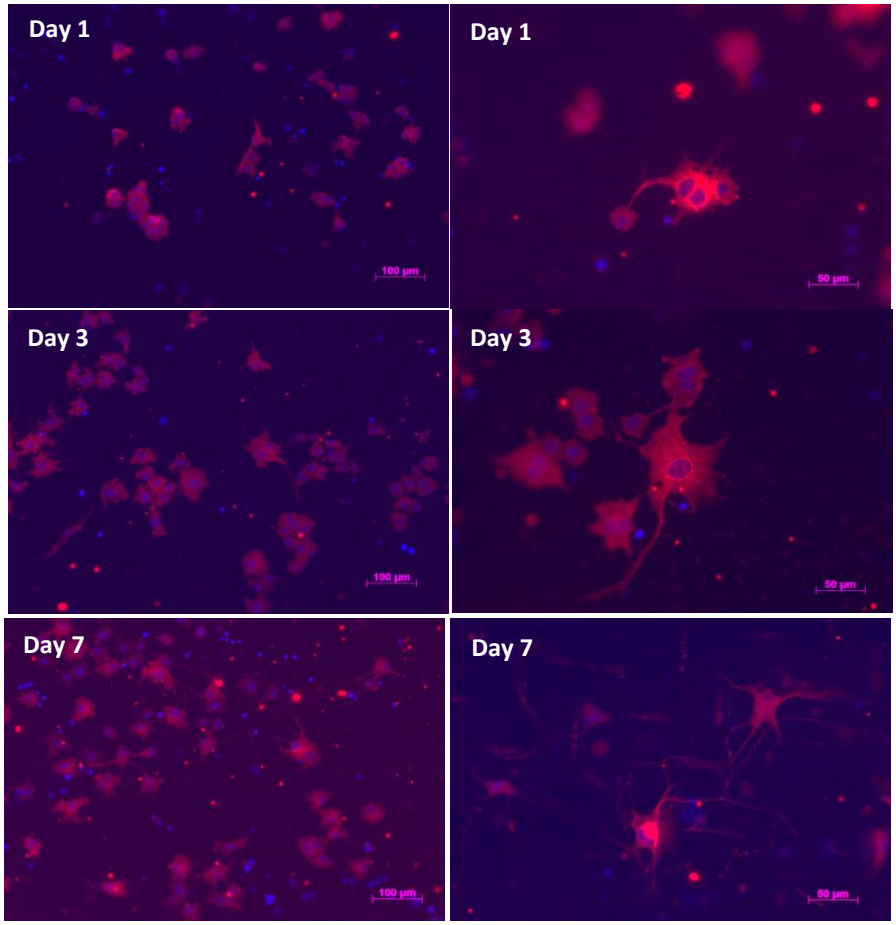

Figure 3.21 Immunostaining of PC12 cells cultured on the PPy/PEDOT hydrogel. PC12 cells were cultured in differentiation media for 7 days and stained with β-III tubulin.

3.3.4.3 Electric stimulation for differentiation of stem cells on PPy/PEDOT hydrogel

To assess whether the PPy/PEDOT hydrogel can deliver electrical stimulation to stem cells and promote differentiation, a custom designed chamber to stimulate hADSCs on this hydrogel was employed. The extent of hADSCs differentiation was initially evaluated by alkaline phosphatase (ALP) activity. ALP is an early indicator of immature osteoblast activity and commitment of stem cells towards the osteoblastic phenotype. ALP activity was almost increased twice in response to the electric

stimulation (Figure 3.22). In the meantime, the hADSCs morphology also underwent obvious changes, and more clonies and cuboidal osteogenic phenotype can be observed (Figure 3.23).

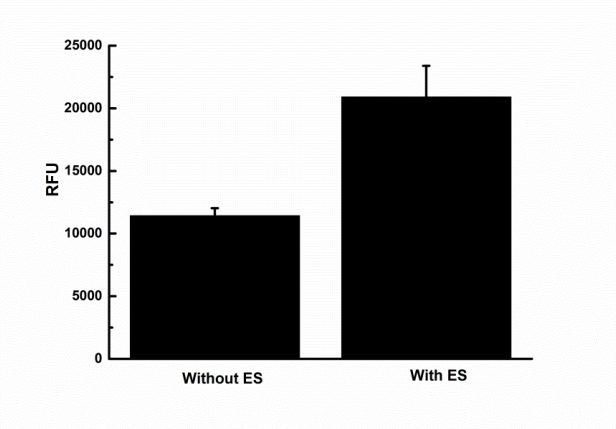

Figure 3.22 ALP activities of hADSCs without and with electrical stimulation (ES).

The ALP activity increased along with the morphological changes thus indicating that PPy/PEDOT hydrogel is a promising electrode material for osteogenic differentiation which can not only support stem cell adhesion, proliferation and differentiation, but also deliver electrical stimulation, and promote the differentiation process.

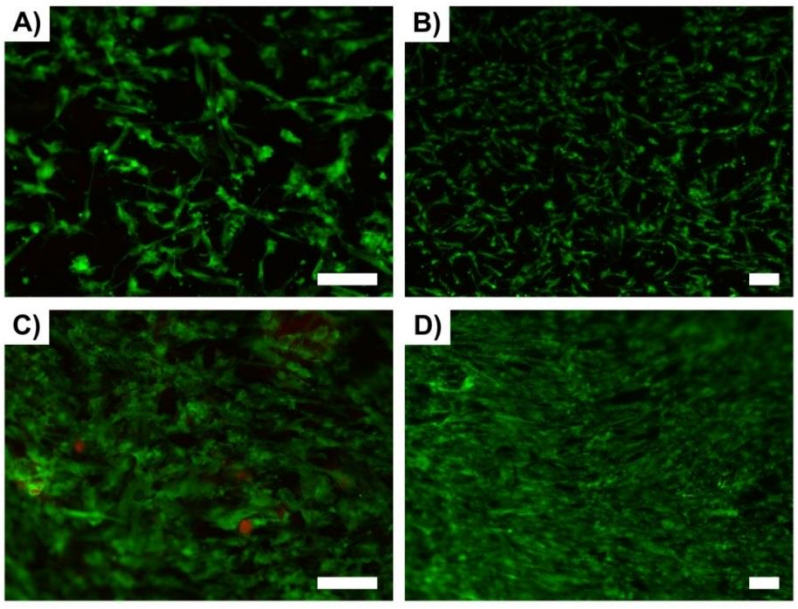

Figure 3.23 Live/Dead staining of hADSCs cultured on PPy/PEDOT hydrogel in osteogenic conditions without (A, B) and with (C, D) electrical stimulation for 7 days, scale bar 100 μm.

3.4 Conclusions

In summary, a robust hybrid conducting polymer hydrogel (PPy/PEDOT) has been developed for a Mg bioelectric battery. By introducing a two-step crosslinking method, it is feasible to fabricate the hydrogel in any desirable size and shape. The incorporation of PPy reinforces the hydrogel scaffold and can tune the mechanical properties suitable for use as different bio-interfaces. The battery assembled with this hybrid hydrogel possesses high capacity, high rate and high energy density due to its three-dimensional porous structure. This conductive hydrogel can also deliver electrical stimulation to the cultured stem cells on it and promote the differentiation. To meet the increasing demand of cytocompatible conductive materials with suitable mechanical properties for electrode-tissue interface, this work may open up new avenues to build three-dimensional conducting polymer hydrogel based electrodes that are capable of presenting spatial and temporal electrical stimulation for bionic applications. It can be anticipated that the energy generated from this type of bioelectric battery may be directly used to modulate cellular activities cultured on the hydrogel without need of an external power supply.

Chapter 4 A cytocompatible iron-air bioelectric battery for enhancing the degradation rate of Fe stent

4.1 Introduction

A bioelectric battery that utilizes aqueous electrolyte, a bioresorbable metal anode and a biocompatible cathode can offer high energy density. It is a promising power source for powering IMDs as the cathode active material (oxygen) is accessed from the physiological environment [250]. In Chapter 3, a Mg-air battery system has shown excellent battery performance. It is worth noting that the employed Mg or Mg based alloy anode has been widely researched for biodegradable metallic stents for vascular intervention and osteosynthesis as well [29, 251-253]. With the features of immunologically inert and matchable physical properties to the commonly used 316L stainless steel for stent, they can provide a temporary opening to a narrowed arterial vessel until the vessel remodels, and disappear progressively thereafter [254]. Unfortunately, the rapid corrosion of Mg stent in the chloride containing solution (e.g., human body fluid or blood plasma) is an intrinsic response as chloride ions promote rapid attack of magnesium; thereby the stents lose their mechanical integrity before the expected service life [255-257]. Moreover, the evolved hydrogen bubbles accompanying the rapid Mg corrosion accumulated in the gas pocket around the implant will delay the healing of surgery [31].

Compared with Mg, Fe has been considered to be an interesting candidate for a biodegradable implant material since their first safe implantation in rabbits for 1 year [258]. Fe is a physiologically essential component of cytochromes and oxygen-binding molecules; its content is high, about 35-45 mg per kilograms of adult body

weight [259]. It has well-defined transport systems for the clearance of its degradation products [260, 261]. With the aid of physiological metabolic processes, the organism succeeds in either excreting the products or integrating them into the natural metabolic process [262, 263]. However, Fe stents suffer from a slow degradation rate over an implantation period of 52 weeks that cannot match the tissue healing period, which significantly hampered its clinical utility [264, 265]. Efforts that have been made to improve the corrosion behaviour of Fe include alloying [266, 267], surface modification [268] and new manufacturing techniques to fabricate novel Fe stents (e.g. electroforming process) [269]. However, Fe corrosion is mainly ascribed to an oxidation-reduction process. These methods are all the static techniques that focus on modifying the Fe itself with passive corrosion.

In this chapter, we present a new dynamic approach to accelerate the degradation rate of Fe by coupling it with a cytocompatible PPy/PEDOT hydrogel cathode and a culture media electrolyte to form a galvanic Fe-air battery. The enhanced degradation behaviour of Fe as a cathode in a working battery (denoted as "with stimulation") compared to that non-activated/static battery (denoted as "without stimulation") *in vitro* was evidenced by the decreased corrosion impedance, increased anodic slope and positively shifted corrosion potential, as well as the increased Fe content released in the electrolyte. It can be explained that the oxygen reduction on the cathode will induce additional electrochemical reaction on Fe apart from the self-corrosion, thus resulting in enhanced corrosion. Impressively, the adipose-derived stem cells cultured on the battery's PPy/PEDOT hydrogel cathode can well attach and proliferate with stimulation for 21 days (2 hours/day) as well. This battery can also deliver a stable voltage potentially for biological activities such as cellular communications.

4.2 Experimental

4.2.1 Assembly of Fe-air battery

PPy/PEDOT hydrogels were prepared following the procedures as described in Chapter 3. They were treated by soaking in sterilised PBS supplemented with 500 U/ml Penicillin-Streptomycin for 20 h before the cells seeding. Fe foils were stored in nitrogen atmosphere before their use.

Batteries were assembled using a PPy/PEDOT hydrogel cathode (2 × 1 cm^2) coupled with a Fe alloy anode (2 × 1 cm^2) in a one-component cell containing 3 mL culture media electrolyte. Its schematic diagram is shown in Figure 4.1, and the assembly process is described in Chapter 2 (Section 2.4).

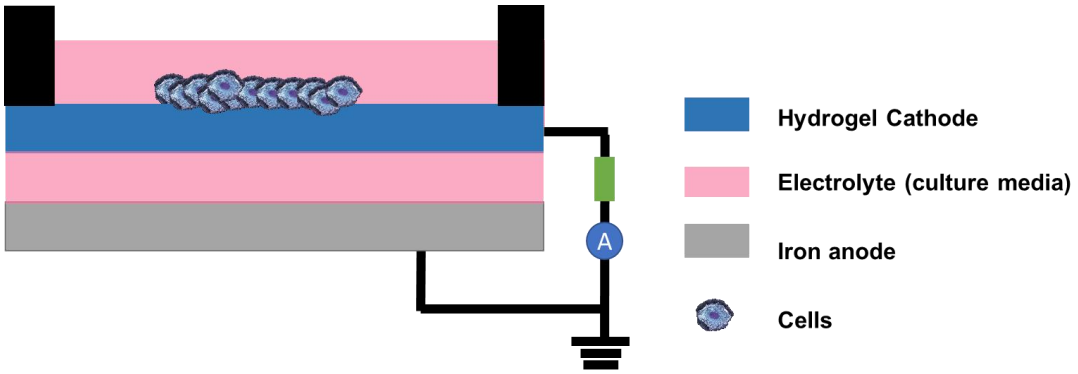

Figure 4.1 Schematic diagram of an Fe-air battery for in vitro work.

4.2.2 Degradation test

Degradation testing of Fe was performed in the above battery device with hADSCs culture media as electrolyte. The device was kept in an incubator (37 ºC, 5% CO_2) for the whole period of degradation testing. The battery was activated by connecting to a 120K resistor for 2 hours per day. The Fe foil anode in the static battery condition (e.g.,

open circuit potential state) was used as control. Three samples were tested for each time point. After the test, Fe foils were gently rinsed with water and dried. The composition and morphology of Fe anodes were then analysed with XRD, SEM techniques and electrochemical tests. The Fe content in the electrolyte from the battery systems were tested by AAS technique.

4.2.3 Metabolic activity of Adipose-derived stem cells

hADSCs were seeded on the PPy/PEDOT hydrogel cathode with a density of 2×10^4 cells/cm^2 and incubated in culture media 24 h for attachment. The culture media electrolyte was kept refreshed every day. The discharge of the battery was initiated by connecting to a 120K resistor. The cells were stimulated on PPy/PEDOT hydrogel by using the discharge current from this battery for 2 hours per day, lasting 21 days.

Cell viability and proliferation ability were measured by PrestoBlue. Specifically, at day 3, 7, 10, 14 and 21, all cells with and without the stimulation from an Fe-air battery discharge were incubated in 10% Prestoblue (in culture media) for 1h. Fluorescence was measured by a plate reader with a 544 nm excitation filter and a 590 nm emission filter.

4.2.4 Characterization

Surface morphology of the Fe foil was investigated by field emission scanning electron microscopy. Cyclic voltammetry tests were performed with an electrochemical workstation (CHI 650D). Impedance spectra were measured using a Gamry EIS 3000 system over the frequency range of 100 kHz to 0.01 Hz with an AC perturbation of 10 mV at open-circuit potential. Tafel curves were tested with the CHI 650D electrochemical workstation at a scan rate of 1 mV s^{-1} over a potential range of −1 to −0.1 V. Atomic absorption spectroscopy technique was performed to measure

the Fe ion concentration (diluted to 2% of the test solution in culture media with 0.1M HNO_3) in the electrolyte. X-ray diffraction patterns were recorded over the scan angles from 10° to 80° to identify the composition of Fe oxide on the Fe surface.

4.3 Results and Discussions

4.3.1 Performance of the Fe-air battery

As discussed above, this Fe-air battery is a water-activated primary battery that consists of a biodegradable Fe anode and an air-breathable conducting polymer hydrogel cathode. The performance of this battery was evaluated with the hADSCs culture media as an electrolyte at 37º (Figure 4.2). Based on the discharge curve, the Fe-air battery could provide a stable voltage of 0.61 V for about 60 h at a current density of 10 μA cm^{-2}, delivering a capacity of 1.3 mAh/cm^2 and a power density of 0.7 mWh cm^{-2}. The current gradually decreased after 60h which is not shown in the figure; which is due to the degradation of the Fe-air battery. It was noticed that there was some fluctuation during the battery discharging, as the iron-air battery was an open system that was affected by the oxygen content in the electrolyte. This calculated power falls within the range of μW to mW, which could potentially drive the implantable medical devices (IMDs) with low power requirement such as a stimulator [2].

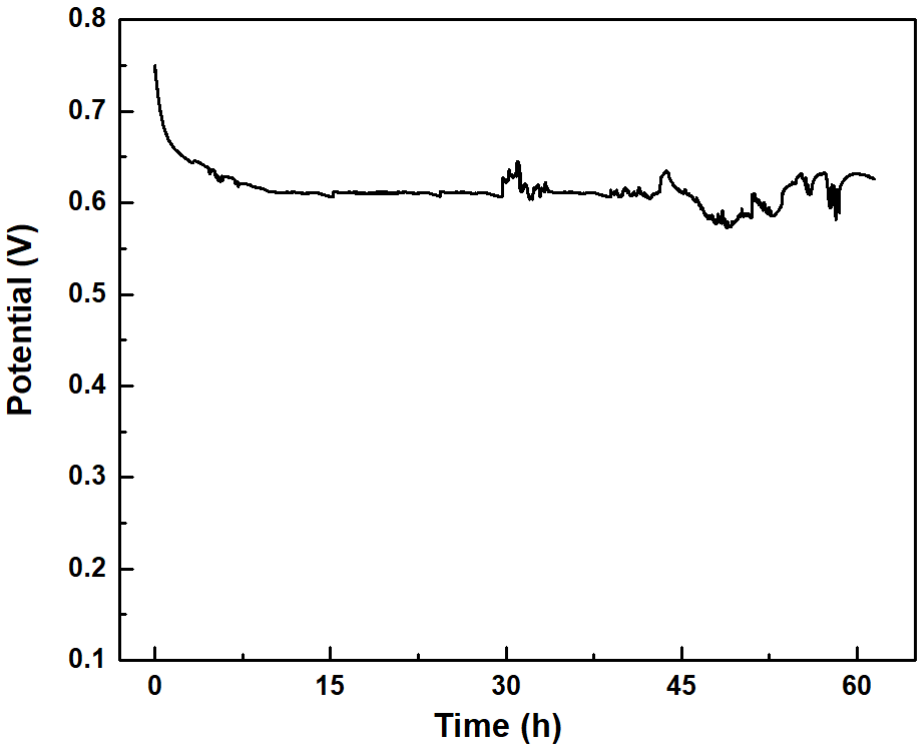

Figure 4.2 Discharge curves of an Fe-air battery with PPy/PEDOT hydrogel at a current density of 10 µA cm^{-2} in culture media of 37 ºC.

The overall cell reaction in this Fe-air battery that leads to energy generation is given in Equation (4.1) [270].

$$Fe + ½\ O_2 + H_2O \leftrightarrow Fe\ (OH)_2 \qquad 4.1$$

During discharge, Fe at the negative electrode is oxidized to Fe (II) hydroxide and oxygen is reduced at the positive electrode to form hydroxide ions. When oxygen is present, the reduction of oxygen is the predominant cathodic reaction as shown in Equation 4.2. The individual reactions at cathode and anode are given by Equations (4.2) and (4.3) [270]:

$$\text{Cathode: } ½\ O_2 + H_2O + 2e^- \rightarrow 2OH^- \qquad 4.2$$

$$\text{Anode: } Fe + 2OH^- \rightarrow Fe(OH)_2 + 2e^- \qquad 4.3$$

Ferrous hydroxide was initially formed on the Fe surface, but further discharging will build up the corrosion products Fe oxyhydroxide or haematite (Fe_2O_3) as shown in Equations (4.4) and (4.5) [271]:

$$Fe(OH)_2 + OH^- \rightarrow FeOOH + H_2O + e^- \quad 4.4$$

$$4Fe(OH)_2 + O_2 + H_2O \rightarrow 2Fe_2O_3 \cdot 5H_2O \quad 4.5$$

The voltage of this battery was recorded when discharging in the incubator, 2 hours per day for a 14 days period (Figure 4.3). The discharge potential was slightly decreasing from 0.68 V at day 3 to 0.65 V at day 14, providing a total capacity of 7.8×10^{-2} mAh cm^{-2} and an energy density of 50.7 µW cm^{-2}. This indicates that this battery with this energy density may be capable of powering some IMDs with low power requirements such as a stimulator [2].

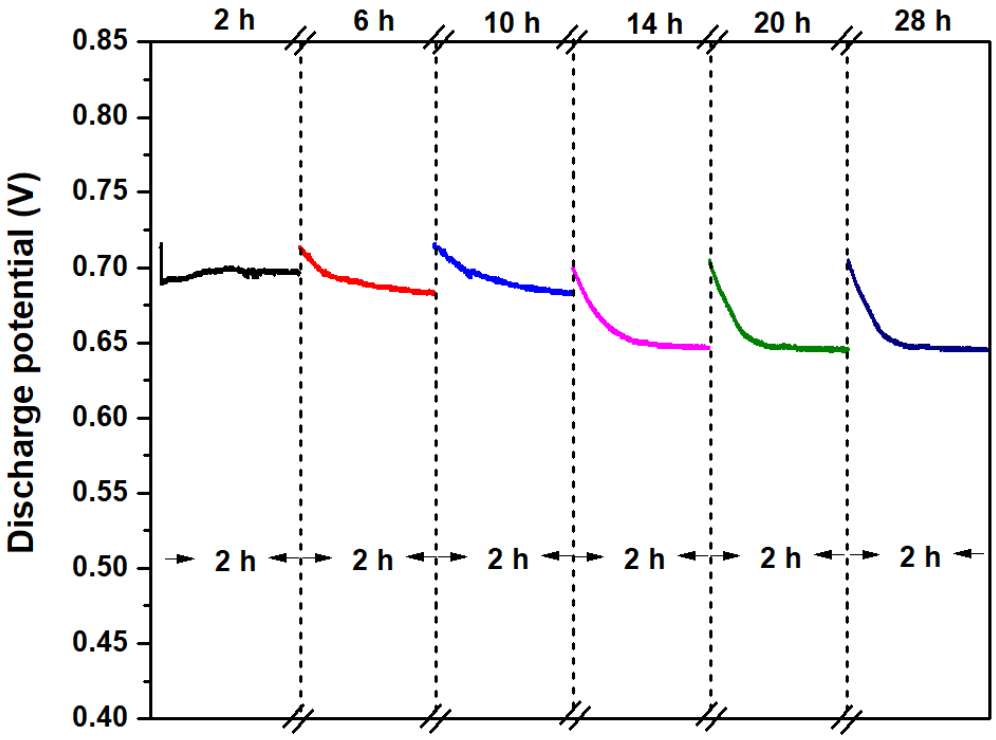

Figure 4.3 Discharge curve of Fe-air battery in the incubator at selected days 1, 3, 5, 7, day 10 and 14 (2 hours/ day).

4.3.2 Degradation of Fe anode with/without stimulation

Degradation of Fe started from its contact with culture media. Solid Fe has the capacity to readily donate electrons and is oxidized to Fe^{2+} (Equation 4.6). The produced ferrous ion may either dissolve into water, or deposit as scale on the corroding metal surface [272].

$$Fe^{0} \rightarrow Fe^{2+} + 2e^{-} \quad 4.6$$

Under the condition of pH 7.4 in an oxygen environment of physiological solution, some Fe^{2+} could be converting to the ferric form (Fe^{3+}) (Equation 4.7) [261]:

$$Fe^{2+} \rightarrow Fe^{3+} + e^{-} \quad 4.7$$

With the presence of oxygen, the resulting ferrous ions are oxidized and hydrolyzed forming various iron (hydr)oxide phases. With the presence of chloride ions, ferric hydroxide is further hydrolysed, and goethite (α-FeO(OH)) is formed as the first precipitate marking the oxidation state change of Fe^{2+} (ferrous) to Fe^{3+} (ferric) [273]. As the oxidation reaction further proceeds, the concentration of ferric chloride or ferric sulfate increases, β-FeO(OH) begins to be formed as the second precipitate [274].

In this work, after 3 days without stimulation (static condition) in the incubator (37 ºC, 5% CO_2), the Fe surface was partly covered by yellow products from Fe corrosion called the corroded floor, basic corrosion scales (Figure 4.4). While with the battery stimulation, a thicker yellow rust was distinctively formed at the centre of the Fe anode, which can be attributed to a more serious corrosion process with more corrosion

products accumulated. When composing a battery circuit, oxygen reduction on the cathode induced the oxidation of Fe being converted into Fe^{2+} products.

After immersion for a sufficiently long time, the galvanic effect was suppressed to some extent due to the limited oxygen reaching the Fe surface and the corrosion mechanism changed from general corrosion to pitting corrosion [275]. It is because oxygen depletion is the determining factor for the overall Fe corrosion reaction [276].

The pitting on Fe was due to the non-uniform corrosion with the dominant anodic reactions, which will be analysed in detail by electrochemical techniques in the following discussion.

With the elapsed time, the yellow colour on these samples without stimulation became deeper at day 5 and then changed to yellowish brown at day 7, and brown at day 10 (Figure 4.4). In contrast, with an applied stimulation, it displayed a brown colour at day 7 and dark-brown at day 10, meaning more Fe^{3+} compounds were formed on the surface. The surfaces of all specimens were completely covered by brownish corrosion products after 14 days, an evidence of a high degree of corrosion. FeOOH and Fe_2O_3 are the phases comprising this dark, relatively hard and brittle layer [277].

Figure 4.4 Photographs of the Fe anode without and with stimulation at day 3, day 5, day 7, day 10, and day 14.

The SEM images and XRD results of Fe anodes at Day 3 and Day 14 were chosen as representatives for Fe corrosion products at the early and later stages. To reveal the microstructure of corrosion scales, SEM images with localized feature are shown in Figures 4.5A and 4.5B. At day 3 without stimulation, the Fe surface was flat with mildly pitting corrosion. After the stimulation was applied, corrosion products of Fe showed different morphology with accumulation of agglomerated particles. It is probably because that more products are accumulated on the surface forming different scale.

XRD results of the Fe anode with and without battery stimulation are shown in Figure 4.5C. The XRD data indicates possible multicomponent products formation at various

energies [278-281]. The diffraction patterns show that the main species of these corrosion products formed under both conditions can be identified as FeOOH and Fe_2O_3 (Equations 4.8- 4.10 [282].

$$2FeOOH + Fe^{2+} \rightarrow Fe_3O_4 + 2H^+ \quad 4.8$$

$$2FeOOH+Fe+2H_2O \rightarrow 3Fe(OH)_2 \rightarrow Fe_3O_4 + 2H_2O+H_2 \quad 4.9$$

$$4Fe_3O_4 + O_2 \rightarrow 6\ Fe_2O_3 \quad 4.10$$

During the corrosion process, $Fe_2(OH)_2CO_3$ or $FeCO_3$ may probably be formed as the transition state (Equation 4.11, 4.12), however, both of them are unstable in the presence of O_2 forming FeOOH and Fe_2O_3 (Equation 4.13, 4.14) [283, 284]. The distinct peaks ((110) and (200)) of FeOOH disappeared after stimulation, meaning the transformation of FeOOH into Fe_2O_3 according to the reactions 4.8-4.10 [285].

$$2Fe(OH)_2+HCO_3^- \rightarrow Fe_2(OH)_2CO_3+H_2O +OH^- \quad 4.11$$

$$Fe^{2+}+ 2HCO_3^- \rightarrow Fe(HCO_3)_2 \rightarrow FeCO_3+ CO_2+H_2O \quad 4.12$$

$$2Fe_2(OH)_2CO_3+2\ H_2O+ O_2 \rightarrow 4FeOOH +2HCO_3^-+2H^+ \quad 4.13$$

$$FeCO_3 \rightarrow FeO+ CO_2\ ,\ 4FeO+ O_2 \rightarrow 2\ Fe_2O_3 \quad 4.14$$

The characteristic peaks of FeOOH at 2θ of 14º and 17º disappeared after the stimulation. The significantly increased peaks intensity ratio of (300)/(120) indicates that the amount of FeOOH had obviously decreased while the amount of Fe_2O_3 had increased (Figure 4.5C). It also indicates that the Fe anode suffered high degrees of corrosion, as Fe_2O_3 was formed as ultimate species in corrosion products following Equations 4.8 - 4.10 [276, 286]. They all demonstrate that the battery stimulation can enhance the Fe corrosion.

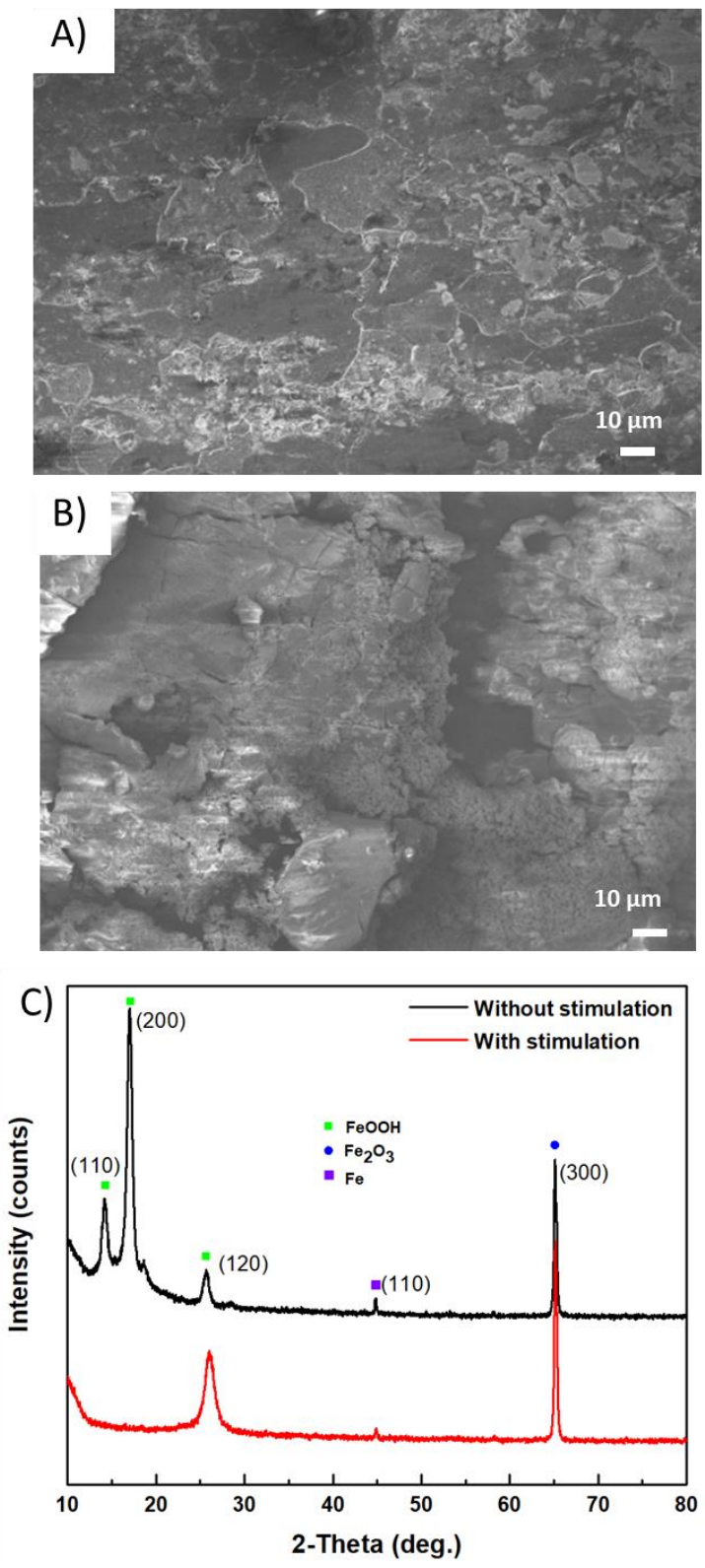

Figure 4.5 SEM images of the Fe anode surface after 3 days without (A) and with (B) battery stimulation; C) XRD results of the Fe anode surface without and with stimulation.

After 14 days, the Fe surface without or with stimulation in the culture media were almost covered by a dense layer of Fe products composing of particles (Figure 4.6A and 4.6B). Some cracks also presented, which may be caused by the dehydration after being dried.

It should be noted that the pronounced peaks of FeOOH at 14º and 17º for Fe without stimulation at day 3 completely disappeared at day 14 (Figure 4.6C). It clearly indicates a greatly decreased amount of FeOOH or even a disappearance; in the meantime, Fe_2O_3 became the dominant corrosion product. Compared with the XRD spectrum at day 3, a small speak at 32º (104) appeared at day 14, which may be attributed to trace of $FeCO_3$ on the surface that were not transformed to Fe_2O_3 via Equation 4.14 due to the limited access of O_2.

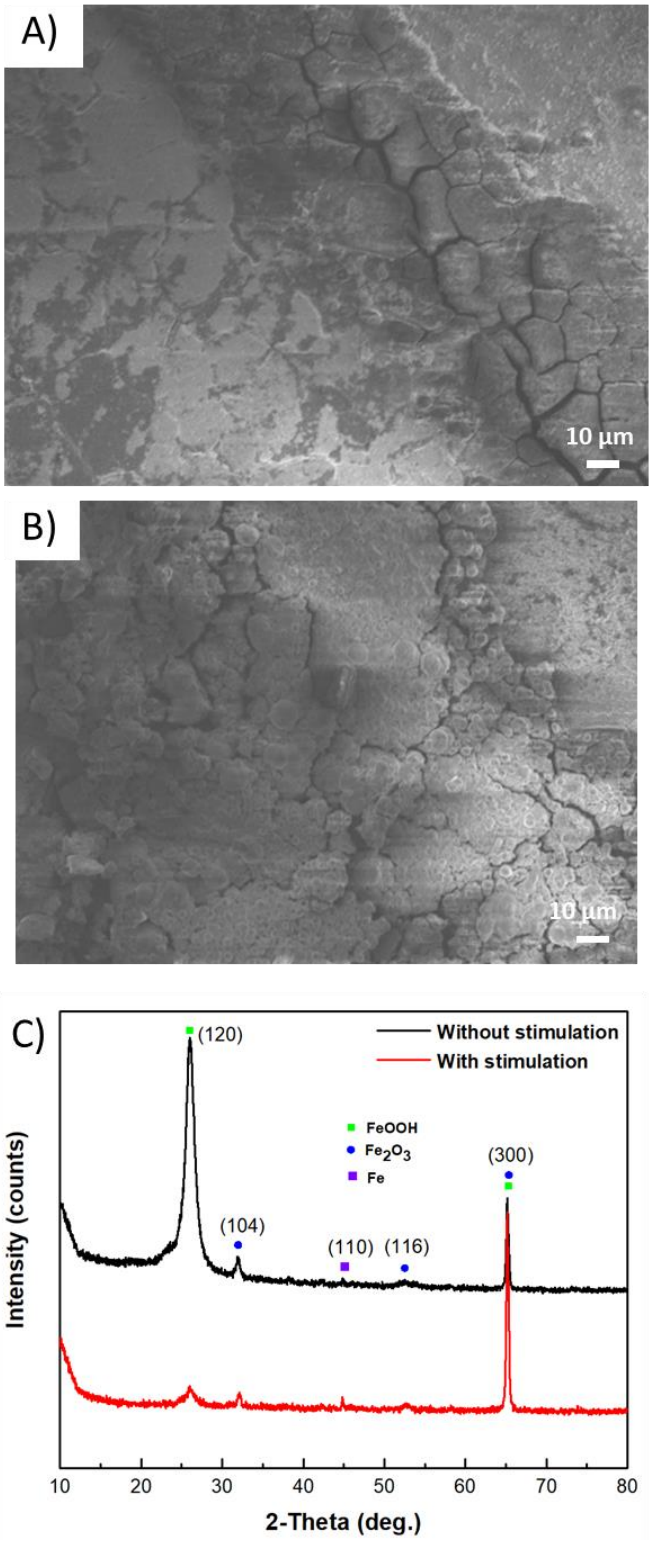

Figure 4.6 SEM images of the Fe anode surface after 14 days without A) and with B) battery stimulation; C) XRD spectrum on the corrosion scales of Fe without and with battery stimulation after 14 days.

The produced ferrous ion from the Fe anode may either dissolve in the water, or deposit as scales on the corroding metal surface. The amount of Fe released was indicated by the Fe content in the electrolyte, which included soluble species and scale particles detached from the surface due to the long-term contact with oxygen and water [277, 287]. The corrosion rate of Fe in culture media with and without battery discharge are illustrated in Figure 4.7. Fe concentration from the corrosion products in the electrolyte without or with stimulation were almost the same at day 3; then with battery stimulation it increased faster than that without stimulation. It also means that larger amounts of Fe products had been released into the electrolyte. This is probably due to the higher percentage of Fe_2O_3 corresponding to a higher Fe release [288]. The quantities of Fe released in both electrolytes at day 3 were quite low (less than 400 mg/L), and it reached over 1500 mg/L at day 14. The produced Fe ions was only about 4.5 mg within this Fe-air battery (3 mL electrolyte) during a 14 days period; they could be eventually transported by the fluid in the human body and excreted out, as Fe could be lost at a rate of 1mg/day through the gut, urine and skin [32].

Taking a typical human weight of 50 kg for example, the volume of blood participating in blood circulation is about 2800 ml. As calculated, it produced a Fe concentration of 1.6 µg/ml for a 50 kg adult; which is far lower than 50 µg/ml that expresses toxicity to cells and, therefore, this system is extremely safe for cells [261].

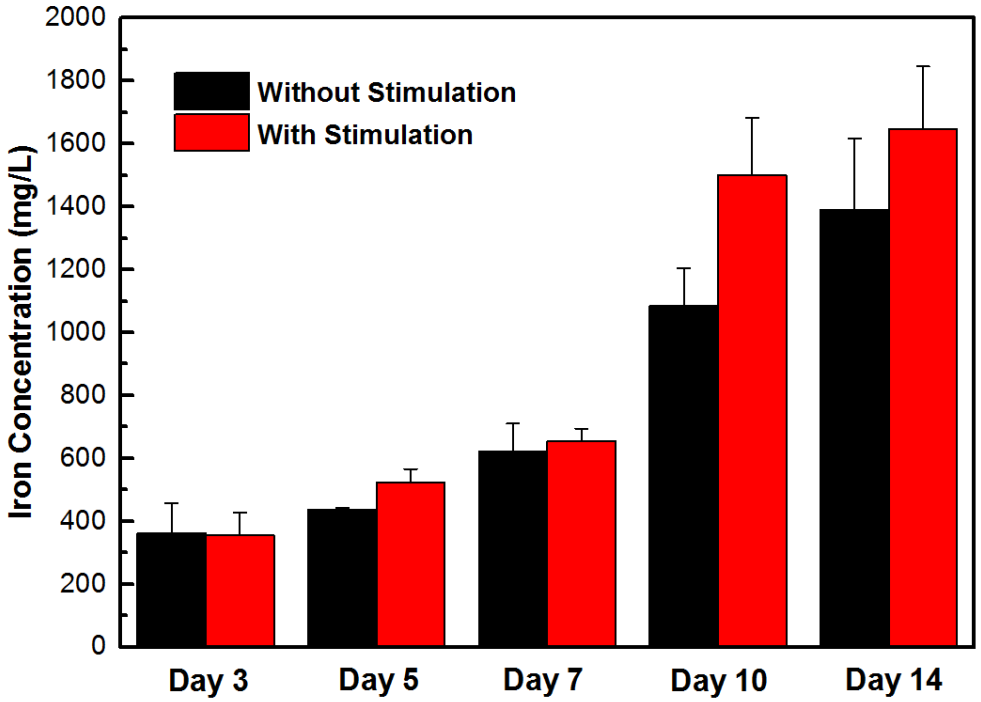

Figure 4.7 The released ion concentrations of Fe in the electrolyte with and without battery stimulation at day 3, day 5, day 7, day 10 and day 14.

EIS was utilized to evaluate the Fe anode corrosion. These results were displayed as Bode plots, in which impedance modulus was plotted versus the frequency (f) of the applied alternating current signal (Figure 4.8). When the frequency of an applied signal is low (f→0), the impedance reflects the polarization resistance (Rp) that is inversely proportional to the corrosion rate [289]. Therefore, the impedance modulus Z_{real} at the lowest frequency in Bode impedance plots can be used as a semi-quantitative indicator of Fe corrosion rate (i.e., a rate of Fe release and oxide growth). The impedance at day 3 with stimulation was about 1987 $\Omega \cdot cm^2$， far lower than that of 3750 $\Omega \cdot cm^2$ without stimulation, indicating the decreasing corrosion resistance and increased corrosion rate. No matter whether with or without stimulation, the impedance at D14 was both kept at a very low value of 170 $\Omega.cm^2$. It was probably

due to the extremely high Fe oxide growth that indicates a high Fe corrosion rate (shown as the brown-black colour in Figure 4.4).

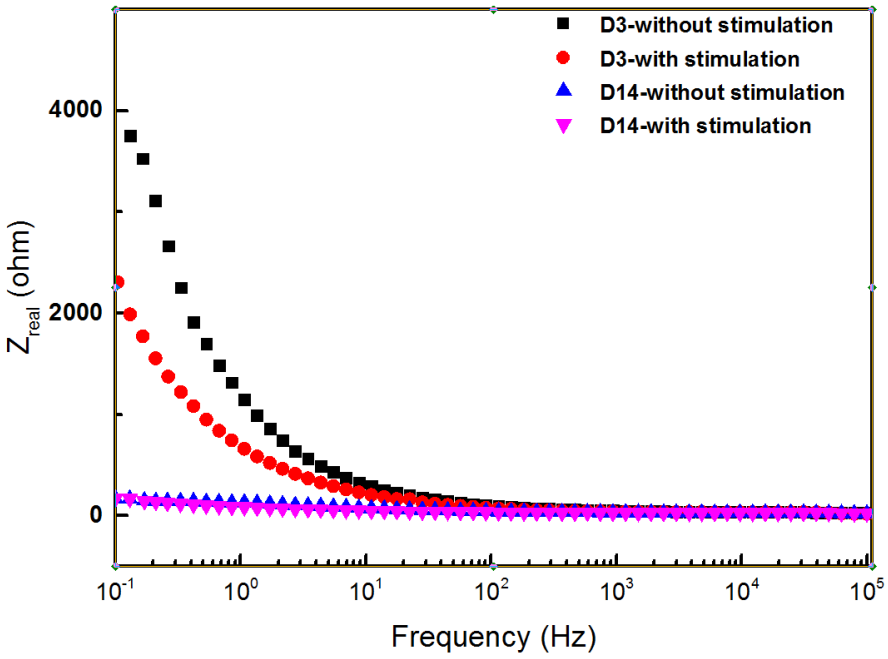

Figure 4.8 Bode impedance plots of Fe anode after 3 days and after 14 days without and with stimulation.

E_{corr} is the potential at which the rate of metal dissolution reaction equals to the rate of oxygen reduction reaction, which can be used to examine the corrosion rate of metals. Cathodic polarisation curves in culture media without and with battery stimulation for 3 days and 14 days are shown in Figure 4.9, and the related values are listed in Table 4.1. It is noted that there is a slight shift of corrosion potential towards positive values after the stimulation from to -0.64 V after 3 days, from -0.63 to -0.61 V after 14 days. The potential difference of 0.03V was equal to the value difference of sample without stimulation at day 3 (-0.66 V) and day 14 (-0.63) during a long period of corrosion. These results demonstrated an easier anodic reaction and the accelerated anodic reactions for Fe corrosion.

However, the cathodic polarization curves did not display the expected linear Tafel plot over the applied potential range, which is probably attributed to the deposition of corrosion products on the Fe surface to form a non-reactive inhibiting film [290]. The corrosion rate can also be determined by Tafel extrapolation of either cathodic or anodic polarization curve alone. The anodic curve is used for better defining the Tafel region, as the cathodic polarization induces concentration effects with deviations from Tafel behaviour due to the diffusion limitation [290]. The cathodic slope with stimulation was lower than that without stimulation at day 3 and day 14 (Table 4.1), which is probably due to the impeded O_2 diffusion by the higher amount of accumulated corrosion products on the Fe anode after stimulation.

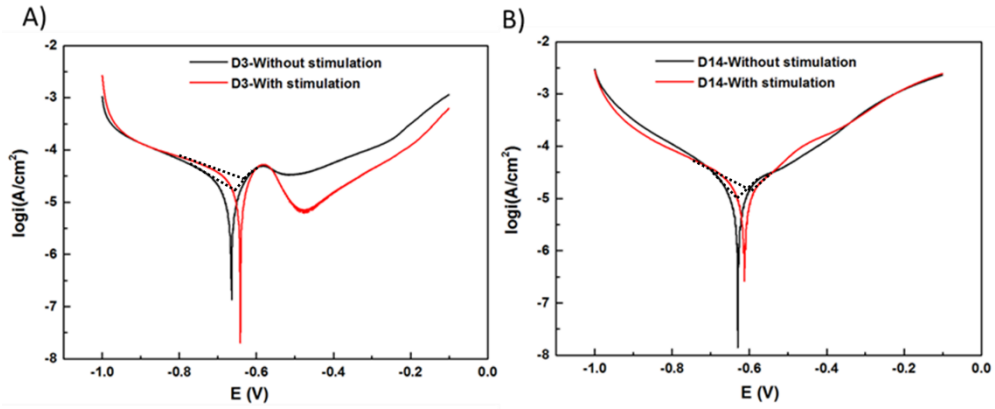

Figure 4.9 Tafel plot of Fe anode without and with battery stimulation at day 3 and day 14.

Consistently, the anodic slope increased from 3.5 without stimulation to 11.0 with 3 days stimulation, from 3.2 to 6.8 during a 14 days period. These results clearly demonstrate the promotion effect on the anodic reactions with the battery stimulation. The anodic reactions result in a localized form of corrosion, such as pitting, intergranular corrosion, or galvanic corrosion [291], which is consistent with the non-uniform corrosion morphology as shown in Figure 4.4 .

Table 4.1 Cathodic and anodic slope of the Tafel curves at day 3 and day 14.

	Cathodic slope	Anodic slope
D3 Without stimulation	4.2	3.5
D3 With stimulation	3.3	11.0
D14 Without stimulation	5.7	3.2
D14 With stimulation	4.1	6.78

4.3.3 Metabolic activity of cells with and without battery stimulation

The cytocompatibility of the Fe-air battery with/without discharging was evaluated using human adipose-derived stem cells (hADSCs). As shown in the live/dead fluorescence staining (Figure 4.10), all the hADSCs were well spread and reached high confluence at day 21 after seeding on PPy/PEDOT hydrogel cathode of this battery system without or with battery discharging stimulation, demonstrating the cytocompatibility of this battery.

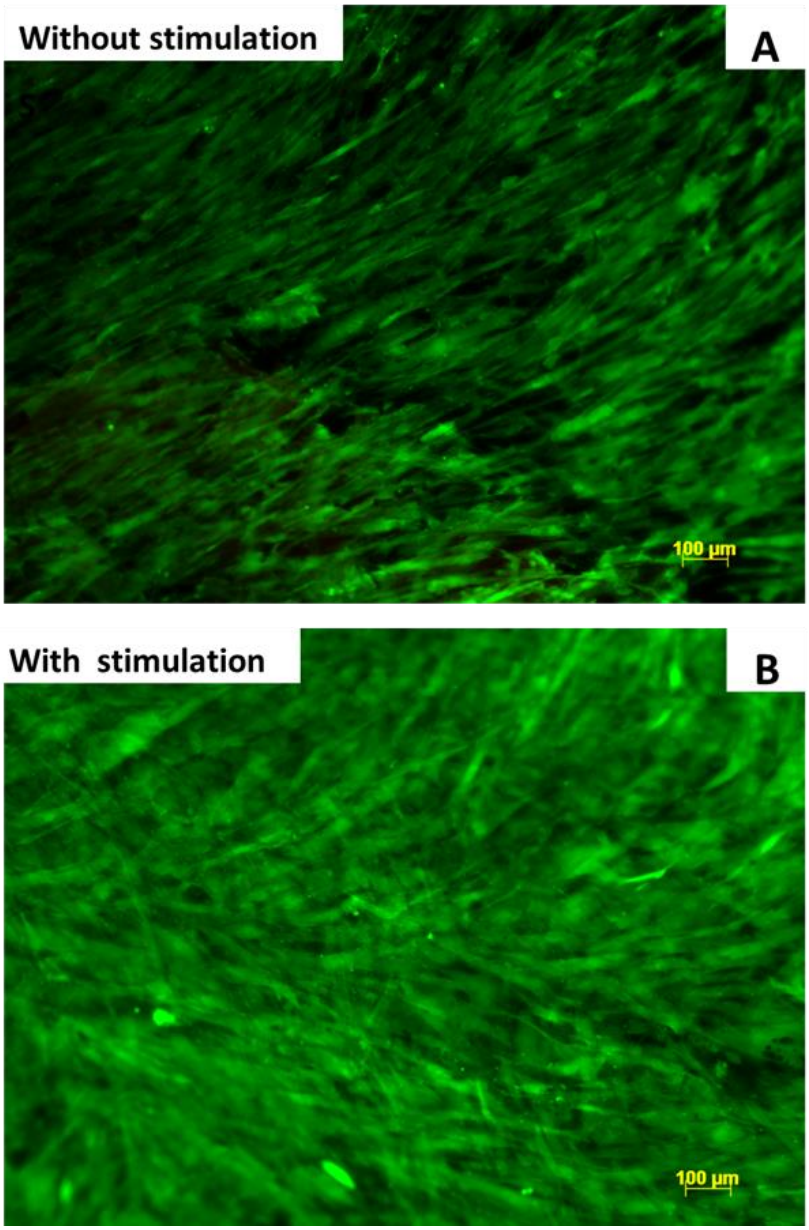

Figure 4.10 Fluorescence images of the ADSCs on PPy/PEDOT hydrogel of an Fe-air battery without A) and with B) stimulation for 21 days.

The total cell metabolic activity, characteristic of cell proliferation, increased gradually in 2 weeks (Figure 4.11). It demonstrates that this battery can well support the proliferation of hADSCs as well. However, cell metabolic activity increased slower with battery stimulation, which could be related to the higher Fe concentration in the culture media. The higher Fe concentration negatively influenced the growth-

related gene expression [263]. The problem of localised high Fe concentration is probably solved if the Fe battery is directly implanted in the body, as these localised Fe ions would diffuse and transport much quicker by physiological fluids, as body fluid is a circulatory system.

As demonstrated above, all the materials involved in this Fe battery are cyto-compatible, and cells could well attach and proliferate on PPy/PEDOT hydrogel cathode even when the battery was at the discharged state for providing power. These results indicate that this Fe-air battery may be safe and efficacious for implantation. It is also reasonable to infer that the power generated by this battery may directly deliver the energy to regulate the cell behaviours (e.g., cell migration).

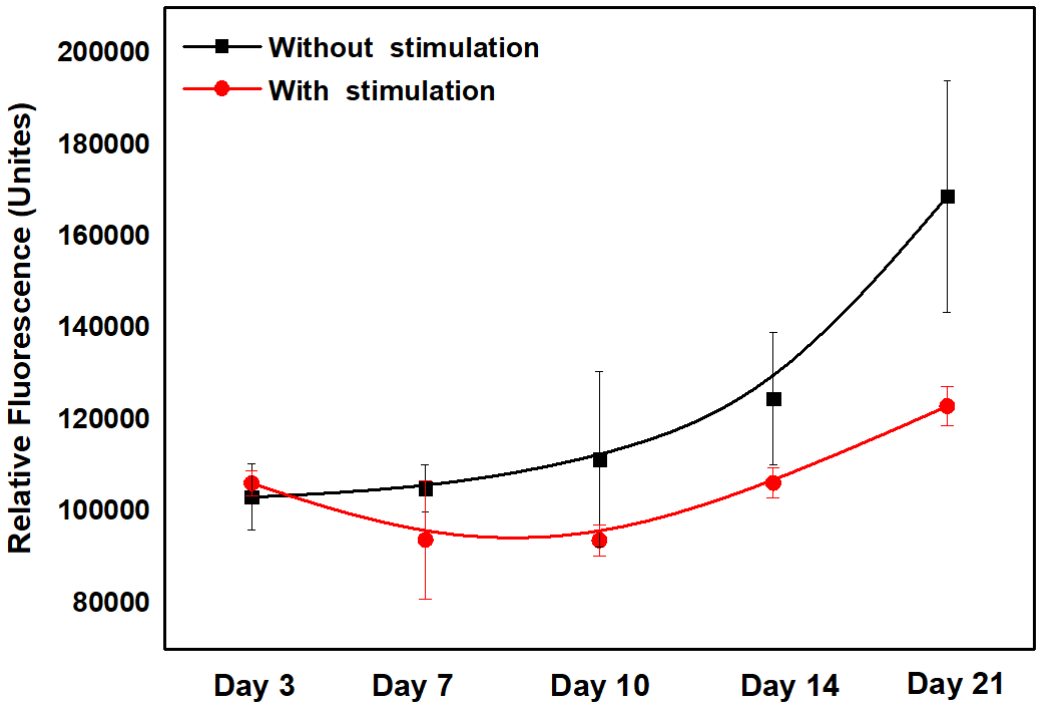

Figure 4.11 Growth curve of ADSCs on an Fe-air battery at day 3, 7, 10, 14 and 21.

4.4 Conclusions

In summary, a novel dynamic method to improve the degradation of Fe stent is developed by coupling with a conducting polymer hydrogel cathode to form a bioelectric battery. This battery provides a capacity of 1.3 mAh cm^{-2}. In the meantime, the electrochemical reactions of the ORR at the cathode induces the oxidation reaction at the Fe anode thus accelerating the Fe corrosion compared with the static Fe corrosion. In addition, this battery showed good cytocompatibility, and can support the attachment and proliferation of adipose-derived stem cells during a 14 days period under the working system with a stable voltage around 0.65 V for 2 hours per day. It is a promising method to solve the low degradation rate of Fe stent and provide the energy for biological activities (e.g., cell migration) at the same time.

Chapter 5 A Smart Cyto-compatible Asymmetric Polypyrrole Membrane for Salinity Power Generation

This chapter is adapted from the article, "A smart cyto-compatible asymmetric polypyrrole membrane for salinity power generation", by Changchun Yu, Xuanbo Zhu, Caiyun Wang, Yahong Zhou, Xiaoteng Jia, Lei Jiang, Xiao Liu, and Gordon G. Wallace, that was published in Nano Energy 53 (2018): 475-482, with the permission from Elsevier.

5.1 Introduction

Salinity gradient power is a clean and sustainable form of energy that can be captured from water via partitioning two aqueous solutions of different salinities across a membrane [292]. For salinity energy conversion process, the membranes used to capture this type of energy screen the passing ions, resulting in a net electrical current. Inspired by biological channels that exist in nature, smart biomimetic nanofluidic systems have been built to enable salinity power harvesting. They commonly feature a nano-porous structure with a specific surface charge (cationic or anionic) [293, 294]. Smart membranes with artificial biological ion channels are capable of reproducing the biological energy conversion process based on a salinity gradient as well as making biomimetic responses by responding to environmental stimuli such as pH, temperature, light or electrical potential [97-100]. Such membranes have also been used for nanofluidic devices, biosensing and drug delivery [295-297]. Membranes containing these nanochannels are commonly fabricated by a self-assembly process, ion track

etching, or electrochemical etching with limited scope for scale-up [101-103]. Typically “smart” nanochannels can be either directly fabricated with functional materials or indirectly by surface modifying these nanochannels with functional molecules [104]. A single component membrane is highly desirable for simplicity.

PPy possesses the properties of ionic as well as electronic conductivity [126]. It has been used extensively in the area of bioengineering and energy storage owing to its biocompatibility and electroactivity [125, 193]. The defects in its π-electron system (polarons, bipolarons) can act as positive charge carriers favouring the conduction of mobile anions within the polymer backbone [156]. PPy has been used previously as an ion-exchange membrane with controllable ion transport via an externally applied potential [298, 299]. With the ion selectivity, PPy has the potential for use in salinity power generation. To date, heterogeneous membranes incorporating PPy as a component, such as alumina/PPy, poly (acrylamide-co-acrylicacid)/PPy membrane, have been developed to realise the smart pH/light or electro/pH modulated ion transport [300, 301]. In these studies, the PPy layer was electrodeposited on a pre-fabricated nanoporous scaffold. The inherent incompatibility between two components may lead to a phase separation [302]. It would be highly desirable if a one component PPy membrane with an asymmetric porous structure could achieve all these smart functions. However, no such membrane has been demonstrated yet.

In this chapter, a smart single component porous PPy membrane with an asymmetric structure was prepared via a facile self-assembly process. It is a cytocompatible substrate for Adipose-derived stem cell adhesion and proliferation. This membrane was used for salinity gradient power generation with an electrochemically tuneable ionic conductance as well. It can be anticipated that this single component PPy

membrane would be a promising smart material for energy harvesting and biomimetic applications.

5.2 Experimental

5.2.1 Fabrication of free-standing PPy membrane

The free-standing PPy membrane was formed at an aqueous/organic interface following the reported procedures with some modifications [303]. Briefly, pyrrole was dissolved in chloroform to form the organic phase (0.1 M, 10 ml). $FeCl_3$ (0.15 M) and Tween-80 (0, 0.5, 2, 4 g/L) were added into Milli-Q water (10 mL) to form the aqueous phase. These two solutions were pre-cooled in an ice-salt bath (weight ratio of ice to salt was 30:1). Then the aqueous solution was gently transferred onto the top of the organic phase. The reaction was initiated when PPy monomer encountered $FeCl_3$, and the reaction proceeded for 24 hours in the ice-salt bath. The formed film was washed alternately with water and ethanol, then dehydrated using ethanol and dried in air.

5.2.2 Cell work

PPy membranes were sterilised by soaking in ethanol for 30 min and exposed to UV-light for 20 min. Then they were placed into a 24-well polystyrene cell culture plate and soaked overnight with culture medium, followed by rinsing with PBS twice. Adipose-derived stem cells (hADSCs) were seeded in the well with an initial density of 2×10^4 cells/cm^2. Cell viability and proliferation ability investigations were done by following the steps described in Chapter 2 (Section 2.3.2). For SEM imaging, the hADSCs were fixed in 3.7% paraformaldehyde for 1 h at room temperature, followed by a freezing process in liquid nitrogen and a subsequent freeze-drying process.

5.2.3 Characterisation

Electrical measurements were conducted by mounting the PPy membrane with a solution contact area of 3.14 mm^2 (e.g., diameter 2 mm) between two halves of a custom-made electrochemical cell where 2 mL electrolyte was added into each half-cell. The membrane was immersed in ethanol to increase its surface tension prior to the ion transportation experiments, which could enable ions to pass through the membrane easily. The current-voltage was recorded by a Keithley picoammeter. Redox potential is obtained in the same electrochemical cell where the separator PPy membrane between two half-cells was replaced by a nonselective silicon membrane containing a single micro-window (side length~10 μm).

5.3 Results and discussions

5.3.1 Preparation and characterization of PPy membrane

The PPy membrane was fabricated using interfacial polymerization in a salt-ice bath (Figure 5.1). Reactants (pyrrole and oxidant $FeCl_3$) dissolved in each of the immiscible phases reacted at the interface to form the insoluble membrane [304]. The pyrrole monomer diffused into the water layer, and seated at the hydrophobic tail of surfactant molecules through secondary forces such as π–π interactions and hydrogen-bonding [305]. The surfactant Tween-80 molecules (0.5 g/L) aggregated into core–shell cylindrical micelles, in which four long chains entangled with one another through intra- and inter- molecular interactions at the applied condition [306]. The unidirectional growth of PPy proceeded with the continuous supply of pyrrole monomer and created an interconnected 3D porous structure.

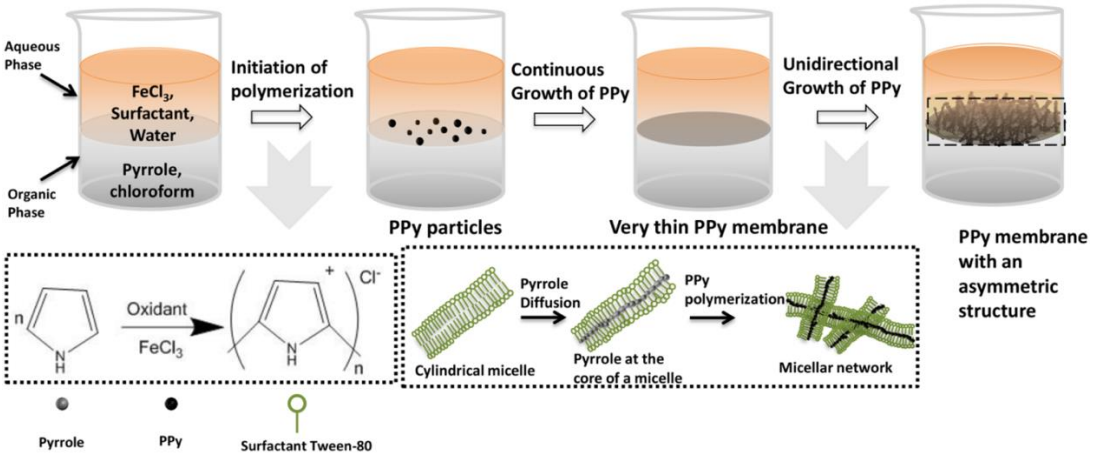

Figure 5.1 Schematic diagram of the PPy growth via interfacial polymerization method.

A black membrane with a diameter of 4 cm (size of the reaction container) was formed at the interface after 24 h interfacial reaction. This free-standing film was robust, offering a conductivity around 200 S/m and a thickness of 20 μm (Figure 5.2A). The surface in contact with the aqueous or organic phase is referred to as PPy-A and PPy-O, respectively. It displayed an asymmetric structure as shown in the cross-sectional view in Figure 5.2B: a uniformly interconnected 3D porous structure on the PPy-A surface, and a planar macroporous structure on the PPy-O surface.

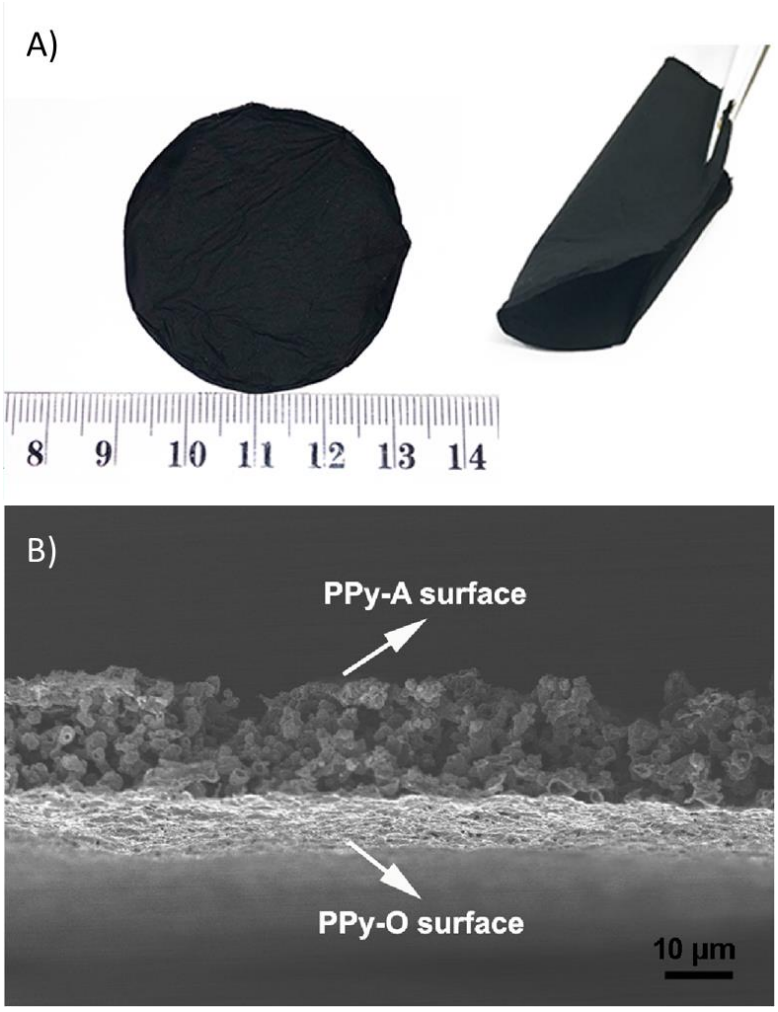

Figure 5.2 (A) Photograph of the free-standing PPy film, and a demonstration that it can be curled by a tweezer; (B) SEM images of a cross-sectional view of this PPy membrane.

The morphology of PPy-A and PPy-O are shown in Figure 5.3A and Figure 5.3C respectively. Those two faces of this film displayed different wettability as evidenced by the observed contact angles: ~151° on the hydrophobic PPy-A surface (Figure 5.3B); and ~85° on the hydrophilic PPy-O surface (Figure 5.3D). The wettability of a solid surface is governed by both chemical composition and microstructure [307]. In addition, an isotropic wettability was observed on the PPy-A surface where water droplets could roll in different directions with equal ease, evidencing a uniform PPy-

A surface. Such a film with asymmetric wettability (hydrophobicity on PPy-A surface, hydrophilic on PPy-O surface) would find broad applications, such as micro-fluidic devices, liquid transfer, and bio-inspired systems [308].

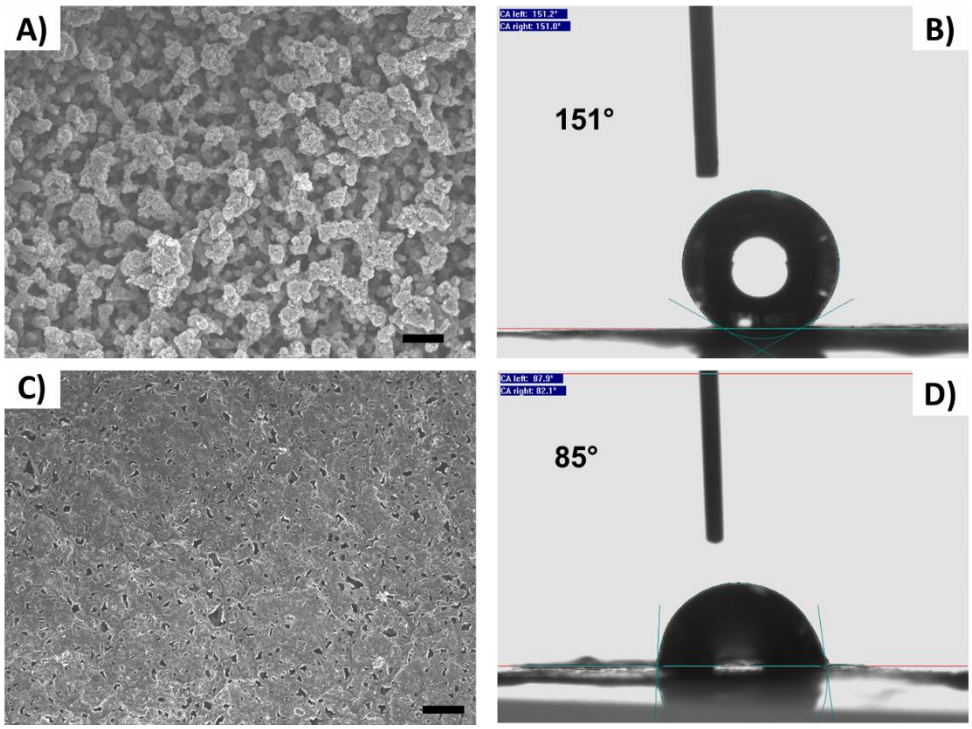

Figure 5.3 SEM images of (A) PPy-A surface and (C) PPy-O surface, contact angle of water droplet on the (B) PPy-A surface and (D)PPy-O surface.

More specifically, PPy-A surface displayed a gradient pore distribution with pore size in a range of 1~30 μm, while the average pore size of the PPy-O surface membrane was around 1.3 μm (Figure 5.4). Aggregated PPy granules can be clearly observed, and they were stacked up to tens of micrometres.

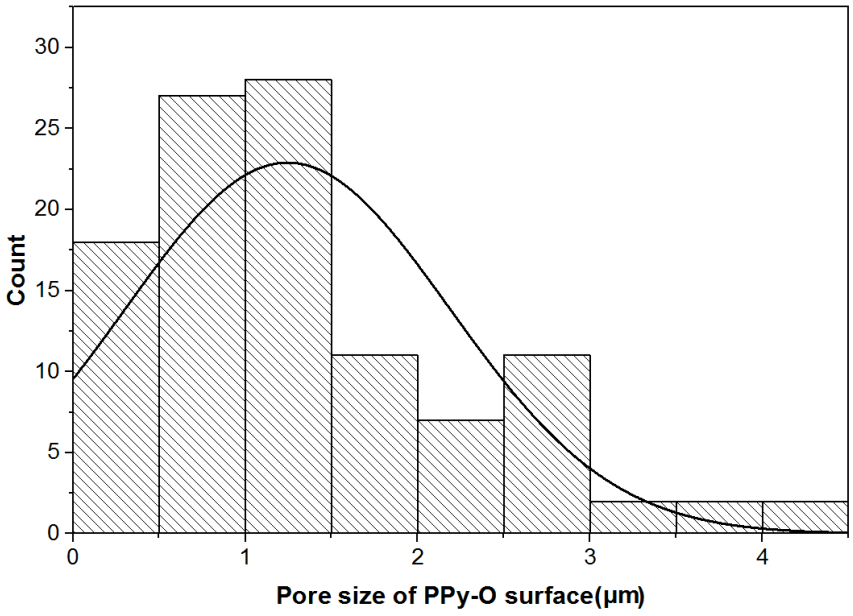

Figure 5.4 Statistical pore size distributions of PPy-O surface, calculated from 100 pores in the SEM observations.

The surfactant is important to form the interesting structure. Without the presence of surfactant, the produced PPy membrane was very thin and transparent black (Figure 5.5A). It displayed an integrated fibre network with large amount of pores in large sizes (up to 20 μm). This is attributed to the limited amount of pyrrole available for the polymerization. When the surfactant concentration was increased to 2 g/L and 4 g/L, larger vesicles were formed (Figure 5.5B, 5.5C). The increased volumes and numbers of micelles induced a simple merging mutually because of the lowered interfacial tension, following the PPy growth in this merged micelle model [309].

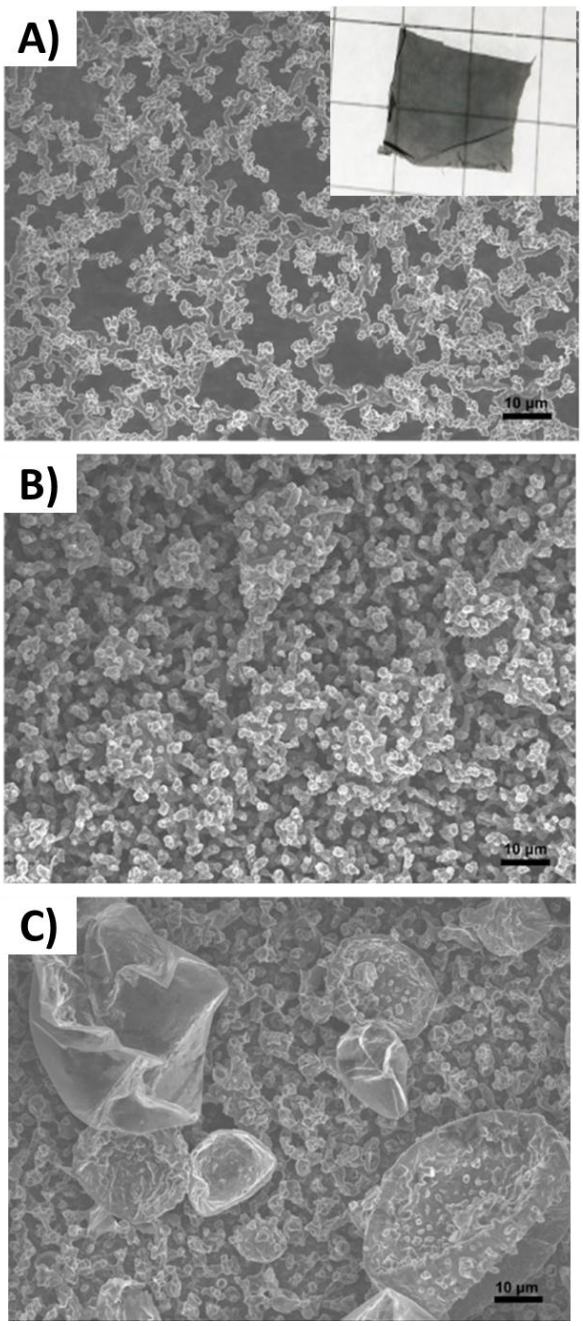

Figure 5.5 SEM images of the formed PPy from the solution containing Tween-80 surfactant at a concentration of (A) 0 g/L; (B) 2 g/L; and (C) 4 g/L. Inset of A) shows that the film is very thin in black colour.

Another important factor for this novel PPy formation is temperature. When the reaction temperature was elevated (in an ice bath), the produced PPy membrane became much thicker (~100 µm, Figure 5.6). These results clearly demonstrate that

formation of this porous PPy membrane can be easily modulated by controlling the used surfactant and temperature. It is also reasonable to deduce that the formed structure can be further tuned with different types of surfactant having different micelle shapes. It should be noted that this facile chemical polymerization method can be easily scaled up.

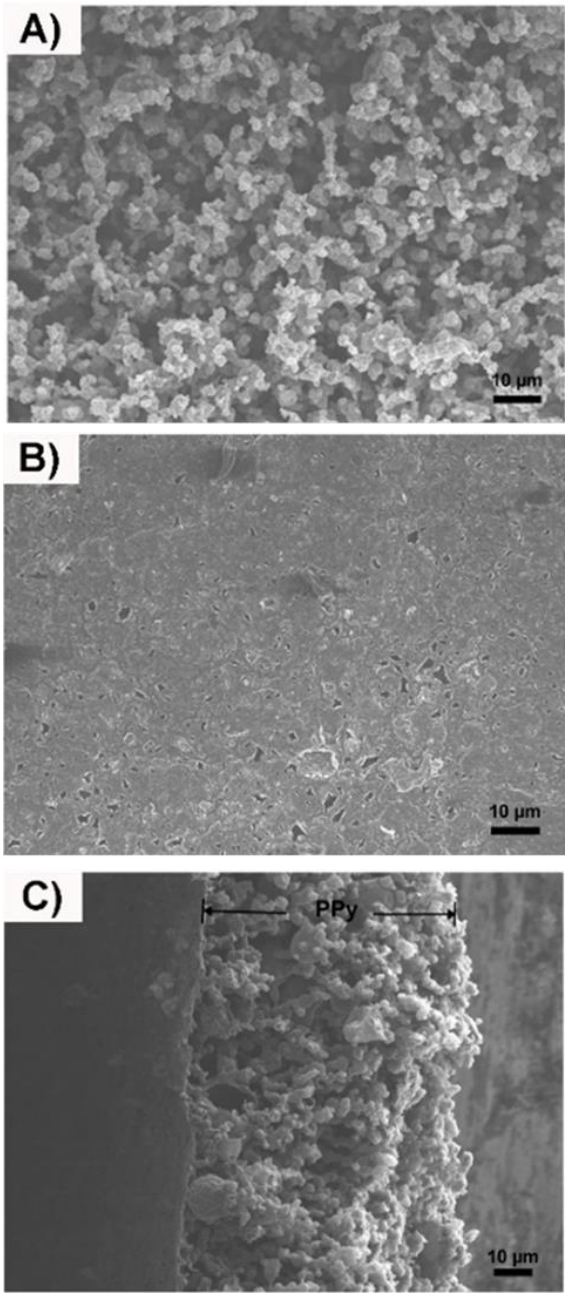

Figure 5.6 SEM images of the formed PPy in an ice bath: (A) PPy-A surface, (B) PPy-O surface, and (C) cross-sectional view.

This PPy film demonstrated the characteristic bands of PPy in the FTIR spectrum (Figure 5.7): the band at 925 cm^{-1} is attributed to C–H wagging [310]; band at 1565 cm^{-1} corresponds to C=C stretching; and band at 1311 cm^{-1} represents C–N bonds [311].

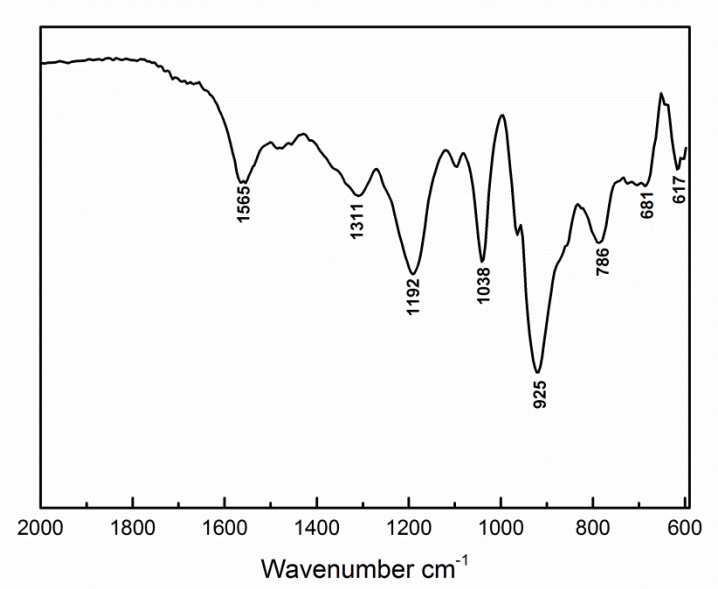

Figure 5.7 FTIR spectrum of a PPy membrane.

5.3.2 Ion transport properties of PPy membrane and its application for salinity power generation

An electrochemical system (Figure 5.8) was used to examine the ionic transport properties of this PPy membrane by measuring the transmembrane ionic current. The electrode used was Ag/AgCl, which was placed on each side of the membrane for the measuring. The positively charged backbone of PPy attracted counterions Cl^- to ensure the electroneutrality. The electrochemical potential difference between the solutions

is the driving force for ion transport. As a result, electrons can be transferred from one electrode to another via an external electrical circuit, generating an electrical current [76]. In short, the ion flux was driven by chemical potential through the positively charged PPy pores, forming a diffusion current composed of mostly negatively charged ions.

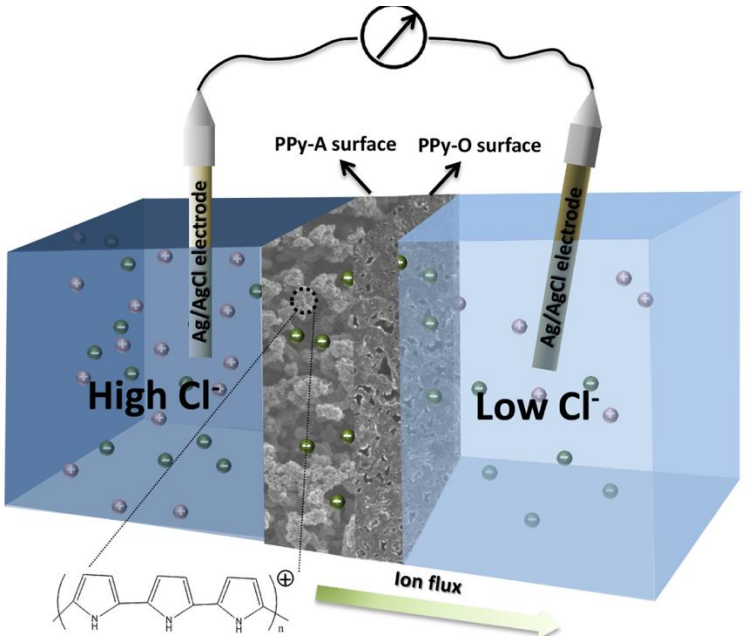

Figure 5.8 Schematic illustration of the energy harvesting with a PPy membrane under a concentration gradient.

The electrolyte concentration at the PPy-O side was fixed at 1 µM, and that at the PPy-A side was gradually elevated from 1 µM to 1 M. The voltage generated was in the range of several to hundreds of mV (Figure 5.9, *I–V* response), comparable to the reported result for an ionic diode carbon membrane [312]. The redox reactions ($Ag + Cl^- \Leftrightarrow AgCl + e$) on the electrodes contributed to the obtained potentials as well. The electric potential generated in the micropores is given by $V = V_{out} - V_{redox}$, V_{out} is the voltage output read from a source meter, V_{redox} is the potential difference between two Ag/AgCl electrodes [312].

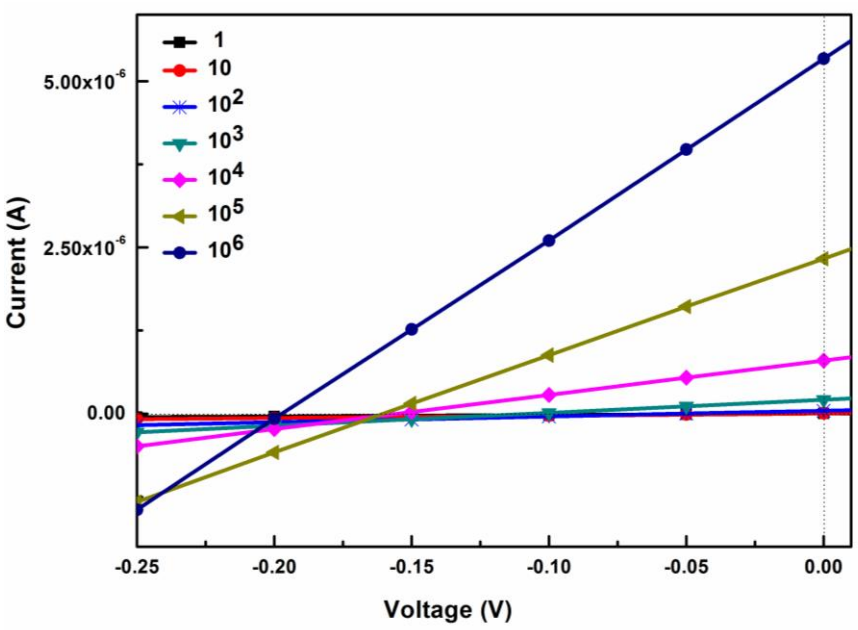

Figure 5.9 Current-voltage (I-V) response of a PPy membrane in KCl solution at different gradient ratios ranging from 1 to 10^6.

All these three potentials are listed in Table 5.1. The measured potential reached a high potential of 207 mV at a gradient ratio of 10^6 (Figure 5.10), where the potential generated in the micropores was 95 mV. For the concentration gradients lower than $10^{-6}/10^{-3}$, the membrane showed much lower potentials and thus are not shown, which may be due to its poor ion selectivity.

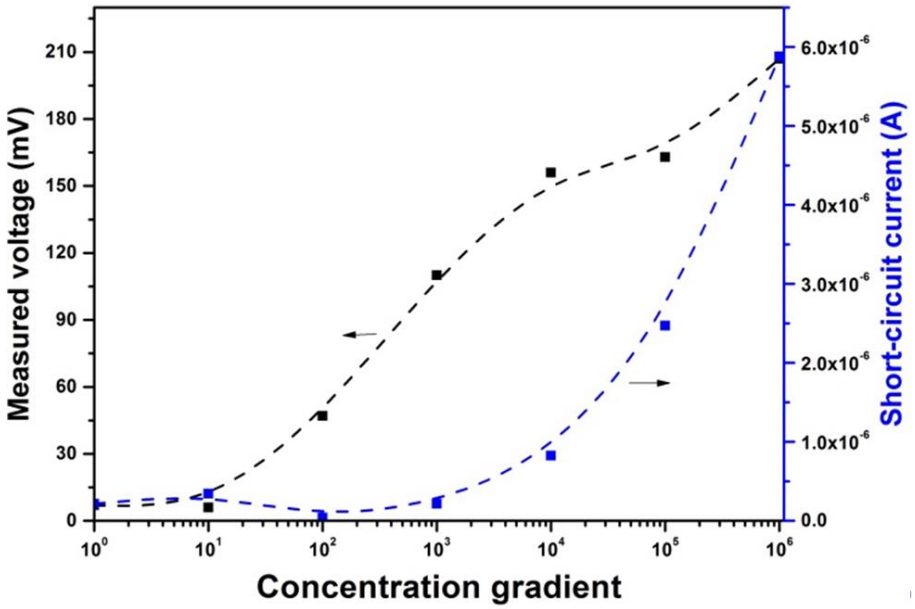

Figure 5.10 Short circuit current and measured output voltage at the different concentration gradients, both the voltage and current increase with the salinity gradients.

Table 5.1 Measured output potential, redox potential and membrane potential of the energy conversion system with different concentration gradients.

Concentration gradient (M/M)	$10^{-6}/10^{-3}$	$10^{-6}/10^{-2}$	$10^{-6}/10^{-1}$	$10^{-6}/1$
Output potential (mV)	110	156	163	207
Redox potential (mV)	73	82	100	112
Membrane potential (mV)	37	74	63	95

In this electrochemical system, a potential of 163 mV was obtained from the 0.1M/1μM gradient when high salt concentration solution was placed at the hydrophobic PPy-A side, much higher than that 69 mV from the reverse concentration gradient (Figure 5.11). It also means that the diffusion electric field was stronger from the PPy-A surface to PPy-O surface. This may be explained by the difference in charge density at these two faces: PPy-A surface might be at a higher doped state with a higher charge density, since sufficient oxidant $FeCl_3$ was available for the polymerization in the aqueous phase. In addition, it is favourable for ions to transfer from PPy-A surface to PPy-O surface as water tends to transfer from the hydrophobic side to the hydrophilic side [313, 314]. Thus, the difference in the charge density as well as

surface structure render an ion permselectivity. Such a selective ion diffusion will endow this PPy membrane with a broad range of applications such as charge separation process, and nanofluidic sensing devices.

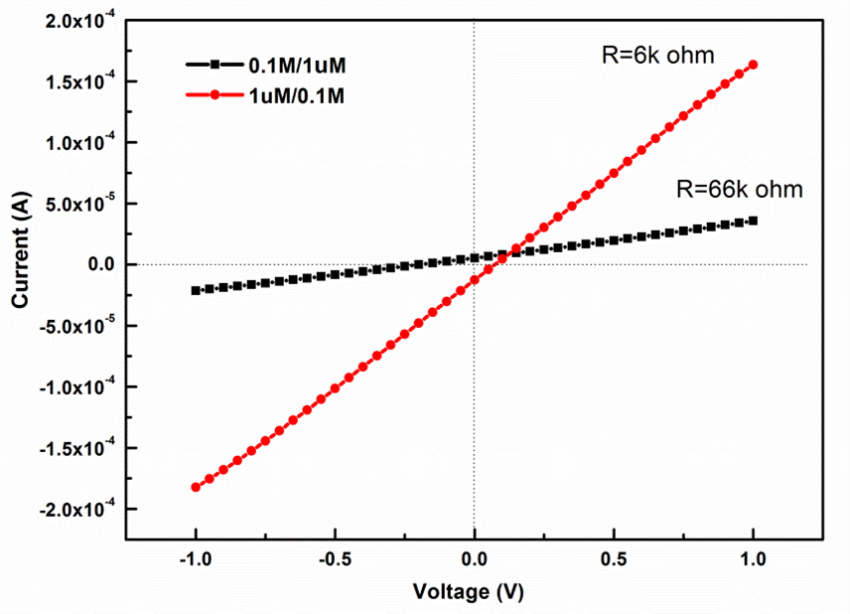

Figure 5.11 Internal resistance of the fluid system at the reversed concentration gradient. For the 0.1 M/1 μM gradient, U and I were 163 mV and 2.47 μA, respectively; in contrast to that 69 mV and -12 μA obtained when the concentration gradient was reversed.

The ion selectivity of a membrane can be characterised with transference number, that is calculated by referring to the formula $t_n = \frac{1}{2}\left(\frac{V_{diff}}{V_{redox}} + 1\right)$ [315]. It is noticed that the transference number displayed the lowest value t_n of 0.75 at the lowest solution gradients of $10^{-6}/10^{-3}$ (Table 5.2). It is different from the commonly reported trend that the transference number increased with the decreasing electrolyte concentration, as the effective concentration of ions required to neutralize the surface charge became larger compared to the bulk ion concentration in the nanochannels [316]. This phenomenon for PPy membrane may be explained by the decreased surface charge density due to

the diffusion of the dopant Cl ions in the PPy membrane into the electrolyte attributed to the osmotic pressure [170, 317], since PPy is a unique material that affords charge transport both ionically and electronically allowing the in and out movement of the doped ions [318, 319]. When the concentration gradient increased to $10^{-6}/10^{-2}$, $10^{-6}/10^{-1}$ and $10^{-6}/1$, an equilibrium distribution of Cl ions across the membrane/electrolyte interface is probably formed, which results in a higher surface charge density and thus a higher t_n.

Table 5.2 Transference number for various combinations of concentrations.

Concentration gradient(M/M)	$10^{-6}/10^{-3}$	$10^{-6}/10^{-2}$	$10^{-6}/10^{-1}$	$10^{-6}/1$
Transference number	0.75	0.95	0.82	0.92

The ionic transport property of this PPy membrane in different concentrations of KCl solution was examined (Figure 5.12). The conductance decreased nonlinearly with the concentration and notably deviated from the bulk value from 10^{-3} M, shown as the dashed line (a linear trend of ionic conductance with the decreased concentration), indicating surface-charge-governed ion transport. At low concentrations, the water/ion ratio makes the average distance between ions quite high, which enables ions to redistribute realising effective screening [320].

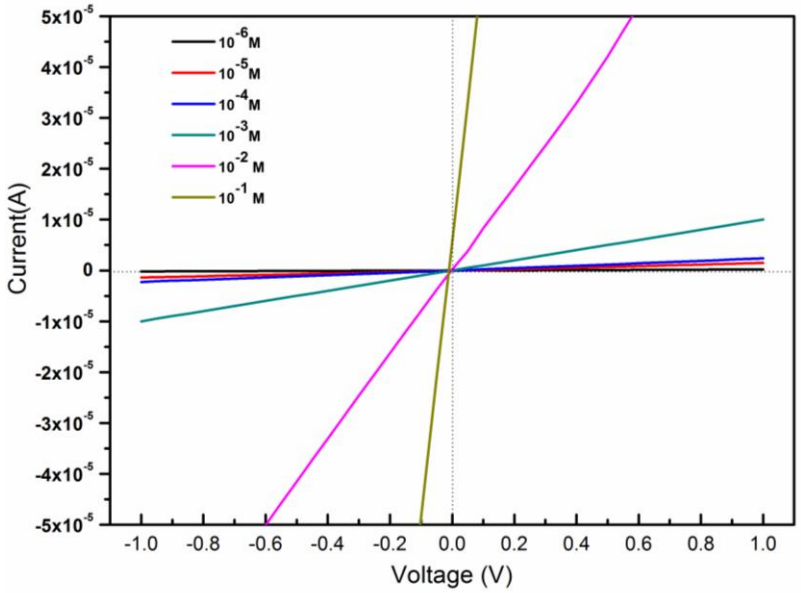

Figure 5.12 Current-voltage response of a PPy membrane in the KCl solution with the concentration from 10^{-6} to 10^{-1} M.

The conductance was governed by the surface charge density inside the pores when the Debye screening length (24 nm for 10^{-3} M KCl electrolyte) increased to a value comparable to the pore size at low solution concentration [321]. Debye screening length can be deducted by the following method: charged channels possess ion selective properties due to the electrical double layer, whose thickness is characterised by the Debye screening length $\lambda_D = \sqrt{(\frac{\varepsilon\varepsilon_0 K_B T}{2cz^2e^2})}$; where ε is the dielectric constant of the solvent, ε_0 is the permittivity of vacuum, K_B is the Boltzmann constant, T is the absolute temperature, c is the concentration of ionic solution, z is the valence of the ion, and e is the electron charge.

It is also noticed that the conductance displayed a sharp conductance drop again at 10^{-6} M. This might be explained by that a large amount of dopant Cl ions in PPy

membrane diffused into this extremely low electrolyte, leading to greatly decreased ion selectivity as discussed above.

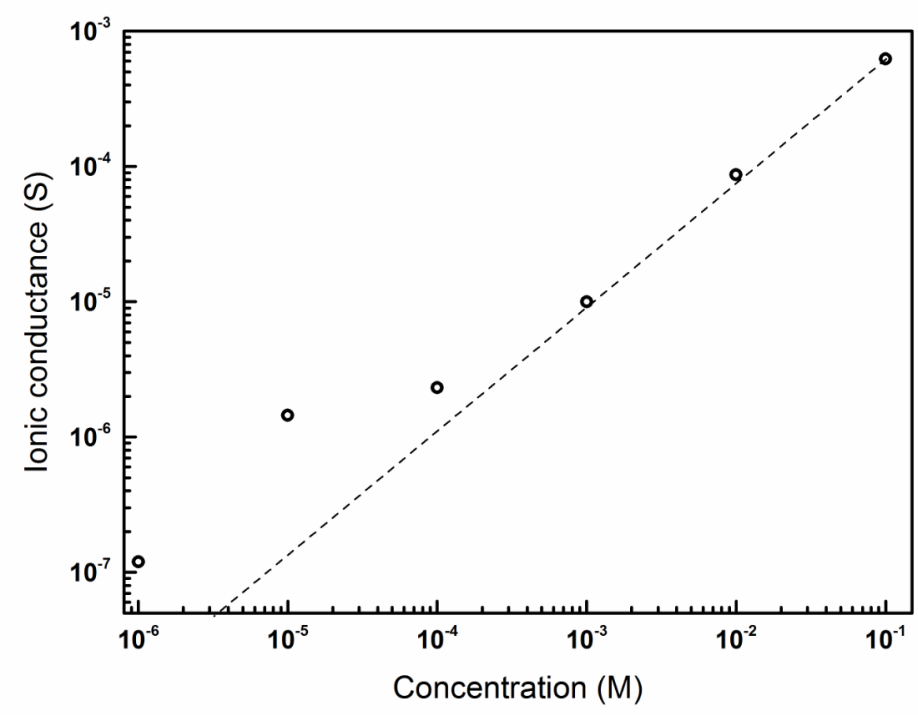

Figure 5.13 Ionic conductance of a PPy membrane in different concentrations of KCl solution.

This membrane could also be used as an ion exchange membrane to collect salinity gradient energy due to its ion selectivity. The harvested power which is consumed on the electric load can be calculated as $P_{out}= I^2 \times R$, where I is the electric current through the resistor. The power density generated from a gradient using artificial seawater (0.5 M NaCl) and river water (0.01 M NaCl) reached a peak value of 0.087 W/m^2 at an external resistance of ~5 KΩ (Figure 5.14). A current density of 2 A/m^2 was generated and remained stable during the monitored time of 16 h, affording an energy density of 1.4 Wh/m^2 (Figure 5.15). The ability of component PPy membrane to capture salinity gradient power is attributed to its ion permselectivity, and the preferred ion

transportation within the asymmetric structure. It should be noted that this PPy membrane is composed of only one component and can be easily fabricated via a chemical synthesis route, which is suitable for large scale production [322, 323].

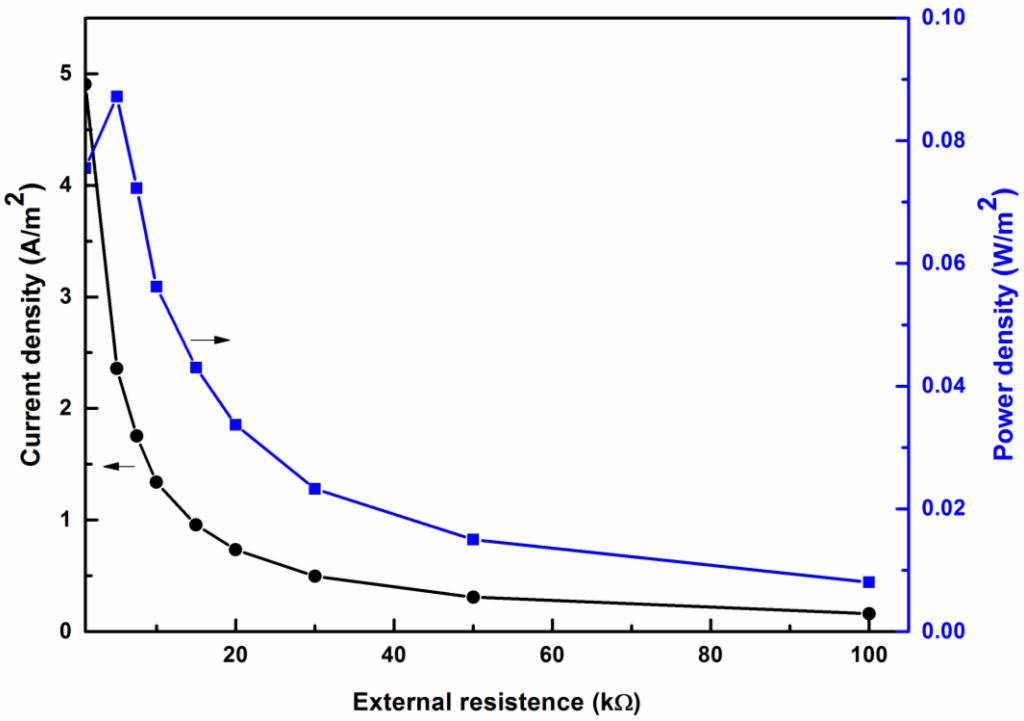

Figure 5.14 By mixing artificial seawater (0.5 M NaCl) and river water (0.01 M NaCl), the generated power can be output and supply an electric load.

The generated power density 0.087 W/m^2 is lower than the results reported for heterogeneous membranes (carbon/alumina, engineered polymer polyphenylsulfone/GO) due to large pores inside the film that compromises the ion selectivity [312, 324]. Nevertheless, it's higher than the reported green energy (3.89 × 10^{-5} W/m^2) generated by a graphene/humic acid concentration cell [325]. It is not possible to make a comparison with the heterogeneous membranes with a layer of PPy coating [300, 301], since data of salinity power density was not available. It should be mentioned that this power was generated within the gradient of 0.01M/0.5M, a

concentration gradient similar to that of Cl^- (~20) in the body fluid. A power of 40 μW can be generated from this membrane in a size of 2 cm×2 cm, same as that reverse electrodialysis system used for drug delivery [63]. This power is also sufficient to drive the implantable medical devices with power requirement in the level of μW-mW, such as a pacemaker [2]. It clearly demonstrates that this membrane has the potential for biomimetic applications. Moreover, at this gradient of 0.01M/0.5M, this system could generate a potential of 37 mV, larger than some bioelectric signals such as an electromyogram (less than 10 mV) [326].

Similar to the electric eel whose electric organ consists of stacks of electrocytes linked in series and parallels [327], the generated power density from this PPy membrane may be enhanced by assembling single cells in series. The stacked PPy membranes build up voltage and the working area is enlarged to promote the total ionic flux [327]. It has been demonstrated by Taek Dong Chung *et al.* that by using increased pairs of the ion exchange membrane, the voltage is enhanced and the reverse electrodialysis system successfully facilitate the transdermal penetration of ionic drug *in vitro* and *in vivo* [63]. Improvement may also be achieved by using a heterogeneous membrane by combining a negatively charged membrane such as graphene oxide (GO) to realize a rectification effect for regulating ion flux.

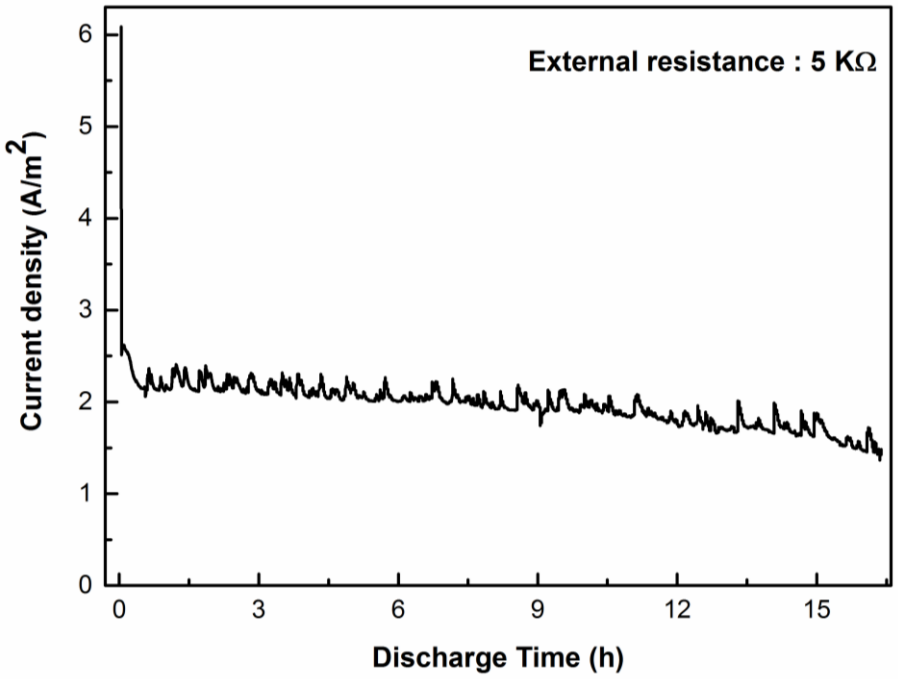

Figure 5.15 Current density of the PPy devices recorded during a monitoring time of 16 hours. By mixing of artificial seawater (0.5 M NaCl) and river water (0.01 M NaCl), the device can generate an energy density of 1.4 Wh m^{-2}.

5.3.3 Electrochemical properties of PPy membrane

The electrochemical oxidation and reduction of PPy involves both electron and ion-exchange processes [328]. In a PBS electrolyte with a matching ion concentration of body fluid, this membrane demonstrated an anodic peak at 0.5 V and cathodic peak -0.25 V (Figure 5.16), which is primarily due to ion transporting through the polymer to compensate the charges on the PPy backbone [329]. These results clearly demonstrate that the ion transport of PPy can be governed by its redox state.

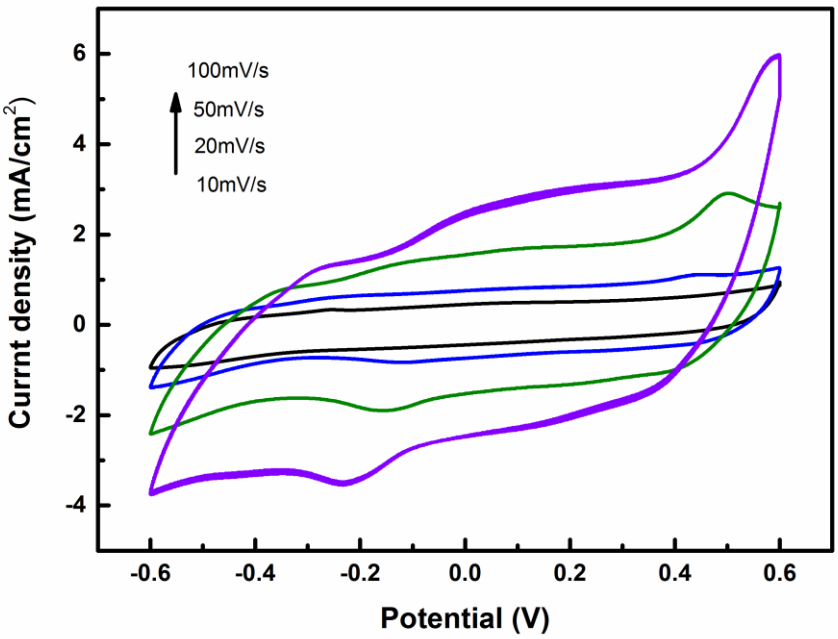

Figure 5.16 Cyclic voltammograms of a PPy membrane in a PBS solution at different scan rates of 10mV/s, 20 mV/s, 50 mV/s and 100 mV/s.

The impedance plot of a PPy membrane is shown in Figure 5.17, where the intercept at the real impedance (Z') axis was 7.9 Ω, which was lower than the 12 Ω reported for a free-standing PPy membrane prepared by electropolymerization, thus evidencing a high ionic conductivity of our membrane [319].

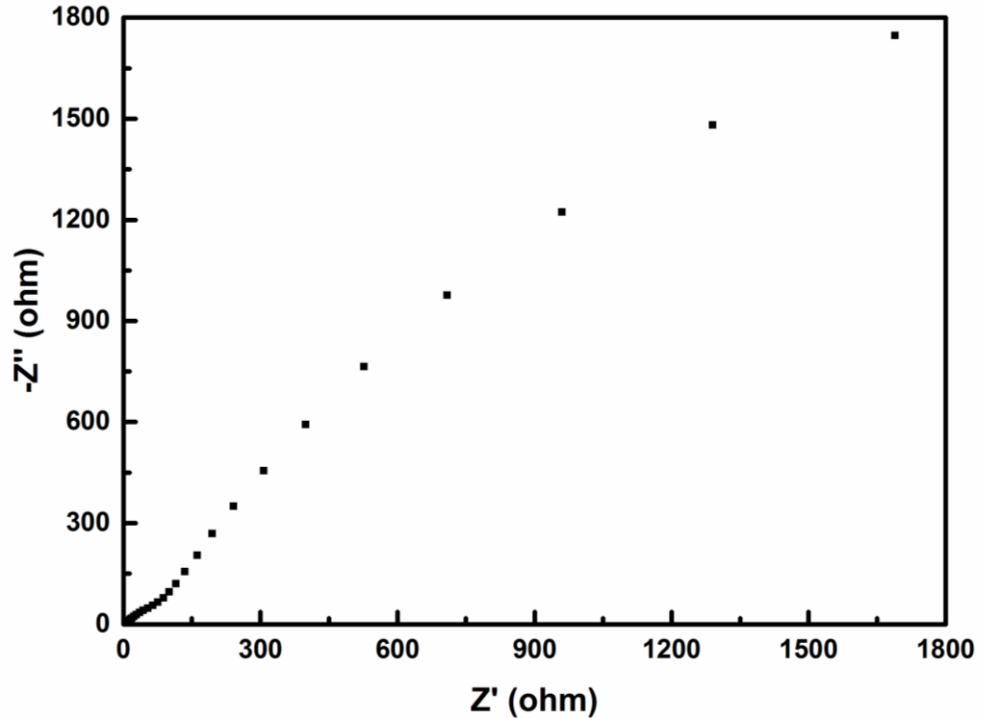

Figure 5.17 Nyquist plot of a PPy membrane in a PBS solution.

The ion conductance of this PPy membrane at its reduced or oxidised state was investigated. A potential from -0.5 to -1 V to trigger the reduction was applied, and 0.1- 0.5 V to trigger the oxidation. The ionic conductance (slope of the *I-V* curve) increased with the applied transmembrane potential in 1 mM KCl solution (Figure 5.18A and 5.18B). This ion concentration is of the same order of magnitude as the extracellular fluid (4 mM K^+) [330].

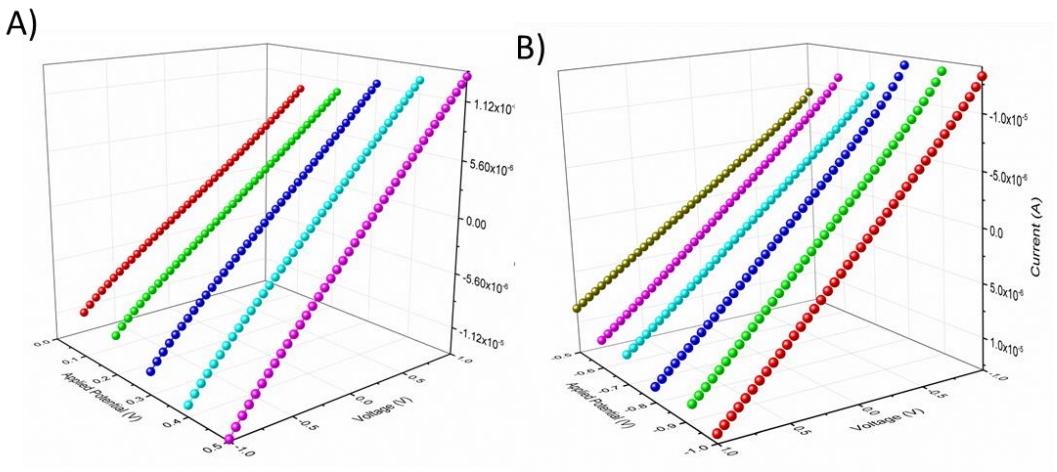

Figure 5.18 (A) Current-voltage response of the oxidised PPy membrane at different potentials (0.1 V, 0.2 V, 0.3 V, 0.4 V and 0.5 V) in 1 mM KCl solution, oxidation time was 300s. (B) Current-voltage response of the reduced PPy membrane at different potentials (-0.5 V, -0.6 V, -0.7 V, -0.8 V, -0.9 V and -1.0 V) in 1 mM KCl solution; reduction time was 300s.

When an oxidation potential of 0.5 V was applied, –NH– amine groups on the PPy chain was oxidised to N^+ as evidenced by the increased N^+/(–NH–) ratio from 0.14 to 0.17 (XPS spectra, Figure 5.19A). With an increase in oxidising potential or reducing potential, more ions are transported across the film, resulting in a higher streaming current [331]. The ionic conductance increased with the oxidation time (Figure 4.19B), owing to the increased number of defects in the π-electron system that regulates the anions ingress to the oxidised sites [298]. The ionic conductance of oxidised PPy (0.5 V) was 1.3×10^{-5} S, higher than that 8.6×10^{-6} S at the reduced state (-0.5 V). A better ion transport in the oxidised PPy can be due to the tight packing of PPy at its oxidized state resulting in better ion selectivity [331]. Such tunable ionic conductance proves that this PPy membrane can be used as a smart electro-modulated membrane.

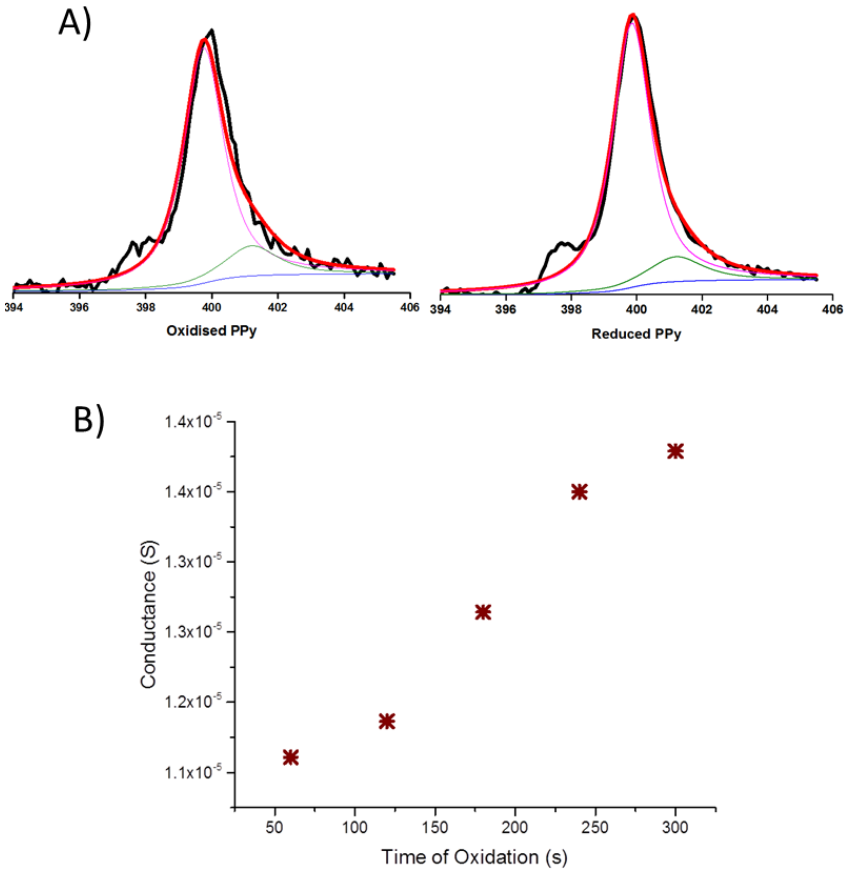

Figure 5.19 (A) XPS N 1s spectra of oxidised PPy (left) and reduced PPy (right) with –NH– (399.8 eV) and the positively charged nitrogen N^+ (401.2 eV). (B) Ionic conductance of the PPy membrane at 0.5 V as a function of oxidation time (60 to 300 s) in 1 mM KCl solution.

5.3.4 Cytocompatibility of PPy membrane

Smart biological devices that are interactive, programmable, and capable of seamless communication with surrounding tissues are highly desirable to evoke cell response [189]. The materials for use should be biocompatible or at least non-toxic. The cytocompatibility of PPy membrane was evaluated using human adipose-derived stem cells (hADSCs). As shown in the live/dead fluorescence staining (Figure 5.20A-C),

hADSCs were well spread and reached high confluence at day 14 after seeding, showing the cytocompatibility of this film. In agreement with the fluorescence image, a flat, well spread cell morphology with filopodia attached tightly to the PPy granules; these cells also formed bridges over this highly porous substrate (Figure 5.20D). The total cell metabolic activity, characteristic of cell proliferation, increased significantly during the first 2 weeks, then stabilised (Figure 5.20E). These results demonstrate that this porous PPy membrane can well support adhesion and proliferation of hADSCs.

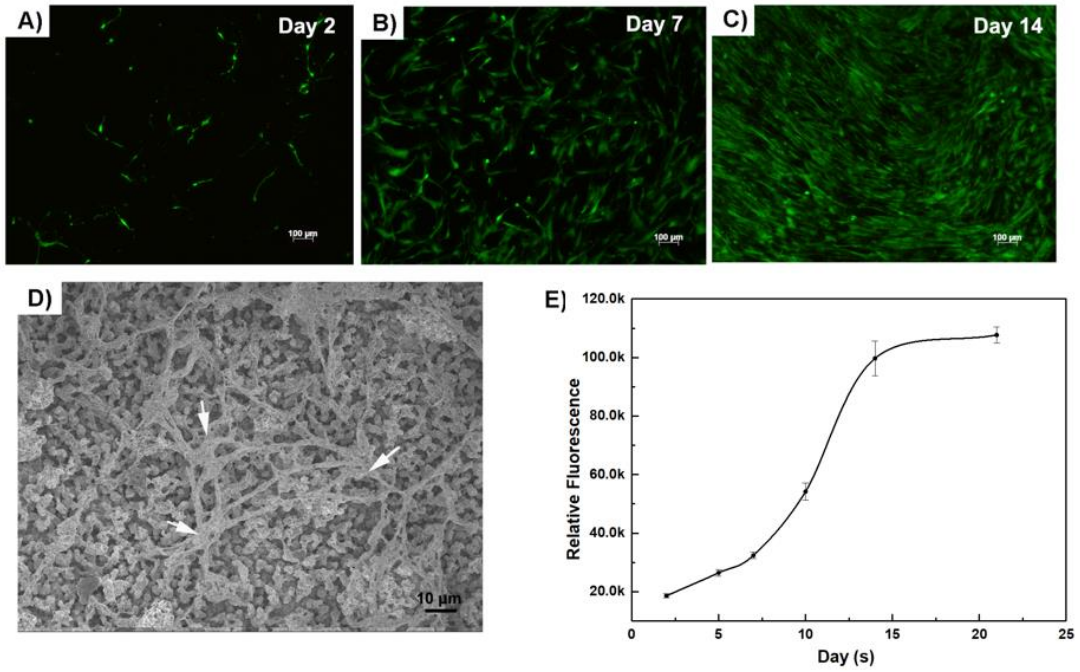

Figure 5.20 Cytocompatibility of the PPy membrane: Fluorescence micrographs of hADSCs on a PPy membrane at (A) day 2, (B) day 7 and (C) day 14. (D) SEM images of hADSCs (indicated by the arrows) on a PPy membrane at day 7; (E) Growth curve of hADSCs on a PPy membrane during a 21 days' time period.

5.4 Conclusions

In summary, a smart PPy membrane with an asymmetric structure has been developed via a self-assembly process. It demonstrates different wettability: hydrophobicity on

the PPy-aqueous surface and hydrophilicity on the PPy-oil surface; which can be ascribed to the asymmetric geometrical microstructure at these two faces. Its electrochemically tunable ionic conductance is ascribed to its charged backbone that regulates the ingress/egress of ions onto the redox sites. This membrane has demonstrated the capability to convert a salinity gradient into a streaming ionic current and realise an energy conversion, which can be ascribed to the ion permselectivity and preferred ion transportation within the asymmetric structure. Moreover, this membrane is a good substrate for Adipose-derived stem cells adhesion and proliferation. It can be deduced that this single component PPy membrane provides a platform to imitate biological ion transport by utilizing its asymmetric structure, and harvest energy from the stream of body fluid. This work may provide one step further towards the development of "smart" membranes.

Chapter 6 Conclusions and outlooks

6.1 Conclusions

The work in this thesis work aims to develop cytocompatible conducting polymers materials for bio-related energy applications due to the increasing demand for wearable and miniaturised implantable medical devices (IMDs). Two types of materials have been engineered via facile approaches: Polypyrrole/Poly(3,4-ethylenedioxythiophene hydrogel (PPy/PEDOT hydrogel) and free-standing PPy membrane. Using these materials as one important component, a metal-air battery system and a salinity power generation system have been developed as power sources potentially for driving the IMDs.

PPy/PEDOT hydrogel is fabricated by a two-step crosslinking method and a subsequent electrochemical deposition technique. Its application for a Mg-air bioelectric battery system has been demonstrated (Chapter 3). This fabrication method is facile and effective which is capable of producing hydrogels with any desirable size and shape. Mechanical properties of this hydrogel can be tailored for different bio-interfaces application by controlling the charge consumed. With the inherent electroconductivity, this hydrogel can deliver electrical stimulation to the hADSCs and promote the cell differentiation. The Mg-air bioelectric battery assembled with this hybrid hydrogel cathode and a magnesium anode in aqueous electrolyte possesses high energy density. This type of bioelectric battery may be directly used to provide the electrical energy to modulate cellular activities (e.g. cell migration, proliferation, differentiation) without need of an external power supply.

Application of this PPy/PEDOT hydrogel is expanded for an Fe bioelectric battery by coupling with an Fe anode, a promising material for stent, in the culture media electrolyte. Apart from the battery function for providing electrical energy, this galvanic Fe-air battery improves the Fe degradation compared with its static corrosion without battery stimulation (Chapter 4). The oxygen reduction on the cathode imposes an additional electrochemical reaction on the Fe anode apart from its self-corrosion, resulting in enhanced Fe corrosion. This battery can well support the proliferation of hADSCs during a 21 days period. This Fe-air battery may provide a new dynamic strategy to solve the problem of low degradation rate of Fe stent.

This thesis further develops another type of energy source - a salinity gradient energy harvesting system using an asymmetric PPy membrane (Chapter 5). This PPy membrane is developed via an interfacial polymerization process. The formed membrane features an asymmetric structure, resulting in favourable ion transport from PPy-aqueous surface to PPy-oil surface with a tunable conductance attributed to the positively charged backbone of the PPy membrane. Its capability to convert salinity gradient into a streaming ionic current enable the realisation of the energy conversion. This membrane is cytocompatible and able to support the hADSCs adhesion and proliferation. Therefore, this PPy membrane may provide a platform to imitate biological ion transport by harvesting energy from the stream of body fluid for biological activities.

In summary, conducting polymer based materials developed in this thesis have demonstrated their promising applications in bio-related energy including metal-air battery and salinity power generation. These works may open a new avenue to develop bio-related energy generation.

6.2 Outlooks

The ultimate goal of the research on cytocompatible energy source is to realise *in vitro* or *in vivo* power supply for wearable and implantable medical devices. Energy densities derived from the developed energy devices (metal-air battery, salinity gradient power) in this thesis are still much lower than the currently used electrochemical batteries, hence they need to be further improved for practical applications.

For metal-air battery, elctrocatalytic activity of the cathode determines the battery performance. Nanostructured CPs with higher surface areas are expected to deliver high performance due to the short path lengths and easy access of ions transport [136]. In this regard, further work needs to focus on developing cytocompatible materials with such features by controlling the synthesis condition or introducing bio-macromolecules with functional groups enabling of hydrogen bond formation to regulate the growth process [136]. The electrocatalytic activity of CPs can also be enhanced with the incorporation of redox-active dopants due to the additional contribution and more favourable kinetics and electron transport environment [332]. Moreover, incorporation of biological dopants will increase the capability to regulate cell behaviours [333, 334].

For the salinity energy harvesting system, ionic permselectivity of the membrane is the key factor determining the efficiency of this energy conversion process. Higher ionic permselectivity, higher ability to discriminate ions with opposite charges [88]. It can be improved by applying a well-designed heterogeneity on membranes. Asymmetric membranes with opposite surface charge can exhibit an ionic diode behaviour, avoiding power dissipation due to the blocking of back current under

reverse bias and boosting the energy conversion [335]. It may be easily achieved by integrating a negatively charged component such as graphene oxide with this positively charged PPy membrane.

It should be pointed out that body fluid is not static and flowing across the body driven by hydrostatic pressure and osmosis [336]. The induced performance from this dynamic nature of *in vivo* conditions will be different from that of the static nature used in this work. To more precisely estimate the performance of these power sources for potential implantation, the condition of a simulated body fluid under the dynamic condition of normal physiological flow rate (2 ml/100 ml min^{-1}) is suggested [337].

Currently, there have been tremendous development and efforts into materials and energy source systems for IMDs to enhance the quality and efficacy of healthcare. It is reasonable to expect that this field will attract more attention from academics and industries to work together towards practical applications.

References

1. Y.-H. Joung, *Development of implantable medical devices: from an engineering perspective.* International Neurourology Journal, 2013. **17**(3): p. 98.
2. X. Wei, and J. Liu, *Power sources and electrical recharging strategies for implantable medical devices.* Frontiers of Energy and Power Engineering in China, 2008. **2**(1): p. 1-13.
3. A.B. Amar, , A.B. Kouki, and H. Cao, *Power approaches for implantable medical devices.* Sensors, 2015. **15**(11): p. 28889-28914.
4. W. Irnich, , *Electronic security systems and active implantable medical devices.* Pacing and Clinical Electrophysiology, 2002. **25**(8): p. 1235-1258.
5. N. Kakade, [cited 2019 24/01]; Available from: https://www.sganalytics.com/blog/winning-in-implantable-medical-devices-market-pharmas-next-frontier/.
6. Y. Han, C. Yu, and H. Liu, *A microbial fuel cell as power supply for implantable medical devices.* Biosensors and Bioelectronics, 2010. **25**(9): p. 2156-2160.
7. M. Rasouli, and L.S.J. Phee, *Energy sources and their development for application in medical devices.* Expert Review of Medical Devices, 2010. **7**(5): p. 693-709.
8. D.C. Bock, et al., *Batteries used to power implantable biomedical devices.* Electrochimica Acta, 2012. **84**: p. 155-164.
9. T. Denning, K. Fu, and T. Kohno. *Absence Makes the Heart Grow Fonder: New Directions for Implantable Medical Device Security*. in *HotSec*. 2008.
10. M. Mackin, , *Study Guide to Accompany Basics for Chemistry*. 2012: Elsevier.
11. M. Winter, and R.J. Brodd, *What Are Batteries, Fuel Cells, and Supercapacitors?* Chemical Reviews, 2004. **104**(10): p. 4245-4270.
12. C. de las Casas, and W. Li, *A review of application of carbon nanotubes for lithium ion battery anode material.* Journal of Power Sources, 2012. **208**: p. 74-85.
13. D.W.I.R.M. Hahn, , *Techniques for Raman Analysis of Lithium-Ion Batteries.* 2015.
14. K.Chen , et al., *Hybrid cathode lithium batteries for implantable medical applications.* Journal of Power Sources, 2006. **162**(2): p. 837-840.
15. W. Greatbatch, *The Making of the Pacemaker: Celebrating a Lifesaving Invention*. 2000: Prometheus Books.
16. T. Wacharasindhu, et al., *Radioisotope microbattery based on liquid semiconductor.* Applied Physics Letters, 2009. **95**(1): p. 014103.
17. G. Antonioli, et al., *Stinulatore cardiaco impiantabile con nuova battaria a stato solido al litio.* Minerva Med, 1973. **64**: p. 2298-2305.

18. R.J. Brodd, et al., *Batteries, 1977 to 2002.* Journal of the Electrochemical Society, 2004. **151**(3): p. K1-K11.

19. S. Stauss, and I. Honma, *Biocompatible batteries—Materials and chemistry, fabrication, applications, and future prospects.* Bulletin of the Chemical Society of Japan, 2018. **91**(3): p. 492-505.

20. A. Heller, , *Potentially implantable miniature batteries.* Analytical and Bioanalytical Chemistry, 2006. **385**(3): p. 469-473.

21. J. Rao, and G. Richter, *Implantable bio-electrochemical power sources.* Naturwissenschaften, 1974. **61**(5): p. 200-206.

22. A.C.C. Tseung, , B.Y.C. Wan, and W.J. King, *Electrochemical Cells*. 1975, Google Patents.

23. M. Schaldach, , *Bioelectric energy sources for cardiac pacing.* Annals of the New York Academy of Sciences, 1969. **167**(1): p. 1016-1024.

24. O. Roy, et al., *Biological energy sources.* Annals of the New York Academy of Sciences, 1969. **167**(1): p. 645-660.

25. R.D. Bentz, C.S. Pedicini, and W.J. Scott Jr, *Metal-air power supply and air-manager system, and metal-air cell for use therein*. 1994, Google Patents.

26. T. Zhang, Z. Tao, and J. Chen, *Magnesium–air batteries: from principle to application.* Materials Horizons, 2014. **1**(2): p. 196-206.

27. F. Cheng, and J. Chen, *Metal–air batteries: from oxygen reduction electrochemistry to cathode catalysts.* Chemical Society Reviews, 2012. **41**(6): p. 2172-2192.

28. F. Witte, et al., *Degradable biomaterials based on magnesium corrosion.* Current Opinion in Solid State and Materials Science, 2008. **12**(5): p. 63-72.

29. D. Pierson, et al., *A simplified in vivo approach for evaluating the bioabsorbable behavior of candidate stent materials.* Journal of Biomedical Materials Research Part B: Applied Biomaterials, 2012. **100**(1): p. 58-67.

30. A. Inoishi, et al., *Mg–air oxygen shuttle batteries using a ZrO 2-based oxide ion-conducting electrolyte.* Chemical Communications, 2013. **49**(41): p. 4691-4693.

31. G. Song, *Control of biodegradation of biocompatable magnesium alloys.* Corrosion Science, 2007. **49**(4): p. 1696-1701.

32. P.M. Harrison, and P. Arosio, *The ferritins: molecular properties, iron storage function and cellular regulation.* Biochimica et Biophysica Acta (BBA)-Bioenergetics, 1996. **1275**(3): p. 161-203.

33. K.F. Blurton, and A.F. Sammells, *Metal/air batteries: Their status and potential — a review.* Journal of Power Sources, 1979. **4**(4): p. 263-279.

34. R. Balasubramanian, et al., *Electrochemical characterization of magnesium/silver chloride battery.* Journal of Power Sources, 1995. **56**(2): p. 197-199.

35. M.G. Medeiros, and E.G. Dow, *Magnesium-solution phase catholyte seawater electrochemical system.* Journal of Power Sources, 1999. **80**(1): p. 78-82.

36. J.S. Lee, et al., *Metal–air batteries with high energy density: Li–air versus Zn–air.* Advanced Energy Materials, 2011. **1**(1): p. 34-50.

37. J.S. Spendelow and A. Wieckowski, *Electrocatalysis of oxygen reduction and small alcohol oxidation in alkaline media.* Physical Chemistry Chemical Physics, 2007. **9**(21): p. 2654-2675.

38. G. Fontenier, R. Freschard, and M. Mourot, *Study of a "platinum-magnesium" cell to supply current to a pacemaker.* Bioelectrochemistry and Bioenergetics, 1975. **2**(2): p. 106-123.

39. G. Fontenier, R. Freschard, and M. Mourot, *Design of Experimentation with a Platinum-Magnesium Bioelectric Battery.* Biomaterials, Medical Devices, and Artificial Organs, 1975. **3**(1): p. 25-45.

40. G. Fontenier, M. Mourot, and R. Freshard, *Long-term in vivo behavior of a platinum endoauricular-magnesium hybrid battery.* Medical Instrumentation, 1975. **9**(4): p. 171-176.

41. L. Liu, et al., *Nanoporous Pt− Co alloy nanowires: fabrication, characterization, and electrocatalytic properties.* Nano Letters, 2009. **9**(12): p. 4352-4358.

42. J. Zhang, et al., *Platinum monolayer on nonnoble metal− noble metal core− shell nanoparticle electrocatalysts for O2 reduction.* The Journal of Physical Chemistry B, 2005. **109**(48): p. 22701-22704.

43. B. Wang, *Recent development of non-platinum catalysts for oxygen reduction reaction.* Journal of Power Sources, 2005. **152**: p. 1-15.

44. Q. Zhou and G. Shi, *Conducting Polymer-Based Catalysts.* Journal of the American Chemical Society, 2016. **138**(9): p. 2868-2876.

45. V.G. Khomenko, V.Z. Barsukov, and A.S. Katashinskii, *The catalytic activity of conducting polymers toward oxygen reduction.* Electrochimica Acta, 2005. **50**(7): p. 1675-1683.

46. A. Golberg, H.D. Rabinowitch, and B. Rubinsky, *Galvanic apparent internal impedance: An intrinsic tissue property.* Biochemical and Biophysical Research Communications, 2009. **389**(1): p. 168-171.

47. P. Nadeau, et al., *Prolonged energy harvesting for ingestible devices.* Nature Biomedical Engineering, 2017. **1**(3): p. 0022.

48. H. Hafezi, et al., *An ingestible sensor for measuring medication adherence.* IEEE Transactions on Biomedical Engineering, 2015. **62**(1): p. 99-109.

49. X. Huang, et al., *A Fully Biodegradable Battery for Self-Powered Transient Implants.* Small, 2018: p. 1800994.

50. M. Tsang, et al., *Biodegradable magnesium/iron batteries with polycaprolactone encapsulation: A microfabricated power source for transient implantable devices.* Microsystems & Nanoengineering, 2015. **1**: p. 15024.

51. I.M. Mosa, et al., *Ultrathin Graphene–Protein Supercapacitors for Miniaturized Bioelectronics.* Advanced Energy Materials, 2017. **7**(17): p. 1700358.

52. Y.K. Tan, and S.K. Panda, *Review of energy harvesting technologies for sustainable WSN*, in *Sustainable wireless sensor networks*. 2010, InTech.

53. L. Halámková, et al., *Implanted biofuel cell operating in a living snail.* Journal of the American Chemical Society, 2012. **134**(11): p. 5040-5043.

54. Z.L. Wang, *Triboelectric nanogenerators as new energy technology for self-powered systems and as active mechanical and chemical sensors.* ACS Nano, 2013. **7**(11): p. 9533-9557.

55. C. Dagdeviren, et al., *Conformal piezoelectric energy harvesting and storage from motions of the heart, lung, and diaphragm.* Proceedings of the National Academy of Sciences, 2014. **111**(5): p. 1927-1932.

56. M. Amin Karami and D.J. Inman, *Powering pacemakers from heartbeat vibrations using linear and nonlinear energy harvesters.* Applied Physics Letters, 2012. **100**(4): p. 042901.

57. P.D. Mitcheson, et al., *Energy harvesting from human and machine motion for wireless electronic devices.* Proceedings of the IEEE, 2008. **96**(9): p. 1457-1486.

58. J. Paulo and P. Gaspar. *Review and future trend of energy harvesting methods for portable medical devices*. in *Proceedings of the world congress on engineering*. 2010.2:p. 168-196.

59. D.M. Rowe, *Conversion Efficiency and Figure-of-Merit*, in *CRC Handbook of Thermoelectrics*. 1995, CRC press. p. 31-37.

60. O. Korostynska, *Energy harvesting technologies.* Sensor Review, 2011. **31**(1), https://doi.org/10.1108/sr.2011.08731aae.001.

61. Tang, W., et al., *Implantable Self-Powered Low-Level Laser Cure System for Mouse Embryonic Osteoblasts' Proliferation and Differentiation.* ACS Nano, 2015. **9**(8): p. 7867-7873.

62. Z.L. Wang, J. Chen, and L. Lin, *Progress in triboelectric nanogenerators as a new energy technology and self-powered sensors.* Energy & Environmental Science, 2015. **8**(8): p. 2250-2282.

63. S.R. Kwon, et al., *Electrodeless Reverse Electrodialysis Patches as an Ionic Power Source for Active Transdermal Drug Delivery.* Advanced Functional Materials, 2018. **28**(15): p. 1705952.

64. F. Yin, et al., *Effects of low salinity on antioxidant enzymes activities in kidney and muscle of juvenile silver pomfret Pampus argenteus.* Acta Ecologica Sinica, 2011. **31**(1): p. 55-60.

65. M. Altamirano, *Electrical properties of the innervated membrane of the electroplax of electric eel.* Journal of Cellular and Comparative Physiology, 1955. **46**(2): p. 249-277.

66. C.d.S. Mermelstein, M.L. Costa, and V. Moura Neto, *The cytoskeleton of the electric tissue of Electrophorus electricus, L.* Anais Da Academia Brasileira De Ciencias, 2000. **72**(3): p. 341-351.

67. A.L. Gotter, M.A. Kaetzel, and J.R. Dedman, *Electrophorus electricus as a Model System for the Study of Membrane Excitability.* Comparative

Biochemistry and Physiology Part A: Molecular & Integrative Physiology, 1998. **119**(1): p. 225-241.

68. J. Xu and D.A. Lavan, *Designing artificial cells to harness the biological ion concentration gradient.* Nature Nanotechnology, 2008. **3**(11): p. 666.

69. J. Feng, et al., *Single-layer MoS 2 nanopores as nanopower generators.* Nature, 2016. **536**(7615): p. 197.

70. G.Z. Ramon, B.J. Feinberg, and E.M. Hoek, *Membrane-based production of salinity-gradient power.* Energy &Environmental Science, 2011. **4**(11): p. 4423-4434.

71. F.H. van der Heyden, D. Stein, and C. Dekker, *Streaming currents in a single nanofluidic channel.* Physical Review Letters, 2005. **95**(11): p. 116104.

72. D.A. Vermaas, M. Saakes, and K. Nijmeijer, *Doubled power density from salinity gradients at reduced intermembrane distance.* Environmental Science & Technology, 2011. **45**(16): p. 7089-7095.

73. I. Statistics, *Key world energy statistics 2017.* International Energy Agency, 2017.

74. F. Helfer, C. Lemckert, and Y.G. Anissimov, *Osmotic power with Pressure Retarded Osmosis: Theory, performance and trends – A review.* Journal of Membrane Science, 2014. **453**: p. 337-358.

75. I.L. Alsvik M.-B. Hägg, *Pressure retarded osmosis and forward osmosis membranes: materials and methods.* Polymers, 2013. **5**(1): p. 303-327.

76. J.W. Post, et al., *Salinity-gradient power: Evaluation of pressure-retarded osmosis and reverse electrodialysis.* Journal of Membrane Science, 2007. **288**(1): p. 218-230.

77. K. Lee, R. Baker, and H. Lonsdale, *Membranes for power generation by pressure-retarded osmosis.* Journal of Membrane Science, 1981. **8**(2): p. 141-171.

78. B.B. Sales, et al., *Direct Power Production from a Water Salinity Difference in a Membrane-Modified Supercapacitor Flow Cell.* Environmental Science & Technology, 2010. **44**(14): p. 5661-5665.

79. R.A. Rica, et al., *Capacitive mixing for harvesting the free energy of solutions at different concentrations.* Entropy, 2013. **15**(4): p. 1388-1407.

80. F. La Mantia, D. Brogioli, and M. Pasta, *6 - Capacitive mixing and mixing entropy battery*, in *Sustainable Energy from Salinity Gradients*, A. Cipollina and G. Micale, Editors. 2016, Woodhead Publishing. p. 181-218.

81. M. Marino, et al., *Modification of the surface of activated carbon electrodes for capacitive mixing energy extraction from salinity differences.* Journal of Colloid and Interface Science, 2014. **436**: p. 146-153.

82. D. Brogioli, et al., *Capacitive mixing for the extraction of energy from salinity differences: Survey of experimental results and electrochemical models.* Journal of Colloid and Interface Science, 2013. **407**: p. 457-466.

83. M.C. Hatzell, R.D. Cusick, and B.E. Logan, *Capacitive mixing power production from salinity gradient energy enhanced through exoelectrogen-*

generated ionic currents. Energy & Environmental Science, 2014. **7**(3): p. 1159-1165.

84. R. Lacey, *Energy by reverse electrodialysis.* Ocean Engineering, 1980. **7**: p. 1-47.

85. S. Pawlowski, et al., *Improved fluid mixing and power density in reverse electrodialysis stacks with chevron-profiled membranes.* Journal of Membrane Science, 2017. **531**: p. 111-121.

86. J.G. Hong and Y. Chen, *Nanocomposite reverse electrodialysis (RED) ion-exchange membranes for salinity gradient power generation.* Journal of Membrane Science, 2014. **460**: p. 139-147.

87. J.N. Weinstein and F.B. Leitz, *Electric power from differences in salinity: the dialytic battery.* Science, 1976. **191**(4227): p. 557-559.

88. P. Długołęcki, et al., *Current status of ion exchange membranes for power generation from salinity gradients.* Journal of Membrane Science, 2008. **319**(1): p. 214-222.

89. E. Güler, et al., *Performance-determining membrane properties in reverse electrodialysis.* Journal of Membrane Science, 2013. **446**: p. 266-276.

90. C. Dekker, *Solid-state nanopores.* Nature Nanotechnology, 2007. **2**(4): p. 209-215.

91. Y. Mei and C.Y. Tang, *Recent developments and future perspectives of reverse electrodialysis technology: A review.* Desalination, 2018. **425**: p. 156-174.

92. J. Ji, et al., *Osmotic power generation with positively and negatively charged 2D nanofluidic membrane pairs.* Advanced Functional Materials, 2017. **27**(2): p. 1603623.

93. I. Vlassiouk and Z.S. Siwy, *Nanofluidic diode.* Nano Letters, 2007. **7**(3): p. 552-556.

94. H.C. Yang, et al., *Janus Membranes: Creating Asymmetry for Energy Efficiency.* Advanced Materials, 2018(30): p. 1801495.

95. Z. Zhang, et al., *Ultrathin and Ion-Selective Janus Membranes for High-Performance Osmotic Energy Conversion.* Journal of the American Chemical Society, 2017. **139**(26): p. 8905-8914.

96. L. Cao, et al., *Towards understanding the nanofluidic reverse electrodialysis system: well matched charge selectivity and ionic composition.* Energy & Environmental Science, 2011. **4**(6): p. 2259-2266.

97. B. Yameen, et al., *Single conical nanopores displaying pH-tunable rectifying characteristics. Manipulating ionic transport with zwitterionic polymer brushes.* Journal of the American Chemical Society, 2009. **131**(6): p. 2070-2071.

98. W. Guo, et al., *Current Rectification in Temperature-Responsive Single Nanopores.* ChemPhysChem, 2010. **11**(4): p. 859-864.

99. A. Koçer, et al., *A light-actuated nanovalve derived from a channel protein.* Science, 2005. **309**(5735): p. 755-758.

100. Z.S. Siwy, and S. Howorka, *Engineered voltage-responsive nanopores.* Chemical Society Reviews, 2010. **39**(3): p. 1115-1132.

101. S.B. Lee, et al., *Antibody-based bio-nanotube membranes for enantiomeric drug separations.* Science, 2002. **296**(5576): p. 2198-2200.

102. A.L. Sisson, et al., *Synthetic ion channels and pores (2004–2005).* Chemical Society Reviews, 2006. **35**(12): p. 1269-1286.

103. B. Zhang, Y. Zhang, and H.S. White, *The nanopore electrode.* Analytical Chemistry, 2004. **76**(21): p. 6229-6238.

104. X. Hou, W. Guo, and L. Jiang, *Biomimetic smart nanopores and nanochannels.* Chemical Society Reviews, 2011. **40**(5): p. 2385-2401.

105. D.o. Biology and M.U.o. Newfoundland, *Principles of Cell Biology (BIOL2060)*,2016.

106. N. Sperelakis, *Chapter 9 - Origin of Resting Membrane Potentials*, in *Cell Physiology Source Book (Fourth Edition)*, N. Sperelakis, Editor. 2012, Academic Press: San Diego. p. 121-145.

107. T.B. Schroeder, et al., *An electric-eel-inspired soft power source from stacked hydrogels.* Nature, 2017. **552**(7684): p. 214.

108. R. Waltman and J. Bargon, *Electrically conducting polymers: a review of the electropolymerization reaction, of the effects of chemical structure on polymer film properties, and of applications towards technology.* Canadian Journal of Chemistry, 1986. **64**(1): p. 76-95.

109. T. Otero, J. Martinez, and J. Arias-Pardilla, *Biomimetic electrochemistry from conducting polymers. A review: artificial muscles, smart membranes, smart drug delivery and computer/neuron interfaces.* Electrochimica Acta, 2012. **84**: p. 112-128.

110. M.R. Abidian, M.R., et al., *Hybrid conducting polymer–hydrogel conduits for axonal growth and neural tissue engineering.* Advanced Healthcare Materials, 2012. **1**(6): p. 762-767.

111. A. Ramanavičius, A., A. Ramanavičienė, and A. Malinauskas, *Electrochemical sensors based on conducting polymer—polypyrrole.* Electrochimica Acta, 2006. **51**(27): p. 6025-6037.

112. A. Malinauskas, *Electrocatalysis at conducting polymers.* Synthetic Metals, 1999. **107**(2): p. 75-83.

113. L. Pan, et al., *Conducting polymer nanostructures: template synthesis and applications in energy storage.* International Journal of Molecular Sciences, 2010. **11**(7): p. 2636-2657.

114. F.D.R. Amado, et al., *Synthesis and characterisation of high impact polystyrene/polyaniline composite membranes for electrodialysis.* Journal of Membrane Science, 2004. **234**(1): p. 139-145.

115. M. Karthikeyan, K.K.S. Kumar, and K.P. Elango, *Batch sorption studies on the removal of fluoride ions from water using eco-friendly conducting polymer/bio-polymer composites.* Desalination, 2011. **267**(1): p. 49-56.

116. T. Sata, T. Funakoshi, and K. Akai, *Preparation and transport properties of composite membranes composed of cation exchange membranes and polypyrrole.* Macromolecules, 1996. **29**(11): p. 4029-4035.

117. N.K. Guimard, N. Gomez, and C.E. Schmidt, *Conducting polymers in biomedical engineering.* Progress in Polymer Science, 2007. **32**(8): p. 876-921.

118. C.K. Chiang, et al., *Electrical conductivity in doped polyacetylene.* Physical Review Letters, 1977. **39**(17): p. 1098.

119. S. Machida, S. Miyata, and A. Techagumpuch, *Chemical synthesis of highly electrically conductive polypyrrole.* Synthetic Metals, 1989. **31**(3): p. 311-318.

120. A.F. Diaz, et al., *Electrochemistry of conducting polypyrrole films.* Journal of Electroanalytical Chemistry and Interfacial Electrochemistry, 1981. **129**(1): p. 115-132.

121. A. Diaz, and B. Hall, *Mechanical properties of electrochemically prepared polypyrrole films.* Ibm Journal of Research and Development, 1983. **27**(4): p. 342-347.

122. N. Oyama, et al., *Dimercaptan–polyaniline composite electrodes for lithium batteries with high energy density.* 1995. **373**(6515), p. 598.

123. N. Mermilliod, J. Tanguy, and F. Petiot, *A study of chemically synthesized polypyrrole as electrode material for battery applications.* Journal of the Electrochemical Society, 1986. **133**(6): p. 1073-1079.

124. R. Liu, S.I. Cho, and S.B. Lee, *Poly (3, 4-ethylenedioxythiophene) nanotubes as electrode materials for a high-powered supercapacitor.* Nanotechnology, 2008. **19**(21): p. 215710.

125. G. Wang, L. Zhang, and J. Zhang, *A review of electrode materials for electrochemical supercapacitors.* Chemical Society Reviews, 2012. **41**(2): p. 797-828.

126. G.G. Wallace, et al., *Conductive electroactive polymers: intelligent polymer systems*. 2008: CRC press.

127. S. Sadki, et al., *The mechanisms of pyrrole electropolymerization.* Chemical Society Reviews, 2000. **29**(5): p. 283-293.

128. T.y.V. Vernitskaya and O.N. Efimov, *Polypyrrole: a conducting polymer; its synthesis, properties and applications.* Russian Chemical Reviews, 1997. **66**(5): p. 443-457.

129. A. Malinauskas, J. Malinauskiene, and A. Ramanavičius, *Conducting polymer-based nanostructurized materials: electrochemical aspects.* Nanotechnology, 2005. **16**(10): p. R51.

130. W.-S. Huang, B.D. Humphrey, and A.G. MacDiarmid, *Polyaniline, a novel conducting polymer. Morphology and chemistry of its oxidation and reduction in aqueous electrolytes.* Journal of the Chemical Society, Faraday Transactions 1: Physical Chemistry in Condensed Phases, 1986. **82**(8): p. 2385-2400.

131. A.G. MacDiarmid and A.J. Epstein, *Polyanilines: a novel class of conducting polymers.* Faraday Discussions of the Chemical Society, 1989. **88**: p. 317-332.

132. A. Malinauskas, *Chemical deposition of conducting polymers.* Polymer, 2001. **42**(9): p. 3957-3972.

133. N. Toshima and S. Hara, *Direct synthesis of conducting polymers from simple monomers.* Progress in Polymer Science, 1995. **20**(1): p. 155-183.

134. C.M. Boutry, I. Gerber-Hörler, and C. Hierold, *Electrically conducting biodegradable polymer composites (polylactide-polypyrrole and polycaprolactone-polypyrrole) for passive resonant circuits.* Polymer Engineering & Science, 2013. **53**(6): p. 1196-1208.

135. D.N. Nguyen and H. Yoon, *Recent advances in nanostructured conducting polymers: from synthesis to practical applications.* Polymers, 2016. **8**(4): p. 118.

136. C. Li, H. Bai, and G. Shi, *Conducting polymer nanomaterials: electrosynthesis and applications.* Chemical Society Reviews, 2009. **38**(8): p. 2397-2409.

137. X. Zhang and S.K. Manohar, *Bulk synthesis of polypyrrole nanofibers by a seeding approach.* Journal of the American Chemical Society, 2004. **126**(40): p. 12714-12715.

138. K. Jurewicz, et al., *Supercapacitors from nanotubes/polypyrrole composites.* Chemical Physics Letters, 2001. **347**(1-3): p. 36-40.

139. Y. Yang, J. Liu, and M. Wan, *Self-assembled conducting polypyrrole micro/nanotubes.* Nanotechnology, 2002. **13**(6): p. 771.

140. K. Ramanathan, et al., *Bioaffinity sensing using biologically functionalized conducting-polymer nanowire.* Journal of the American Chemical Society, 2005. **127**(2): p. 496-497.

141. Y.-Y. Horng, et al., *Direct-growth of polyaniline nanowires for enzyme-immobilization and glucose detection.* Electrochemistry Communications, 2009. **11**(4): p. 850-853.

142. M. Wei, and Y. Lu, *Templating fabrication of polypyrrole nanorods/nanofibers.* Synthetic Metals, 2009. **159**(11): p. 1061-1066.

143. J.M. Pringle, et al., *Conducting polymer nanoparticles synthesized in an ionic liquid by chemical polymerisation.* Synthetic Metals, 2006. **156**(14-15): p. 979-983.

144. J. Huang, et al., *Polyaniline nanofibers: facile synthesis and chemical sensors.* Journal of the American Chemical Society, 2003. **125**(2): p. 314-315.

145. Y.-Z. Long, et al., *Recent advances in synthesis, physical properties and applications of conducting polymer nanotubes and nanofibers.* Progress in Polymer Science, 2011. **36**(10): p. 1415-1442.

146. L. Xia, Z. Wei, and M. Wan, *Conducting polymer nanostructures and their application in biosensors.* Journal of Colloid and Interface Science, 2010. **341**(1): p. 1-11.

147. A. de Leon and R.C. Advincula, *Chapter 11 - Conducting Polymers with Superhydrophobic Effects as Anticorrosion Coating*, in *Intelligent Coatings for Corrosion Control*, A. Tiwari, J. Rawlins, and L.H. Hihara, Editors. 2015, Butterworth-Heinemann: Boston. p. 409-430.

148. A.D.W. Carswell, E.A. O'Rea, and B.P. Grady, *Adsorbed Surfactants as Templates for the Synthesis of Morphologically Controlled Polyaniline and Polypyrrole Nanostructures on Flat Surfaces: From Spheres to Wires to Flat Films.* Journal of the American Chemical Society, 2003. **125**(48): p. 14793-14800.

149. L. Warren, et al., *A study of conducting polymer morphology the effect of dopant anions upon order.* Journal of the Electrochemical Society, 1989. **136**(8): p. 2286-2295.

150. V.P. Menon, J. Lei, and C.R. Martin, *Investigation of molecular and supermolecular structure in template-synthesized polypyrrole tubules and fibrils.* Chemistry of Materials, 1996. **8**(9): p. 2382-2390.

151. S.M. Richardson-Burns, et al., *Polymerization of the conducting polymer poly(3,4-ethylenedioxythiophene) (PEDOT) around living neural cells.* Biomaterials, 2007. **28**(8): p. 1539-1552.

152. H. Stubb, E. Punkka, and J. Paloheimo, *Electronic and optical properties of conducting polymer thin films.* Materials Science Reports, 1993. **10**(3): p. 85-140.

153. A.G. MacDiarmid, *"Synthetic metals": A novel role for organic polymers (Nobel Lecture).* Angew. Chem., Int. Ed., 2001. **40**(14): p. 2581-2590.

154. K.K Kanazawa, A.F. Diaz, et al., *Polypyrrole: An electrochemically synthesized conducting organic polymer.* Synthetic Metals, 1980. **1**(3): p. 329-336.

155. M.H. Harun, et al., *Conjugated conducting polymers: A brief overview.* UCSI Academic Journal: Journal for the Advancement of Science & Arts, 2007. **2**: p. 63-68.

156. T.-H. Le, Y. Kim, and H. Yoon, *Electrical and electrochemical properties of conducting polymers.* Polymers, 2017. **9**(4): p. 150.

157. R. Balint, N.J. Cassidy, and S.H. Cartmell, *Conductive polymers: Towards a smart biomaterial for tissue engineering.* Acta Biomaterialia, 2014. **10**(6): p. 2341-2353.

158. J.L. Bredas and G.B. Street, *Polarons, bipolarons, and solitons in conducting polymers.* Accounts of Chemical Research, 1985. **18**(10): p. 309-315.

159. N.K. Guimard, J.L. Sessler, and C.E. Schmidt, *Design of a novel electrically conducting biocompatible polymer with degradable linkages for biomedical applications.* MRS Online Proceedings Library Archive, 2006. **950**.

160. G. Tourillon, *Polythiophene and its derivatives.* Handbook of conducting polymers, 1986. **1**: p. 293.

161. K. Kaneto, K. Yoshino, and Y. Inuishi, *Electrical and optical properties of polythiophene prepared by electrochemical polymerization.* Solid State Communications, 1983. **46**(5): p. 389-391.

162. H. Yoon and J. Jang, *Conducting-polymer nanomaterials for high-performance sensor applications: issues and challenges.* Advanced Functional Materials, 2009. **19**(10): p. 1567-1576.

163. M. Trojanowicz, *Application of conducting polymers in chemical analysis.* Microchimica Acta, 2003. **143**(2-3): p. 75-91.

164. B. Winther-Jensen, et al., *High rates of oxygen reduction over a vapor phase–polymerized PEDOT electrode.* Science, 2008. **321**(5889): p. 671-674.

165. J. Roncali, *Conjugated poly (thiophenes): synthesis, functionalization, and applications.* Chemical Reviews, 1992. **92**(4): p. 711-738.

166. A.T. Lawal, and G.G. Wallace, *Vapour phase polymerisation of conducting and non-conducting polymers: A review.* Talanta, 2014. 119: p. 133-143.

167. X. Gao, et al., *Bifunctional 3D n-doped porous carbon materials derived from paper towel for oxygen reduction reaction and supercapacitor.* Science Bulletin, 2018. **63**(10): p. 621-628.

168. J. Bobacka, *Conducting polymer-based solid-state ion-selective electrodes.* Electroanalysis: An International Journal Devoted to Fundamental and Practical Aspects of Electroanalysis, 2006. **18**(1): p. 7-18.

169. M.J. Ariza and T.F. Otero, *Ionic diffusion across oxidized polypyrrole membranes and during oxidation of the free-standing film.* Colloids and Surfaces A: Physicochemical and Engineering Aspects, 2005. **270**: p. 226-231.

170. X. Zhang and R. Bai, *Surface electric properties of polypyrrole in aqueous solutions.* Langmuir, 2003. **19**(26): p. 10703-10709.

171. P. Burgmayer and R.W. Murray, *An ion gate membrane: electrochemical control of ion permeability through a membrane with an embedded electrode.* Journal of the American Chemical Society, 1982. **104**(22): p. 6139-6140.

172. G. Gohil, V. Binsu, and V.K. Shahi, *Preparation and characterization of mono-valent ion selective polypyrrole composite ion-exchange membranes.* Journal of Membrane Science, 2006. **280**(1-2): p. 210-218.

173. P. Burgmayer and R.W. Murray, *Ion gate electrodes. Polypyrrole as a switchable ion conductor membrane.* The Journal of Physical Chemistry, 1984. **88**(12): p. 2515-2521.

174. M.N. Akieh, et al., *Electrochemically controlled ion transport across polypyrrole/multi-walled carbon nanotube composite membranes*. Synthetic Metals, 2011. 161(17): p. 1906-1914.

175. M.N. Akieh, et al., *Electrochemically controlled ion transport across polypyrrole/multi-walled carbon nanotube composite membranes.* Synthetic Metals, 2011. **161**(17): p. 1906-1914.

176. B. Bao, et al., *3D Porous Hydrogel/Conducting Polymer Heterogeneous Membranes with Electro-/pH-Modulated Ionic Rectification.* Advanced Materials, 2017. **29**(44): p. 1702926.

177. Q. Zhang, et al., *The synthesis and characterization of a novel biodegradable and electroactive polyphosphazene for nerve regeneration.* Materials Science and Engineering: C, 2010. **30**(1): p. 160-166.

178. S.A. Hillyard, et al., *Electrical signs of selective attention in human brain.* Science, 1973. **182**(4108): p. 177-180.

179. X. Gu, et al., *Low-Frequency Electrical Stimulation Induces the Proliferation and Differentiation of Peripheral Blood Stem Cells Into Schwann Cells.* American Journal of the Medical Sciences, 2015. **349**(2): p. 157-161.

180. H.-S. Hou, et al., *Simultaneous chemical and electrical stimulation on lung cancer cells using a multichannel-dual-electric-field chip.* Biomicrofluidics, 2014. **8**(5), p: 052007.

181. R.F. Valentini, et al., *Electrically charged polymeric substrates enhance nerve fibre outgrowth in vitro.* Biomaterials, 1992. **13**(3): p. 183-190.

182. J. Black, *Electrical stimulation.* Its role in growth, repair, and remodeling of the musculoskeletal system. Praeger, New York, 1987.

183. P. Aebischer, et al., *Piezoelectric guidance channels enhance regeneration in the mouse sciatic nerve after axotomy.* Brain Research, 1987. **436**(1): p. 165-168.

184. A. Kotwal and C.E. Schmidt, *Electrical stimulation alters protein adsorption and nerve cell interactions with electrically conducting biomaterials.* Biomaterials, 2001. **22**(10): p. 1055-1064.

185. C.T. Brighton, et al., *Signal transduction in electrically stimulated bone cells.* The Journal of Bone & Joint Surgery, 2001. **83**(10): p. 1514-1523.

186. P.R. Supronowicz, et al., *Novel current-conducting composite substrates for exposing osteoblasts to alternating current stimulation.* Journal of Biomedical Materials Research, 2002. **59**(3): p. 499-506.

187. L. Ghasemi-Mobarakeh, et al., *Application of conductive polymers, scaffolds and electrical stimulation for nerve tissue engineering.* Journal of Tissue Engineering and Regenerative Medicine, 2011. **5**(4): p. E17-E35.

188. R.A. Green, et al., *Conducting polymer-hydrogels for medical electrode applications.* Science and Technology of Advanced Materials, 2010. **11**(1): p. 014107.

189. T.J. Rivers, T.W. Hudson, and C.E. Schmidt, *Synthesis of a novel, biodegradable electrically conducting polymer for biomedical applications.* Advanced Functional Materials, 2002. **12**(1): p. 33-37.

190. J.Y. Wong, R. Langer, and D.E. Ingber, *Electrically conducting polymers can noninvasively control the shape and growth of mammalian cells.* Proceedings of the National Academy of Sciences, 1994. **91**(8): p. 3201.

191. N.C. Foulds and C.R. Lowe, *Enzyme entrapment in electrically conducting polymers. Immobilisation of glucose oxidase in polypyrrole and its application in amperometric glucose sensors.* Journal of the Chemical Society, Faraday Transactions 1: Physical Chemistry in Condensed Phases, 1986. **82**(4): p. 1259-1264.

192. M. Umana and J. Waller, *Protein-modified electrodes. The glucose oxidase/polypyrrole system.* Analytical Chemistry, 1986. **58**(14): p. 2979-2983.

193. C.E. Schmidt, et al., *Stimulation of neurite outgrowth using an electrically conducting polymer.* Proceedings of the National Academy of Sciences, 1997. **94**(17): p. 8948-8953.

194. X. Liu, et al., *Electrical stimulation promotes nerve cell differentiation on polypyrrole/poly (2-methoxy-5 aniline sulfonic acid) composites.* Journal of Neural Engineering, 2009. **6**(6): p. 065002.

195. S. Adeloju and G. Wallace, *Conducting polymers and the bioanalytical sciences: new tools for biomolecular communications. A review.* Analyst, 1996. **121**(6): p. 699-703.

196. X. Cui, et al., *Surface modification of neural recording electrodes with conducting polymer/biomolecule blends.* Journal of Biomedical Materials Research: An Official Journal of The Society for Biomaterials, The Japanese Society for Biomaterials, and The Australian Society for Biomaterials and the Korean Society for Biomaterials, 2001. **56**(2): p. 261-272.

197. I. Sapurina and J. Stejskal, *The mechanism of the oxidative polymerization of aniline and the formation of supramolecular polyaniline structures.* Polymer International, 2008. **57**(12): p. 1295-1325.

198. J.H. Collier, et al., *Synthesis and characterization of polypyrrole–hyaluronic acid composite biomaterials for tissue engineering applications.* Journal of biomedical materials research, 2000. **50**(4): p. 574-584.

199. Y. Xiao, et al., *Electrochemical polymerization of poly (hydroxymethylated-3, 4-ethylenedioxythiophene)(PEDOT-MeOH) on multichannel neural probes.* Sensors and Actuators B: Chemical, 2004. **99**(2-3): p. 437-443.

200. M.R. Abidian, D.H. Kim, and D.C. Martin, *Conducting-polymer nanotubes for controlled drug release.* Advanced Materials, 2006. **18**(4): p. 405-409.

201. M. Ma, et al., *Bio-inspired polymer composite actuator and generator driven by water gradients.* Science, 2013. **339**(6116): p. 186-189.

202. L. Pan, et al., *Hierarchical nanostructured conducting polymer hydrogel with high electrochemical activity.* Proceedings of the National Academy of Sciences, 2012. **109**(24): p. 9287-9292.

203. N.A. Peppas, et al., *Hydrogels in biology and medicine: from molecular principles to bionanotechnology.* Advanced Materials. 2006. **18**(11): p. 1345-1360.

204. S. Van Vlierberghe, P. Dubruel, and E. Schacht, *Biopolymer-based hydrogels as scaffolds for tissue engineering applications: a review.* Biomacromolecules, 2011. **12**(5): p. 1387-1408.

205. Y. Zhao, et al., *3D nanostructured conductive polymer hydrogels for high-performance electrochemical devices.* Energy & Environmental Science, 2013. **6**(10): p. 2856-2870.

206. S. Sekine, et al., *Conducting polymer electrodes printed on hydrogel.* Journal of the American Chemical Society, 2010. **132**(38): p. 13174-13175.

207. M.R. Abidian, D.-H. Kim, and D.C. Martin, *Conducting-polymer nanotubes for controlled drug release.* Advanced Materials (Deerfield Beach, Fla.), 2006. **18**(4): p. 405.

208. D.H. Kim, M. Abidian, and D.C. Martin, *Conducting polymers grown in hydrogel scaffolds coated on neural prosthetic devices.* Journal of Biomedical Materials Research Part A, 2004. **71**(4): p. 577-585.

209. A. Phadke, et al., *Rapid self-healing hydrogels.* Proceedings of the National Academy of Sciences, 2012. **109**(12): p. 4383-4388.

210. A. Woolfson, et al., *Moisture-activated, electrically conducting bioadhesive hydrogels as interfaces for bioelectrodes: Effect of formulation factors on cutaneous adherence in wet environments.* Journal of Applied Polymer Science, 1995. **56**(9): p. 1151-1159.

211. D. Zhai, et al., *Highly sensitive glucose sensor based on Pt nanoparticle/polyaniline hydrogel heterostructures.* ACS Nano, 2013. **7**(4): p. 3540-3546.

212. X.M. Sun, et al., *Two-step synthesis of superabsorbent conducting hydrogel based on poly(acrylamide-pyrrole) with interpenetrating network structure.* Materials Research Innovations, 2011. **15**(1): p. 70-74.

213. D.H. Kim, M. Abidian, and D.C. Martin, *Conducting polymers grown in hydrogel scaffolds coated on neural prosthetic devices.* Journal of Biomedical Materials Research Part A, 2004. **71A**(4): p. 577-585.

214. T. Dai and Y. Jia, *Supramolecular hydrogels of polyaniline-poly(styrene sulfonate) prepared in concentrated solutions.* Polymer, 2011. **52**(12): p. 2550-2558.

215. G. Chamberlain, et al., *Concise review: mesenchymal stem cells: their phenotype, differentiation capacity, immunological features, and potential for homing.* Stem Cells, 2007. **25**(11): p. 2739-2749.

216. L.A. Greene and A.S. Tischler, *Establishment of a noradrenergic clonal line of rat adrenal pheochromocytoma cells which respond to nerve growth factor.* Proceedings of the National Academy of Sciences, 1976. **73**(7): p. 2424-2428.

217. R. García and A. Báez, *Atomic absorption spectrometry (AAS)*, in *Atomic absorption spectroscopy*. 2012, InTech.

218. E.J. Bradbury, et al., *Chondroitinase ABC promotes functional recovery after spinal cord injury.* Nature, 2002. **416**(6881): p. 636-640.

219. N.K. Guimard, N. Gomez, and C.E. Schmidt, *Conducting polymers in biomedical engineering.* Progress in Polymer Science, 2007. **32**(8–9): p. 876-921.

220. B. Mordike and T. Ebert, *Magnesium: properties—applications—potential.* Materials Science and Engineering: A, 2001. **302**(1): p. 37-45.

221. C. Zhu, et al., *Highly efficient nonprecious metal catalysts towards oxygen reduction reaction based on three-dimensional porous carbon nanostructures.* Chemical Society Reviews, 2016. **45**(3): p. 517-531.

222. X. Jia, et al., *Biocompatible Ionic Liquid–Biopolymer Electrolyte-Enabled Thin and Compact Magnesium–Air Batteries.* ACS Applied Materials & Interfaces, 2014. **6**(23): p. 21110-21117.

223. Y. Kong, et al., *A battery composed of a polypyrrole cathode and a magnesium alloy anode—Toward a bioelectric battery.* Synthetic Metals, 2012. **162**(7): p. 584-589.

224. S. Li, et al., *One-Step Synthesis of Graphene/Polypyrrole Nanofiber Composites as Cathode Material for a Biocompatible Zinc/Polymer Battery.* ACS Applied Materials & Interfaces, 2014. **6**(19): p. 16679-16686.

225. A. Guiseppi-Elie, *Electroconductive hydrogels: Synthesis, characterization and biomedical applications.* Biomaterials, 2010. **31**(10): p. 2701-2716.

226. V. Khomenko, V. Barsukov, and A. Katashinskii, *The catalytic activity of conducting polymers toward oxygen reduction.* Electrochimica Acta, 2005. **50**(7): p. 1675-1683.

227. D. Mawad, et al., *A single component conducting polymer hydrogel as a scaffold for tissue engineering.* Advanced Functional Materials, 2012. **22**(13): p. 2692-2699.

228. Z. Chen, et al., *A Three-Dimensionally Interconnected Carbon Nanotube–Conducting Polymer Hydrogel Network for High-Performance Flexible Battery Electrodes.* Advanced Energy Materials, 2014. **4**(12): p. 1400207

229. Y. Meng, et al., *Hierarchical porous graphene/polyaniline composite film with superior rate performance for flexible supercapacitors.* Advanced Materials, 2013. **25**(48): p. 6985-6990.

230. S. Ghosh and O. Inganäs, *Conducting polymer hydrogels as 3D electrodes: applications for supercapacitors.* Advanced Materials, 1999. **11**(14): p. 1214-1218.

231. T. Dai, et al., *Facile fabrication of conducting polymer hydrogels via supramolecular self-assembly.* Chemical Communications, 2008(36): p. 4279-4281.

232. L. Pan, et al., *Hierarchical nanostructured conducting polymer hydrogel with high electrochemical activity.* Proceedings of the National Academy of Sciences of the United States of America, 2012. **109**(24): p. 9287-9292.

233. H. Wu, et al., *Stable Li-ion battery anodes by in-situ polymerization of conducting hydrogel to conformally coat silicon nanoparticles.* Nature Communications, 2013. **4**: p. 1943.

234. B.R. Liu, et al., *Three-Dimensional Hierarchical Ternary Nanostructures for High-Performance Li-Ion Battery Anodes.* Nano Letters, 2013. **13**(7): p. 3414-3419.

235. Y. Shi, et al., *Nanostructured conductive polypyrrole hydrogels as high-performance, flexible supercapacitor electrodes.* Journal of Materials Chemistry A, 2014. **2**(17): p. 6086-6091.

236. Y. Shi, et al., *Conductive "Smart" Hybrid Hydrogels with PNIPAM and Nanostructured Conductive Polymers.* Advanced Functional Materials, 2015. **25**(8): p. 1219-1225.

237. S. Ghosh and O. Inganäs, *Self-assembly of a conducting polymer nanostructure by physical crosslinking: applications to conducting blends and modified electrodes.* Synthetic Metals, 1999. **101**(1): p. 413-416.

238. A.A. Arrieta Almario and R.L. Tarazona Caceres, *Study of kinetic formation and the electrochemical behavior of polypyrrole films.* Journal of the Chilean Chemical Society, 2009. **54**(1): p. 14-19.

239. H. Ding, et al., *Biologically Derived Soft Conducting Hydrogels Using Heparin-Doped Polymer Networks.* ACS Nano, 2014. **8**(5): p. 4348-4357.

240. D.A. Young, et al., *Stimulation of adipogenesis of adult adipose-derived stem cells using substrates that mimic the stiffness of adipose tissue.* Biomaterials, 2013. **34**(34): p. 8581-8588.

241. A.B. Mathur, et al., *Endothelial, cardiac muscle and skeletal muscle exhibit different viscous and elastic properties as determined by atomic force microscopy.* Journal of Biomechanics, 2001. **34**(12): p. 1545-1553.

242. S.R. Mukai, H. Nishihara, and H. Tamon, *Formation of monolithic silica gel microhoneycombs (SMHs) using pseudosteady state growth of microstructural ice crystals.* Chem. Commun., 2004 (7): p. 874-875.

243. F. Karnbach, *et al., Interplay of the open circuit potential-relaxation and the dissolution behavior of a single H_2 bubble generated at a Pt microelectrode.* The Journal of Physical Chemistry C, 2016. **120**(28): p. 15137-15146.

244. A.J. Bard, L.R.F., *electrochemical methods fundamentals and applications*, ed. 2. Vol. 18. 2012, Beijing: chemistry industry publisher. 269.

245. R.A. Green, et al., *Conducting polymers for neural interfaces: challenges in developing an effective long-term implant.* Biomaterials, 2008. **29**(24): p. 3393-3399.

246. M.R. Abidian and D.C. Martin, *Multifunctional Nanobiomaterials for Neural Interfaces.* Advanced Functional Materials, 2009. **19**(4): p. 573-585.

247. Y. Zhang, et al., *Carbon aerogel supported Pt-Zn catalyst and its oxygen reduction catalytic performance in magnesium-air batteries.* Journal of Materials Research, 2014. **29**(23): p. 2863-2870.

248. B.C. Thompson, et al., *Optimising the incorporation and release of a neurotrophic factor using conducting polypyrrole.* Journal of Controlled Release, 2006. **116**(3): p. 285-294.

249. Y. Zhao, et al., *Crosslinked three-dimensional demineralized bone matrix for the adipose-derived stromal cell proliferation and differentiation.* Tissue Engineering Part A, 2008. **15**(1): p. 13-21.

250. A. Kraytsberg and Y. Ein-Eli, *The impact of nano-scaled materials on advanced metal–air battery systems.* Nano Energy, 2013. **2**(4): p. 468-480.

251. R. Erbel, et al., *Temporary scaffolding of coronary arteries with bioabsorbable magnesium stents: a prospective, non-randomised multicentre trial.* The Lancet, 2007. **369**(9576): p. 1869-1875.

252. G. Mani, et al., *Coronary stents: a materials perspective.* Biomaterials, 2007. **28**(9): p. 1689-1710.

253. M. Schinhammer, et al., *Design strategy for biodegradable Fe-based alloys for medical applications.* Acta Biomaterialia, 2010. **6**(5): p. 1705-1713.

254. H. Hermawan, D. Dubé, and D. Mantovani, *Developments in metallic biodegradable stents.* Acta Biomaterialia, 2010. **6**(5): p. 1693-1697.

255. G.L. Song, and A. Atrens, *Corrosion mechanisms of magnesium alloys.* Advanced Engineering Materials, 1999. **1**(1): p. 11-33.

256. B. Liu and Y. Zheng, *Effects of alloying elements (Mn, Co, Al, W, Sn, B, C and S) on biodegradability and in vitro biocompatibility of pure iron.* Acta Biomaterialia, 2011. **7**(3): p. 1407-1420.

257. L. Choudhary and R.K. Singh Raman, *Magnesium alloys as body implants: Fracture mechanism under dynamic and static loadings in a physiological environment.* Acta Biomaterialia, 2012. **8**(2): p. 916-923.

258. M. Peuster, et al., *A novel approach to temporary stenting: degradable cardiovascular stents produced from corrodible metal—results 6–18 months after implantation into New Zealand white rabbits.* Heart, 2001. **86**(5): p. 563-569.

259. J. Emerit, C. Beaumont, and F. Trivin, *Iron metabolism, free radicals, and oxidative injury.* Biomedicine & Pharmacotherapy, 2001. **55**(6): p. 333-339.

260. M. Peuster, et al., *Long-term biocompatibility of a corrodible peripheral iron stent in the porcine descending aorta.* Biomaterials, 2006. **27**(28): p. 4955-4962.

261. S. Zhu, et al., *Biocompatibility of pure iron: in vitro assessment of degradation kinetics and cytotoxicity on endothelial cells.* Materials Science and Engineering: C, 2009. **29**(5): p. 1589-1592.

262. J.M. Seitz, et al., *Magnesium degradation products: effects on tissue and human metabolism.* Journal of Biomedical Materials Research Part A, 2014. **102**(10): p. 3744-3753.

263. P.P. Mueller, et al., *Control of smooth muscle cell proliferation by ferrous iron.* Biomaterials, 2006. **27**(10): p. 2193-2200.

264. T. Huang, Y. Zheng, and Y. Han, *Accelerating degradation rate of pure iron by zinc ion implantation.* Regenerative Biomaterials, 2016. **3**(4): p. 205-215.

265. S. Wang, et al., *In vitro degradation and surface bioactivity of iron-matrix composites containing silicate-based bioceramic.* Bioactive Materials, 2017. **2**(1): p. 10-18.

266. H. Hermawan, et al., *Fe–Mn alloys for metallic biodegradable stents: degradation and cell viability studies.* Acta Biomaterialia, 2010. **6**(5): p. 1852-1860.

267. H. Hermawan, D. Dubé, and D. Mantovani, *Degradable metallic biomaterials: design and development of Fe–Mn alloys for stents.* Journal of Biomedical Materials Research Part A, 2010. **93**(1): p. 1-11.

268. S. Zhu, et al., *Biocompatibility of Fe–O films synthesized by plasma immersion ion implantation and deposition.* Surface and Coatings Technology, 2009. **203**(10-11): p. 1523-1529.

269. M. Moravej, et al., *Electroformed iron as new biomaterial for degradable stents: Development process and structure–properties relationship.* Acta Biomaterialia, 2010. **6**(5): p. 1726-1735.

270. S.R. Narayanan, et al., *Materials challenges and technical approaches for realizing inexpensive and robust iron–air batteries for large-scale energy storage.* Solid State Ionics, 2012. **216**: p. 105-109.

271. B.T. Hang, et al., *The effect of additives on the electrochemical properties of Fe/C composite for Fe/air battery anode.* Journal of Power Sources, 2006. **155**(2): p. 461-469.

272. P. Sarin, et al., *Physico-chemical characteristics of corrosion scales in old iron pipes.* Water Research, 2001. **35**(12): p. 2961-2969.

273. M. Moravej, et al., *Electroformed pure iron as a new biomaterial for degradable stents: In vitro degradation and preliminary cell viability studies.* Acta Biomaterialia, 2010. **6**(5): p. 1843-1851.

274. M. Kiyama and T. Takada, *Iron compounds formed by the aerial oxidation of ferrous salt solutions.* Bulletin of the Chemical Society of Japan, 1972. **45**(6): p. 1923-1924.

275. Y. Xin, et al., *Corrosion behavior of biomedical AZ91 magnesium alloy in simulated body fluids.* Journal of Materials Research, 2007. **22**(7): p. 2004-2011.

276. J. Kassim, T. Baird, and J. Fryer, *Electron microscope studies of iron corrosion products in water at room temperature.* Corrosion Science, 1982. **22**(2): p. 147-158.

277. P. Sarin, et al., *Iron corrosion scales: model for scale growth, iron release, and colored water formation.* Journal of Environmental Engineering, 2004. **130**(4): p. 364-373.

278. J. Fan, et al., *Synthesis of different crystallographic FeOOH catalysts for peroxymonosulfate activation towards organic matter degradation.* RSC Advances, 2018. **8**(13): p. 7269-7279.

279. D. Vernekar and D. Jagadeesan, *Tunable acid–base bifunctional catalytic activity of FeOOH in an orthogonal tandem reaction.* Catalysis Science & Technology, 2015. **5**(8): p. 4029-4038.

280. Y. Jia, et al., *Facile one-pot synthesis of lepidocrocite (γ-FeOOH) nanoflakes for water treatment.* New Journal of Chemistry, 2013. **37**(8): p. 2551-2556.

281. X. Wang, et al., *Synthesis of β-FeOOH and α-Fe 2 O 3 nanorods and electrochemical properties of β-FeOOH.* Journal of Materials Chemistry, 2004. **14**(5): p. 905-907.

282. M.A. Rodríguez, *Anticipated degradation modes of metallic engineered barriers for high-level nuclear waste repositories.* JOM, 2014. **66**(3): p. 503-525.

283. I. Azoulay, C. Rémazeilles, and P. Refait, *Corrosion of steel in carbonated media: The oxidation processes of chukanovite (Fe2 (OH) 2CO3).* Corrosion Science, 2014. **85**: p. 101-108.

284. J.K. Heuer, and J.F. Stubbins, *An XPS characterization of FeCO3 films from CO2 corrosion.* Corrosion Science, 1999. **41**(7): p. 1231-1243.

285. C. Rémazeilles and P. Refait, *Fe(II) hydroxycarbonate Fe2(OH)2CO3 (chukanovite) as iron corrosion product: Synthesis and study by Fourier Transform Infrared Spectroscopy.* Polyhedron, 2009. **28**(4): p. 749-756.

286. Y. Takahashi, et al., *In-situ X-ray diffraction of corrosion products formed on iron surfaces.* Materials Transactions, 2005. **46**(3): p. 637-642.

287. L.S. McNeill, and M. Edwards, *Iron pipe corrosion in distribution systems.* Journal-American Water Works Association, 2001. **93**(7): p. 88-100.

288. Z. Tang, et al., *Characteristics of iron corrosion scales established under blending of ground, surface, and saline waters and their impacts on iron release in the pipe distribution system.* Corrosion Science, 2006. **48**(2): p. 322-342.

289. M. Dubiel, et al., *Microbial Iron Respiration Can Protect Steel from Corrosion.* Applied and Environmental Microbiology, 2002. **68**(3): p. 1440-1445.

290. K.F. Khaled, *Studies of iron corrosion inhibition using chemical, electrochemical and computer simulation techniques.* Electrochimica Acta, 2010. **55**(22): p. 6523-6532.

291 G. Frankel, *Fundamentals of corrosion kinetics*, in *Active Protective Coatings*. 2016, Springer. p. 17-32.

292. J. Feng, et al., *Single-layer MoS2 nanopores as nanopower generators.* Nature, 2016 536(7615): p. 197.

293. G. Xie, L. Wen, and L. Jiang, *Biomimetic smart nanochannels for power harvesting.* Nano Research, 2016. **9**(1): p. 59-71.

294. C. Cheng, et al., *Ion transport in complex layered graphene-based membranes with tuneable interlayer spacing.* Science Advances, 2016. **2**(2): p. e1501272.

295. S.F. Buchsbaum, et al., *DNA-modified polymer pores allow pH-and voltage-gated control of channel flux.* Journal of the American Chemical Society, 2014. **136**(28): p. 9902-9905.

296. L. Wen, et al., *Bioinspired Smart Gating of Nanochannels Toward Photoelectric-Conversion Systems.* Advanced Materials, 2010. **22**(9): p. 1021-1024.

297. L. Wen and L. Jiang, *Construction of biomimetic smart nanochannels for confined water.* National Science Review, 2013. **1**(1): p. 144-156.

298. C. Ehrenbeck and K. Jüttner, *Ion conductivity and permselectivity measurements of polypyrrole membranes at variable states of oxidation.* Electrochimica Acta, 1996. **41**(11): p. 1815-1823.

299. A. Partridge, et al., *Ion transport membranes based on conducting polymers.* Journal of Membrane Science, 1997. **132**(2): p. 245-253.

300. Q. Zhang, et al., *Organic/Inorganic Hybrid Nanochannels Based on Polypyrrole-Embedded Alumina Nanopore Arrays: pH-and Light-Modulated Ion Transport.* Advanced Functional Materials, 2015. **25**(14): p. 2091-2098.

301. B. Bao, et al., *3D Porous Hydrogel/Conducting Polymer Heterogeneous Membranes with Electro-/pH-Modulated Ionic Rectification.* Advanced Materials, 2017. 29(44): p. 1702926..

302. J. Pyun and K. Matyjaszewski, *Synthesis of nanocomposite organic/inorganic hybrid materials using controlled/"living" radical polymerization.* Chemistry of Materials, 2001. **13**(10): p. 3436-3448.

303. Q. Yang, Z. Hou, and T. Huang, *Self-assembled polypyrrole film by interfacial polymerization for supercapacitor applications.* Journal of Applied Polymer Science, 2015. **132**(11): p. 41615.

304. G. Qi, Z. Wu, and H. Wang, *Highly conductive and semitransparent free-standing polypyrrole films prepared by chemical interfacial polymerization.* Journal of Materials Chemistry C, 2013. **1**(42): p. 7102-7110.

305. K.-J. Ahn, et al., *Surfactant-Templated Synthesis of Polypyrrole Nanocages as Redox Mediators for Efficient Energy Storage.* Scientific Reports, 2015. **5**: p. 14097.

306. H. Aizawa, *Morphology of polysorbate 80 (Tween 80) micelles in aqueous 1, 4-dioxane solutions.* Journal of Applied Crystallography, 2009. **42**(4): p. 592-596.

307. L. Feng, et al., *Super-hydrophobic surfaces: from natural to artificial.* Advanced Materials, 2002. **14**(24): p. 1857-1860.

308. J. Song, et al., *Bio-inspired isotropic and anisotropic wettability on a Janus free-standing polypyrrole film fabricated by interfacial electro-polymerization.* Journal of Materials Chemistry A, 2013. **1**(5): p. 1740-1744.

309. Q.H. Yang, Z.Y. Tu, and N.Y. Zhao, *Research on interfacial polymerization of pyrrole assist with Span80 system.* IOP Conference Series: Materials Science and Engineering, 2016. **137**(1): p. 012070.

310. B. Tian and G. Zerbi, *Lattice dynamics and vibrational spectra of polypyrrole.* The Journal of Chemical Physics, 1990. **92**(6): p. 3886-3891.

311. Chougule, M.A., et al., *Synthesis and characterization of polypyrrole (PPy) thin films.* Soft Nanoscience Letters, 2011. **1**(01): p. 6.

312. J. Gao, et al., *High-performance ionic diode membrane for salinity gradient power generation.* Journal of the American Chemical Society, 2014. **136**(35): p. 12265-12272.

313. W. Guo, Y. Tian, and L. Jiang, *Asymmetric ion transport through ion-channel-mimetic solid-state nanopores.* Accounts of Chemical Research, 2013. **46**(12): p. 2834-2846.

314. Y. Ito, et al., *The movement of a water droplet on a gradient surface prepared by photodegradation.* Langmuir, 2007. **23**(4): p. 1845-1850.

315. D.K. Kim, C. Duan, Y.F. Chen, A. Majumdar, *Power generation from concentration gradient by reverse electrodialysis in ion-selective nanochannels*. Microfluidics and Nanofluidics, 9 (2010): p. 1215-1224.

316. H.-C. Yeh, C.-C. Chang, and R.-J. Yang, *Reverse electrodialysis in conical-shaped nanopores: salinity gradient-driven power generation.* RSC Advances, 2014. **4**(6): p. 2705-2714.

317. R. Skouri, et al., *Swelling and elastic properties of polyelectrolyte gels.* Macromolecules, 1995. **28**(1): p. 197-210.

318. L. Poole-Warren, et al., *Development of bioactive conducting polymers for neural interfaces.* Expert Review of Medical Devices, 2010. **7**(1): p. 35-49.

319. C. Deslouis, et al., *Mixed ionic-electronic conduction of a conducting polymer film. Ac impedance study of polypyrrole.* Electrochimica Acta, 1996. **41**(7-8): p. 1343-1349.

320. N. Gavish and K. Promislow, *Dependence of the dielectric constant of electrolyte solutions on ionic concentration: A microfield approach.* Physical Review E, 2016. **94**(1): p. 012611.

321. J. Hwang, et al., *Enhanced energy harvesting by concentration gradient-driven ion transport in SBA-15 mesoporous silica thin films.* Lab on a Chip, 2016. **16**(19): p. 3824-3832.

322. L. Shao, et al., *Tuning the performance of polypyrrole-based solvent-resistant composite nanofiltration membranes by optimizing polymerization conditions and incorporating graphene oxide.* Journal of Membrane Science, 2014. **452**(Supplement C): p. 82-89.

323. K. Boukerma, et al., *Surfactant-assisted control of the surface energy and interfacial molecular interactions of polypyrrole.* Colloids and Surfaces A: Physicochemical and Engineering Aspects, 2007. **293**(1): p. 28-38.

324. X. Zhu, et al., *A Charge-Density-Tunable Three/Two-Dimensional Polymer/Graphene Oxide Heterogeneous Nanoporous Membrane for Ion Transport.* ACS Nano, 2017. **11**(11): p. 10816-10824.

325. Y. He, et al., *A stable and long-lasting concentration cell based on a reduced graphene oxide membrane and natural resource electrolyte.* Journal of Materials Chemistry A, 2017. **5**(40): p. 21130-21133.

326. M. Masoodian, S. Jones, and B. Rogers, *Computer Human Interaction: 6th Asia Pacific Conference, APCHI 2004, Rotorua, New Zealand, June 29-July 2, 2004, Proceedings*. Vol. 3101. 2005: Springer.

327. J. Ji, et al., *Osmotic power generation with positively and negatively charged 2D nanofluidic membrane pairs.* Advanced Functional Materials, 2017. **27**(2), 1603623.

328. R. Ansari Khalkhali, W.E. Price, and G.G. Wallace, *Quartz crystal microbalance studies of the effect of solution temperature on the ion-exchange properties of polypyrrole conducting electroactive polymers.* Reactive and Functional Polymers, 2003. **56**(3): p. 141-146.

329. K.P. Vidanapathirana, et al., *Ion movement in polypyrrole/dodecylbenzen-esulphonate films in aqueous and non-aqueous electrolytes.* Solid State Ionics, 2002. **154-155**: p. 331-335.

330. B. Yilmaz and Z. Evis, *Biomimetic coatings of calcium phosphates on titanium alloys*, in *Biomedical Nanomaterials: From Design To Implementation*. 2016, Institution of Engineering and Technology. p. 3-14.

331. T. Hery and V.-B. Sundaresan, *Ionic redox transistor from pore-spanning PPy (DBS) membranes.* Energy & Environmental Science, 2016. **9**(8): p. 2555-2562.

332. Y. Yang, et al., *A novel codoping approach for enhancing the performance of polypyrrole cathode in a bioelectric battery*. Carbon, 2014. **80**: p. 691-697.

333. M.F. John, et al., *Biocompatibility implications of polypyrrole synthesis techniques.* Biomedical Materials, 2008. **3**(3): p. 034124.

334. A. Gelmi, M.J. Higgins, and G.G. Wallace, *Physical surface and electromechanical properties of doped polypyrrole biomaterials.* Biomaterials, 2010. **31**(8): p. 1974-1983.

335. A. Siria, M.-L. Bocquet, and L. Bocquet, *New avenues for the large-scale harvesting of blue energy*. Nature Reviews Chemistry, 2017. **1**(11): p. 0091.

336. G. Bhave and E.G. Neilson, *Body fluid dynamics: back to the future.* Journal of the American Society of Nephrology, 2011,**22**(12):p. 2166-2181.

337. J. Wang, et al., *Microstructure and corrosion properties of as sub-rapid solidification Mg–Zn–Y–Nd alloy in dynamic simulated body fluid for vascular stent application.* Journal of Materials Science: Materials in Medicine, 2010. **21**(7): p. 2001-2008.

Permission Letters

Copyright Clearance Center RightsLink®

Home | Account Info | Help

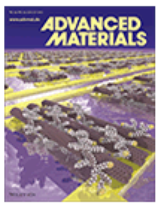

Title: A Cytocompatible Robust Hybrid Conducting Polymer Hydrogel for Use in a Magnesium Battery

Author: Changchun Yu, Caiyun Wang, Xiao Liu, et al

Publication: Advanced Materials

Publisher: John Wiley and Sons

Date: Aug 31, 2016

Logged in as:
changchun yu
Account #:
3001411288

LOGOUT

Review Order

Please review the order details and the associated terms and conditions.

No royalties will be charged for this reuse request although you are required to obtain a license and comply with the license terms and conditions. To obtain the license, click the Accept button below.

Licensed Content Publisher	John Wiley and Sons
Licensed Content Publication	Advanced Materials
Licensed Content Title	A Cytocompatible Robust Hybrid Conducting Polymer Hydrogel for Use in a Magnesium Battery
Licensed Content Author	Changchun Yu, Caiyun Wang, Xiao Liu, et al
Licensed Content Date	Aug 31, 2016
Licensed Content Volume	28
Licensed Content Issue	42
Licensed Content Pages	7
Type of use	Dissertation/Thesis
Requestor type	Author of this Wiley article
Format	Electronic
Portion	Full article
Will you be translating?	No
Title of your thesis / dissertation	Engineering cytocompatible conducting polymers for bio-related energy applications
Expected completion date	Mar 2019
Expected size (number of pages)	180
Requestor Location	AIIM building, innovation campus AIIM building, innovation campus university of wollongong wollongong, New South Wales 2500 Australia Attn: AIIM building, innovation campus
Publisher Tax ID	EU826007151
Total	0.00 AUD